

**Implementation of a Novel
Fucosyltransferase Inhibition Assay on a
Digital Microfluidics Device**

Laura Leclerc

A Thesis
In
The Department
Of
Biology

Presented in Partial Fulfillment of the Requirements
for the Degree of Master of Science (Biology) at
Concordia University
Montreal, Québec, Canada
© Laura Leclerc (2018)

CONCORDIA UNIVERSITY

School of Graduate Studies

This is to certify that the thesis prepared

by: Laura Leclerc

entitled: Implementation of a Novel Fucosyltransferase Inhibition Assay on a Digital
Microfluidics Device.

and submitted in partial fulfillment of the requirements for the degree of

Master of Science (Biology)

complies with the regulations of the University and meets the accepted standards with respect to
originality and quality.

Signed by the final Examining Committee:

_____ Chair

Dr. Aashiq Kachroo

_____ Examiner

Dr. Nawwaf Kharma

_____ Examiner

Dr. Vincent Martin

_____ Examiner

Dr. Steve Shih

_____ Supervisor

Dr. David Kwan

Approved by _____

Chair of Department or Graduate Program Director

Date _____ 2018 _____

Dean of Faculty

Abstract

Implementation of a Novel Fucosyltransferase Inhibition Assay on a Digital Microfluidics Device

Laura Leclerc

Cell-surface carbohydrates—or glycans—influence growth, differentiation, and immune response mechanisms. Alterations to the glycome can be markers for diseases including diabetes, neurodegenerative disorders, and cancer. Fucosyltransferases catalyze the addition of a fucose sugar residue to specific cell-surface glycans, which are involved in intercellular cell rolling/adhesion interactions such as white blood cells homing to inflammation sites and sperm-egg binding in fertilization. Fucosylated glycans are also implicated in inflammatory disease and cancers. In viral and microbial infections, fucosyltransferases can play a role in the adhesion and colonization of the host organism, as in the case of *Helicobacter pylori* $\alpha(1,3)$ -fucosyltransferase (FucT).

To better our understanding of glycome alterations and improve medical diagnostics and treatments, screens for glycosyltransferase activity and inhibition are needed. Efficient screens for specific glycosylations tend toward costly materials, instrumentation, and specialized skillsets—here, we present a novel inhibition assay for FucT using the fluorogenically labeled disaccharide, MU- β -LacNAc. The assay shows good potential for high throughput (Z' =0.78 in 384-well plate), though such an application is not shown here. It was also implemented on a digital microfluidic (DMF) platform, where inhibition curves of FucT by GDP, a product of the glycosyltransferase reaction that exhibits an inhibitory feed-back loop, were generated on-device. Results of the assay on DMF ($IC_{50} = 0.093 \text{ mM} \pm 0.037$) were shown to be comparable to results in a 384-well plate ($IC_{50} = 0.114 \text{ mM} \pm 0.086$), achieving a 87.5% reduction in reaction volume and setting the groundwork for future fully automated screens for potential inhibitors of glycosyltransferases.

Acknowledgements

First and foremost, I would like to thank my supervisors, David Kwan and Steve Shih, for providing me with the wonderful opportunity to pursue the work described in this thesis. It has been an invaluable and truly enjoyable experience, giving me the chance to enrich my knowledge in the interesting fields of chemical glycobiology and microfluidics while gaining useful interdisciplinary skills. It has been a privilege, and I will always be thankful to them.

I would also like to thank my lab-mates in both the Kwan and Shih labs, who have been there for me in a spectrum of ways, from showing me where things are in the lab for the 100th time to taking the 3-hour trip (each way!) to attend my wedding. They have been wickedly enabling in conversations about science, technology and philosophy, in which we have mutually fanned the flames of each others passions in uncontrolled and enthusiastic bouts of what muggles call ‘nerding-out’. That people such as themselves take an active interest in brightening the future of our world polishes our prospects to a Sirius shine. They have been supportive friends, both in and outside of work. Special thanks to Guy Soffer for reintroducing me to Python and for all of his troubleshooting help, as well as building hardware that is indeed, quite solid- and to Mohamed Nasr, for being steadfast in his company, a voice of reason I could count on, and for taking on part of my lab duties in my time of need. My time in their company has been a blessing. I wish them all the greatest success.

Last but not least, I would like to thank my parents, my brother, and my wife in all of their support for this path I have intended to pursue since my early childhood. Thanks to my cherished family, there is lift to carry me upward on the wings of aspiration. Not a day passes in which I am not deeply grateful for them.

It is thanks to the help and guidance of Shih and Kwan lab supervisors and colleagues that the work described in this thesis was made possible. To outline the contributions that each author made to the work, what follows is an overview of author contributions.

The project was conceptualized by Dr. David Kwan and Dr. Steve Shih, then further developed with my additions.

The research article relevant to this work was written by me, and was edited by Dr. Steve Shih and Dr. David Kwan.

Most solutions were prepared by my work using dry solids ordered from Sigma Aldrich (St. Louis, MO, U.S.A.) and Carbosynth (Compton, U.K.), with some exceptions. GDP-fucose had been previously synthesized by Dr. Ching-Ching Yu and Teng-Wei Tsai (National Chung-Cheng University, Taiwan). Additionally, certain synthesis and purification steps of MU- β -LacNAc had assistance from Dr. David Kwan.

Expression vectors for enzymes were obtained from the previous work of Dr. David Kwan.

Experiments, data collection and analyses were all conducted by myself. The resulting figures were also created by me, and then revised and approved by Dr. Steve Shih and Dr. David Kwan.

The automation system's hardware was designed and optimized by Amin Firouzeh, Philippe Vo, and Guy Soffer. The framework code for the automation system was written, optimized and troubleshooted by Guy Soffer. A GUI for the automation system was created by me with help from Guy Soffer. Additional software (PaseMaker) to generate path-solved electrode actuation sequences for the automation system was written by me.

I also thank the following institutions and organisations for their contribution for funding and resources:

- The John R. Evans Leaders Fund for awarding Dr. David Kwan and Dr. Steve Shih with funds in support of the acquisition of lab resources used in this thesis.
- Concordia University's Centre for Applied Synthetic Biology (CASB) for training, access and usage of their equipment.
- The Natural Sciences and Engineering Research Council of Canada (NSERC) for awarding the Centre for Applied Synthetic Biology (CASB) with funds in support of academic resources, training, and the acquisition of lab resources used in this thesis.
- Concordia University Department of Biology for funding, academic resources and for training, access and usage of their equipment.
- École Polytechnique de Montréal's Engineering Physics Department's Microfabrication Laboratory / Laboratoire de microfabrication (LMF) for training, access and usage of their clean-room facilities.
- Concordia University's Department of Engineering and Computer Science's Silicon Microfabrication lab (ConSIM) for training, access and usage of their clean-room facilities.

This thesis is dedicated to the memory of Dr. John G. Sperling, a prominent humanist who fought to create opportunities for higher education. He will remain an inspiration for generations of visionaries to come. This thesis is also dedicated to Dr. Luc Varin and Dr. Nawwaf Kharma, whose deep integrity in both their intellectual and teaching pursuits will always make them my role models.

“Knowledge is important, but much more important is the use towards which it is put. This depends on the heart and mind of the one who uses it.”

– His Holiness the 14th Dalai Lama

Table of Contents

<i>List of Figures</i>	<i>x</i>
<i>List of Tables</i>	<i>xii</i>
<i>List of Equations</i>	<i>xii</i>
<i>List of Abbreviations</i>	<i>xiii</i>
<i>Articles in Preparation for Publication</i>	<i>xiv</i>
Chapter 1. Introduction	1
1.1. Introduction to Cell-surface Glycosylation	1
1.1.1. General introduction to glycobiology.....	1
1.1.2. Definition of glycans.....	3
1.1.3. The role of cell-surface glycosylation.....	4
1.1.4. Abnormal glycosylation as a disease marker.....	6
1.1.5. Medical treatment using glycan-based approaches.....	7
1.1.6. Focus: the role of cell-surface fucosylation.....	9
1.1.7. Abnormal fucosylation and disease.....	10
1.2. Assays for Glycosylation and its Inhibition	13
1.2.1. The challenges of glycosylation assays.....	13
1.2.2. Overview of approaches to inhibition assays for α -(1,3)-fucosyltransferases.....	15
1.3. Microfluidic Devices	17
1.3.1. Introduction to microfluidics platforms.....	17
1.3.2. Enzymatic assays on digital microfluidic devices.....	19
1.3.3. Types of digital microfluidic devices.....	21
1.3.4. Theory of droplet movement.....	22
1.3.5. The challenges of DMF.....	28
Chapter 2. Thesis Objectives	30
2.1. Testing a hypothetical inhibition assay using a synthetic fluorescently labelled disaccharide, MU-β-LacNAc	30
2.2. Implementing the Fucosylation Inhibition Assay on a DMF Device	31
Chapter 3. Methodology	33
3.1. Reagents and Materials	33
3.2. Transformation of Abg2F6, BgaA, SpHex and FucT expression strains	35
3.3. Protein Expression and Purification for Abg-2F6, BgaA, SpHex and FucT	35
3.4. Enzymatic Synthesis and Purification of MU-β-LacNAc	38
3.5. Fucosylation Assay in Well Plates	40
3.6. Fluorescence Readings	40
3.6.1. Calibration in Well Plates.....	40
3.6.2. Reading Fluorescence from DMF chips.....	41
3.6.3. Optimization of Settings.....	42
3.6.4. Normalization and Analysis.....	42
3.7. Automation Hardware Setup	43

3.8.	Fabrication of Digital Microfluidics Chips.....	45
3.9.	Design, Fabrication and Operation of Digital Microfluidics Devices	48
3.9.1.	Design and operation of chip	48
3.9.2.	Fucosylation inhibition assay on a DMF device	51
3.9.3.	Software setup	54
3.9.4.	Software operation: Running an assay-on-device.....	54
Chapter 4.	<i>Assay Validation.....</i>	61
4.1.	Testing the Hydrolysis of MU-β-LacNAc.....	61
4.2.	Optimization of Enzyme Concentration and Hydrolysis Incubation Time.....	63
4.3.	Inhibition by GDP: Proof-Of-Concept	67
Chapter 5.	<i>DMF Platform Validation</i>	69
5.1.	Optimization of Fucosylation Inhibition Assay for Digital Microfluidics	69
5.1.1.	Optimization of dispensing to prevent biofouling	70
5.1.2.	Optimization of movement using oil and surfactants	70
5.1.3.	Testing DMF surfactant and oil impact on 4-MU fluorescence.....	74
5.1.4.	Optimizing electrode shape for droplet movement.....	76
5.1.5.	Optimization of dispensing by actuation sequence.....	77
5.1.6.	'Pixel Count': Image analysis to obtain droplet volume from area occupied	79
5.1.7.	Testing homogeneity of solutions mixed on DMF device	83
5.1.8.	Testing calculation of 4-MU concentration: Pixel Count validation	85
5.2.	Inhibition Assay on DMF Device	87
5.2.1.	Serial dilutions on chip	87
5.2.2.	Inhibition of a fucosyltransferase on chip.....	88
Chapter 6.	<i>Concluding Remarks.....</i>	95
References	98
Appendix	114
	Introduction to DMF Automation Systems	114
	LLGUI.....	114
	PaseMaker (Path Sequence Maker).....	116

List of Figures

Figure 1) Glycosylated protein with molecular depiction of a glycosidic bond.....	3
<i>Illustration of a glycan, depicting the chemical structure of a glycosidic bond.</i>	
Figure 2) Fucosylation of Sialyl LacNAc to form Sialyl-LewisX.....	9
<i>Illustration of the $\alpha(1,3)$-fucosylation of Sialyl-LacNAc into Sialyl-LewisX.</i>	
Figure 3) Electrostatic motion of a droplet on a digital microfluidics device	24
<i>Diagram depicting the induction of droplet motion by electrostatic forces.</i>	
Figure 4) Schematic of MU- β -LacNAc Inhibition Assay.....	31
<i>Depiction of the interactions (or lack thereof) between assay components in conditions with or without inhibitor and the resulting expected fluorescent signal.</i>	
Figure 5) Synthesis of fluorogenic 4-MU tagged oligosaccharide	38
<i>Depiction of MU-β-LacNAc chemoenzymatic synthesis using the mutant agrobacterium glycosynthase Abg2F6.</i>	
Figure 6) Scan of the surface of a DMF chip mounted on a well plate with fluorescence intensity.	41
<i>8 concentrations of 4-MU pipetted to a digital microfluidic device, scanned by well plate reader, and visualized with a heatmap in MARS (©BMG Labtech).</i>	
Figure 7) Automation system diagram	43
<i>Diagram of the digital microfluidics hardware used and their connectivity.</i>	
Figure 8) Photolithographic fabrication.....	45
<i>Illustration of a DMF device at different stages of photolithographic fabrication.</i>	
Figure 9) Design of DMF Device	48
<i>Layout of the DMF Device with electrodes labeled by their function.</i>	
Figure 10) Volume manipulations on DMF device	50
<i>Camera images of the types of operations (ex.: dispensing, mixing...) performed on the digital microfluidic device.</i>	
Figure 11) Illustrated protocol for performing the assay on-chip.....	51
<i>Illustrated protocol describing the steps of the MU-β-LacNAc assay performed on digital microfluidic device.</i>	
Figure 12) Example of a DMF device and its corresponding .csv.....	55
<i>Diagram of the electrode layout of a sample device and its corresponding input for the universal path sequence solving software (PaseMaker).</i>	
Figure 13) PaseMaker sequence construction example	57
<i>Demonstration of the construction of an electrode actuation sequence by PaseMaker through a screenshot of the program GUI and its text output.</i>	
Figure 14) LLGUI.exe interface	58
<i>Screenshot of the in-house software with a graphical user interface for controlling the DMF device.</i>	
Figure 15) Desktop during a DMF experiment.....	59
<i>Screenshot showing the layout of softwares and the camera image on a screen during a DMF experiment.</i>	
Figure 16) ArduBridge script by Guy Soffer	60
<i>Screenshot showing where the script used by the python automation framework needs to be changed between different experimental protocols.</i>	

Figure 17) The hydrolysis of MU- β -LacNAc by BgaA and SpHex.....	62
<i>Bar graph reporting fluorescence of samples incubated either without, with one or with both of the Glycoside hydrolases β-gal from <i>S. pneumoniae</i> (BgaA) and N-acetylhexosaminidase from <i>S. plicatus</i> (SpHex).</i>	
Figure 18) Determination of optimal FucT concentration and length of hydrolysis reaction	64
<i>Fluorescence timecourse depicting the time to completion of the hydrolysis step of the MU-β-LacNAc-based assay with a separate curve for every concentration in a range of FucT concentrations, showing an inverse relationship between FucT concentration and maximum fluorescence.</i>	
Figure 19) Fucosylation prevents hydrolysis and subsequent fluorescent signal	65
<i>Fluorescence bar graph evaluating the MU-β-LacNAc-based assay's potential for throughput application by comparing the signal with and without FucT and measuring its precision.</i>	
Figure 20) Proof-of-concept: Inhibition curves using GDP	67
<i>Proof-of-concept fluorescence-reported inhibition curve obtained for GDP inhibition of FucT using the MU-β-LacNAc-based assay.</i>	
Figure 21) Movement of bulky protein solution using different buffers and surfactants.....	72
<i>Bar graph evaluating the effect of different surfactant conditions and silicone oil on the movement of a bulky protein solution in a DMF experiment.</i>	
Figure 22) 4-MU Fluorescence with different surfactant concentrations.....	75
<i>Fluorescence standards comparing 4-MU concentrations prepared with Tetronics 150R1 and Pluronic F68 at various concentrations, and at DMF concentrations for these surfactants (0.05%), comparing their fluorescence with or without 5% silicone oil.</i>	
Figure 23) Skewed-wave electrodes compared to square electrodes.....	76
<i>AutoCAD diagram depicting a novel electrode shape and comparing the distance they span to a series of square electrodes of either the same area or height.</i>	
Figure 24) Pixel count being used to calculate a dilution factor.....	79
<i>Screenshots demonstrating the 'pixel count' method of calculating a dilution factor using an Adobe Photoshop edge-finding algorithm.</i>	
Figure 25) Accuracy and Precision of Pixel Count as a method of volume measurement.....	80
<i>Bar graph comparing volumes reported by three instruments: (1) precision balance, (2) micropipette, (3) pixel count.</i>	
Figure 26) Testing the homogeneity of the fluorescence of dispensed droplets from a volume mixed on-device.....	83
<i>Camera image and fluorescence heatmap of droplets mixed on-device.</i>	
Figure 27) Dispensed droplets fluoresce homogeneously from a volume mixed on-device.....	84
<i>Fluorescence bar graph comparing the fluorescence of droplets diluted from high and low initial 4-MU concentrations and mixed on-device to determine homogeneity of mixing.</i>	
Figure 28) Concentration of diluted 4-MU droplets calculated by fluorescence VS. pixel count.....	85
<i>Comparing, with diluted droplets from high and low initial 4-MU concentrations in 25 mM HEPES buffer, the concentration of 4-MU calculated by fluorescence standard VS. that which is calculated by pixel count.</i>	
Figure 29) Inhibition curves using GDP	90

Comparison of fluorescence-reported inhibition curves for FucT using GDP as the proof-of-concept inhibitor on DMF device and in a 384-well plate, before and after an additional glycine dilution step.

Figure 30) IC50 comparison before and after glycine dilution on both well plate and DMF device 92

Bar graph comparing the IC50 reported by DMF device and that reported by the same assay solutions (with oil and surfactant) in a 384-well plate.

Figure 31) 4-MU standards subjected to 5-fold dilution in pH 10.4 1M Glycine 93
Standard linear regressions of 4-MU fluorescence on a DMF device before and after a 5-fold dilution in pH 10.4 1M glycine.

List of Tables

Table 1) Roles played by different human fucosyltransferases in cancer	11
Table 2) Calculating the mm ² per pixel factor using the known size of a visual element of the chip design	82
Table 3) Pixel count-determined volumes for different volume settings on a 0.2-2 μ L micropipette	82
Table 4) How PaseMaker constructs sequences	117
Table 5) Examples of sequences made with PaseMaker	118

List of Equations

Equation 1) Lipmann-Young equation	23
Equation 2) Clausius-Mossotti factor	25
Equation 3) Complex Permittivity	25
Equation 4) Time-averaged dielectrophoretic force	26
Equation 5) Electromechanical model for horizontal force acting on a liquid	26
Equation 6) Critical frequency from the electromechanical force model for two-plate DMF	27
Equation 7) Estimated Z' Factor	66
Equation 8) Calculation of droplet volume by pixel count	81

List of Abbreviations

1. **4-MU** - 4-methylumbelliferone
2. **Abg2F6** – *Agrobacterium sp.* β -glucosidase-derived mutant glycosynthase
3. **A β** - amyloid β protein
4. **α GalF** - α -D-galactopyranosyl fluoride
5. **BgaA** - β -galactosidase from *Streptococcus pneumoniae*
6. **DMF** - Digital Microfluidics
7. **ER** - Endoplasmic Reticulum
8. **EWD**- Electrowetting-on-dielectric
9. **FucT** - α -1,3-Fucosyltransferase from *Helicobacter pylori*
10. **Fut1 through Fut11** - Human Fucosyltransferases 1 through 11
11. **GDP** - Guanosine Diphosphate
12. **GUI** - Graphical User Interface
13. **IBD** - Irritable Bowel Disease
14. **ITO** - Indium Tin Oxide
15. **LOD** - Limit of Detection
16. **MALDI-TOFMS** - Matrix-Assisted Laser Desorption/Ionization time-of-Flight Mass Spectrometry
17. **MU- β -GlcNAc** - 4-methylumbelliferyl *N*-acetyl- β -D-glucosaminide
18. **MU- β -LacNAc** - 4-methylumbelliferyl β -N-acetyllactosaminide
19. **PDB** - Protein Data Bank
20. **PLA** - Polylactic Acid
21. **pNP-Glc** - 4-nitrophenyl β -D-glucopyranoside
22. **sLeX** - Sialyl-Lewis^X
23. **SpHex** - N-acetylhexosaminidase from *Streptomyces plicatus*
24. **TLC** - Thin-Layer Chromatography

Articles in Preparation for Publication

A fucosyltransferase inhibition assay using digital microfluidics

Laura M. Y. Leclerc,^{1,2} Guy Soffer,^{2,3} David H. Kwan,^{1,2} Steve C.C. Shih*¹⁻³

¹Department of Biology, Concordia University, Montréal, Québec, Canada

²Centre for Applied Synthetic Biology, Concordia University, Montréal, Québec, Canada

³Department of Electrical and Computer Engineering, Concordia University, Montréal, Québec, Canada

*Corresponding author

Tel: (514) 848-2424 x7579

Email: steve.shih@concordia.ca

Chapter 1. Introduction

1.1. Introduction to Cell-surface Glycosylation

1.1.1. General introduction to glycobiology

Glycobiology is the study of the glycosylation of biological components, a process by which sugar residues are bound to other molecules. The catalysis of this sugar addition to specific target acceptors by enzymes called glycosyltransferases is found ubiquitously in all domains of life.¹⁻³ Due to a database study in which the Swiss-Prot protein database was scanned for known glycosylation site consensus sequences, it was long held that half of all proteins were glycosylated, thus falling under the umbrella term ‘glycoprotein’.⁴ However, a more modest (but still relatively large) proportion was estimated from a more recent database study, which employed an algorithm taking into account the body of knowledge which had since grown over 12 years to encompass multiple weighted evidence sources for glycosylations and their relative abundances, suggesting that it is only a fifth of proteins that are glycosylated.⁵

As the main component of the extracellular matrix, the dense coat of glycans found at the surface of cells is their first contact with the world outside of them, yet glycans have sometimes been overlooked in studies.^{6,7} With the help of large-scale glycomics initiatives like the Collaborative Glycomics Initiative in Europe, the Consortium for Functional Glycomics in the U.S.A., and the Human Disease Glycomics/Proteomics Initiative in Japan, a mere 52 known glycosyltransferase families with 13 solved crystal structures in 2001 has

grown to 106 families with 140 solved crystal structures in 2016.⁸ This showed a rapid increase in efforts to elucidate the mechanisms of their often complex and functionally diverse reactions.

The fields of glycobiology and glycomics have hence gained considerable traction in the past few decades, now at the forefront of many forms of research from the more efficient utilization of many types of carbohydrate-based biomass (ex.: waste made of paper, wood, etc.) as molecular sources to convert into biofuels, to glycan-based clinical diagnostics and therapeutics, the latter of which will be the focus of this introduction.

1.1.2. Definition of glycans

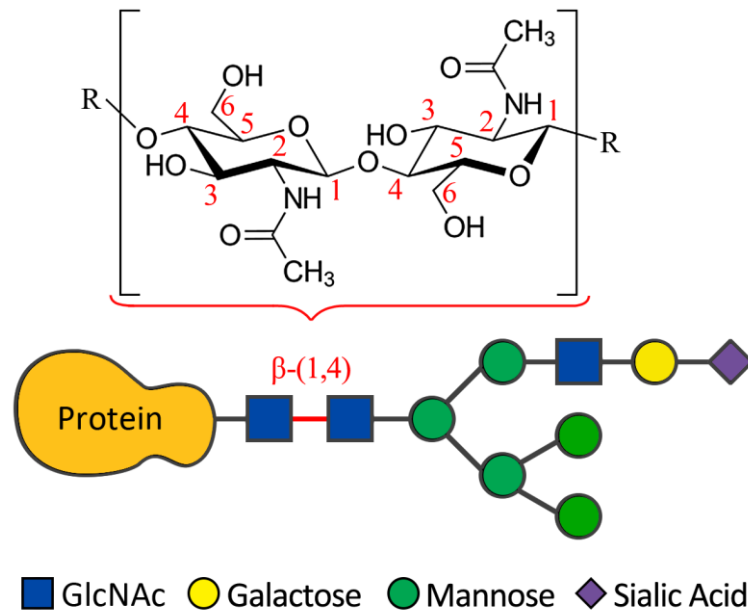


Figure 1) Glycosylated protein with molecular depiction of a glycosidic bond.

Representation of a glycan/oligosaccharide chain tethered to a protein using four of the standard color-coded symbols for sugar subunits: Glucose, Galactose, Mannose, and Sialic Acid. An α -(1,4) glycosidic bond is depicted between two glucose molecules as an example. Molecular structures drawn in ChemDraw.

In mice, every study in which an entire major class of glycans associated to vertebrate cells was genetically knocked out has resulted in embryonic lethality.⁹ To understand why glycans are so crucial, we must first examine what they are. The term ‘glycan’ refers to a broad range of carbohydrate sugars of varying length. They range from ‘polysaccharides’, which are chains of monosaccharides bound by glycosidic linkages, and ‘oligosaccharides’ when less than twenty monosaccharides are included, as well as simple sugars which comprise a single monosaccharide unit. Glycan chains are extremely diverse in composition, length and branching structure. The sugars that compose them are widely

represented across the literature by standard color-coded symbols. (Figure 1) The glycosidic bonds between them are described by their anomeric properties (α – when the O-glycosidic bond from C1 on the first sugar points in the opposite plane from the CH₂OH on that same sugar (can be referred to as C6), β – when the O-glycosidic bond from C1 on the first sugar aligns to the same plane as C6 on that sugar) and the position of the carbon on each sugar ring involved in the linkage.

1.1.3. The role of cell-surface glycosylation

In cells and on their surfaces, glycans mostly occur as post-translational additions made to proteins. Two categories of these glycans are the most commonly described, N-glycans and O-glycans. These are distinguished by the amino acids to which they are tethered; the majority are N-glycans, which are attached to an asparagine (Asn) side-chain, and a small minority are O-glycans, which are attached to either a serine (Ser) or threonine (Thr) side-chain and whose structures tend toward less branching.^{10, 11} They often participate in the fine-tuning of interactions between proteins, as evidenced by the many studies in which interference with glycans only subtly alters processes.¹² They have many other roles in addition to these, sometimes of crucial importance. These can be structural, such as in anchoring other proteins to the cell membrane, and even alter chemical properties of proteins such as stability in acid and heat as in the case of glycan changes resulting from alpha-L-fucosidase activity in the human liver, involved in child autoimmune disorders.¹³⁻
¹⁵ Most significantly, they have a wide range of regulatory functions through signaling mechanisms which control cell-cell recognition, interaction, growth, differentiation, and immune response.^{12, 16} Other categories of glycans exist at the cell surface besides N- and

O-glycans, each of them also involved in a diverse range of functions; glycosaminoglycans are linear repetitions of a disaccharide, highly abundant in the animal extracellular matrix and an important structural component of collagen, for which it acts as a physical spacer to order stroma (connective tissues).¹⁷ Glycosaminoglycans are also involved in tissue repair, with hyaluronan as example; following tissue injury, it is rapidly produced and excreted by cells.¹⁸ There is also considerable study of glycosylated lipids, referred to as glycolipidomics; phosphatidylinositol-linked glycans are involved in the proper formation of membranes and vesicles, among other functions, while glycosphingolipids are involved in cell-cell signaling, adhesion, and differentiation.^{19,20}

Most of the glycans at the cell surface are N-glycans, the most common eukaryotic covalent protein modification.²¹ The mammalian biosynthetic pathway to N-glycan formation begins with the assembly of a core oligosaccharide by transmembrane enzymes of the endoplasmic reticulum (ER).^{21,22} While a new protein is undergoing translation, a glycosyltransferase recognizing the consensus N-glycosylation sequence (Asn-X-Ser/Thr) catalyzes the formation of an N-glycosidic bond between its specific oligosaccharide and the nitrogen side-chain of the asparagine on the protein.²³ Beyond this step, most other glycosyltransferases exist as type II membrane proteins at the Golgi apparatus, providing additional glycosylations to modify and make additions to the core oligosaccharide.^{24,25}

Besides the enzymes involved in their construction, glycans interact specifically with a great number of proteins both in their immediate environment and on the surfaces of other cells, called lectins. These are a unique structural and functional class of proteins that recognize oligosaccharide chains; for instance, lacto-N-fucopentaose III is a cell-

surface glycan which, when recognized by cellular adhesion related proteins, stimulates B cell proliferation.^{26, 27}

To date, there are few, if any, cellular processes left with which glycans have not been implicated. Given biological systems simultaneously capable of expressing glycosyltransferases which can glycosylate specific target glycans, and glycoside hydrolases which can specifically cleave the glycosidic bonds of target oligosaccharides, glycans encode another important layer of post-translational programmability in living organisms. Hence, their further study could help in decoding biological function and eventually result in novel synthetic biological applications.

1.1.4. Abnormal glycosylation as a disease marker

One of the main reasons glycobiology is studied is due to its medical importance, given that changes to glycan structure and abundance comprise many markers for disease.²⁸⁻³⁰ For example, glycans play a role in Alzheimers, Parkinsons, and other neurodegenerative diseases; amyloid β protein ($A\beta$) and the microtubule-associated protein Tau are two of the main components of the plaques and tangles they are associated with. The abnormal glycosylation of $A\beta$ and Tau in Alzheimers-afflicted brains contributes to their pathological filament structuring and aggregation.³¹⁻³⁴

Among the shifts in glycosylation states linked to cancers, changes in fucosylation, sialylation, and the branching of glycans are some of the most important.³⁵ The tumor glycome is characterized by shortened O-glycans, increased sialylation, the presence of Lewis-type antigens on glycoproteins and glycolipids, an accumulation of

precursor glycans, and the skewed production of glycosylated products, among which the notable overproduction of immunosuppressive glycosphingolipids.³⁶⁻³⁸

Harnessing the specificity of lectins for their glycan ligands, lectin-based glycoproteomic analyses have been developed not only for further glycome studies, but also to help in diagnosing patients.³⁹

1.1.5. Medical treatment using glycan-based approaches

Like the distinct morphologies allowing us to identify other species by visual observation, immune systems identify foreign cells by ways of the distinct structural epitopes of their glycans, which bind to immune-system triggering lectins.⁴⁰ As an evolutionary result, it is common for parasitic organisms and bacteria to express glycans at their cell surfaces which mimic those of their host so as to evade immune response.^{1, 41-43} In turn, the immunosuppressive effect of glycans from certain parasitic worms such as *Trichuris suis* and *Schistosoma japonicum* has led to clinical trials which utilized their eggs or soluble egg extracts to treat autoimmune diseases such as IBD (Crohn's Disease).^{44, 45}

Harnessing glycans to opposite (immunostimulatory) effect, many vaccines have and continue to be developed through the covalent conjugation and coupling of glycans to an immunogenic carrier protein.⁴⁶ The glycans of bacteria, protozoans, parasitic worms, fungi, viruses as well as cancer cells can then be presented to the immune system for or targeting. STn- α GalCer is one such cancer vaccine candidate, made by attaching the tumor-associated disaccharide sialyl Tn to α -galactosylceramide, a natural killer T cell ligand. It has been shown to efficiently switch IgM antibody to STn-specific IgG, demonstrating its potential in training the immune system to attack tumor cells.⁴⁷ Animal vaccinations against

Alzheimer's disease-specific A β antigens have also been tested, but the stimulation of damaging neuroinflammatory response remains a problem.⁴⁸ Recent improvements in glycan synthesis and yield have contributed to the advancement of this research, which is progressing by leaps and bounds, with multiple bacterial vaccines already released on the market by Merck & Co., Sanofi Pasteur, and Wyeth Pharmaceuticals, with many more in development across many disease categories.⁴⁶

The recognition of cell-surface glycans by the immune system is also the same principle by which different blood group antigens from one's own— themselves glycans— can trigger an immune response if one is given blood from donors of different blood types.⁴⁹ As such, some are pursuing methods of converting other blood groups to universal blood groups through glycan-modifying biochemistry.⁵⁰

Last but not least, rather than acting as a treatment, pathways that assemble cell-surface glycans that play a role in disease such as sialyl-Lewis^X (sLeX) are the targets for treatment. In sLeX-deficient patients, insufficient sLeX led to a decrease in leukocyte extravasation and hence, insufficient immune response to combat infection.^{51, 52} Dietary supplements of L-fucose are able to restore proper sLeX expression.⁵³ When it comes to the inhibition of glycan formation, an increased understanding of the workings of glycosylation in disease models has brought the search for inhibitors for glycan-modifying proteins to new heights; many such inhibitors in the imino-sugar family are in the preclinical or approved stages for a multitude of diseases, from targeting ER α -glucosidases to treat Hepatitis B, to inhibiting CerGlcT glycosyltransferases for the treatment of lysosomal storage disorders such as Gaucher disease.⁵⁴⁻⁵⁶

1.1.6. Focus: the role of cell-surface fucosylation

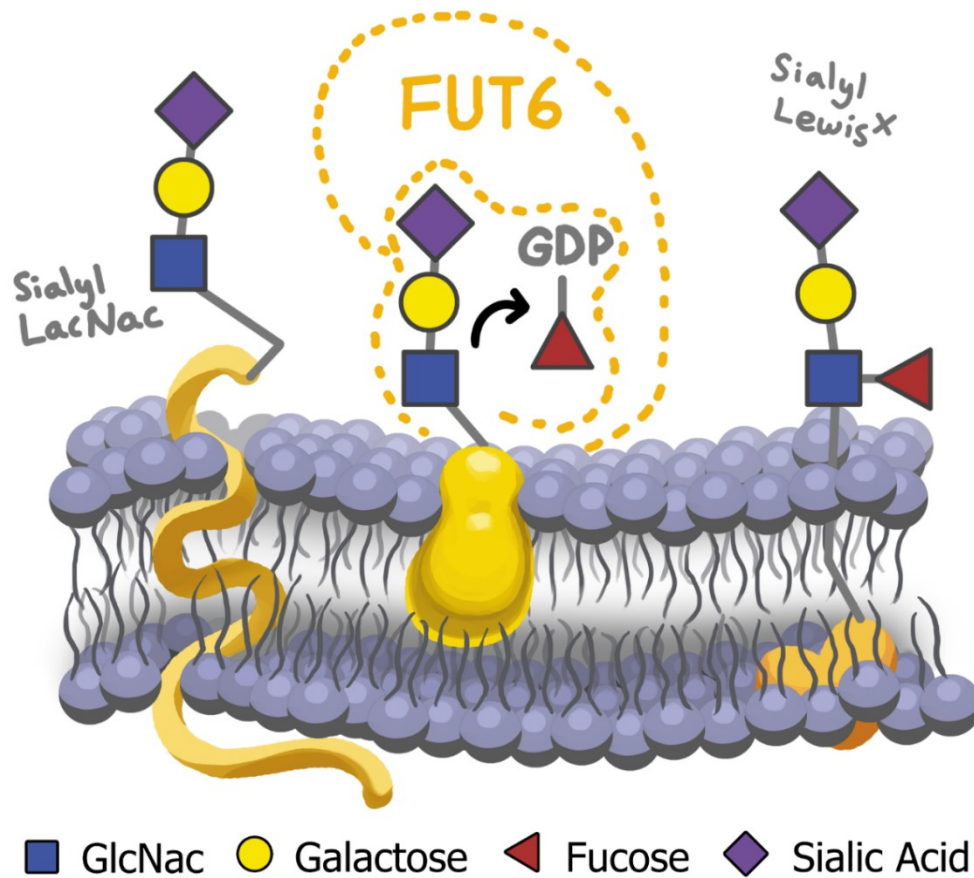


Figure 2) Fucosylation of Sialyl LacNac to form Sialyl-LewisX

A fucosyltransferase catalyzing the addition of a Fucose sugar residue from a GDP-Fucose donor to a Sialyl LacNac receptor glycan, resulting in Sialyl-Lewis^X, an important cell-surface glycan.

Fucosyltransferases are one of the glycosyltransferase families that are being pursued as a target for drug discovery research. Fucosyltransferases catalyze the transfer of a fucose sugar residue from GDP-Fucose to a glycan (Figure 2). In humans, there are 11 fucosyltransferases in total, whose usual expression is restricted to certain cell and tissue types. For example, FUT3 is highly expressed in the kidney and colon, but not the liver – meanwhile, FUT8 is expressed in the

liver, where it contributes to liver tissue regeneration in mice, and FUT9 is the primary $\alpha(1,3)$ -fucosyltransferase activity in the brain.⁵⁷⁻⁵⁹ Specifically for $\alpha(1,3)$ -fucosyltransferases (encompassing FUT3, FUT4, FUT5, FUT6, FUT7, FUT9, FUT10 and FUT11), upregulation can result in the increased formation of sialyl-Lewis^X (sLeX) glycans. These glycans bind to all three members of the selectin family of cell adhesion receptors implicated in lymphocyte homing and neutrophil extravasation during the course of an immune response, as well as platelet binding in the process of wound healing.^{60,61} As important modulators of the cell-surface glycome, the under- or over-expression of fucosyltransferases sometimes lies at the root of disease.

1.1.7. Abnormal fucosylation and disease

In the case of the fucosylated cell-surface glycan sLeX, its aberrant heightened expression on cell surfaces promotes interaction with selectins, facilitating endothelial crossing and adhesion.^{61, 62} This heightened expression of sLeX and the $\alpha(1,3)$ -fucosyltransferases that assemble it has been shown to promote higher metastatic potential, drug resistance, and malignancy in many cancers, making them promising therapeutic targets.^{35, 63-66} (Table 1)

Table 1) Roles played by different human fucosyltransferases in cancer

		Role in cancer(s)
α-1,2	Fut 1	With some colorectal cancer cell lines, heightened expression promotes drug resistance ⁶⁷ and proliferation. ⁶⁸ With some pancreatic, hepatic and colonic cancer cell lines, heightened expression results in a <i>decrease</i> in metastatic potential. ^{69, 70} With an ovarian cancer cell line, heightened expression promotes proliferation and drug resistance. ⁷¹ In chronic myeloid leukemia cells, heightened expression promoted multidrug resistance ⁷²
	Fut 2	With some colon cancer cell lines, lowered expression promoted, or was linked to heightened proliferation. ^{68, 73}
α-1,3/4	Fut 3	Heightened expression was observed in head, neck, metastatic colon cancer cells, and the inhibition of expression decreased proliferation. ^{66, 73, 74}
	Fut 4	Heightened expression in hepatocarcinoma cell lines was linked to multidrug resistance. ⁶⁴ In an epidermoid carcinoma cell line, overexpression was found to increase proliferation. ⁷⁵
	Fut 5	Heightened expression in breast cancer cell lines has been observed. ⁶⁵
	Fut 6	Heightened expression in hepatocarcinoma cell lines was linked to multidrug resistance. ⁶⁴ Heightened expression in breast and prostate cancer cell lines has been observed and promotes metastasis. ^{65, 76} In colon cancer cells, inhibition of expression decreased proliferation. ⁷⁴ Heightened expression was also observed in head and neck cancer cells. ⁶⁶
	Fut 7	In hepatocarcinoma and colon cancer cell lines, upregulation was linked to heightened metastatic potential. ⁷⁷⁻⁷⁹
	Fut 9, 10, 11	N/A (No evidence has been found linking the expression of Fut9, Fut10 or Fut11 to cancer)
α-1,6	Fut 8	Heightened expression in hepatocarcinoma cell lines was linked to multidrug resistance, metastasis and proliferation. ^{64, 80, 81}

In addition to their roles in cancer, human fucosyltransferase 7 (FUT7) has also been found to mediate the initiation and progression of Atherosclerosis, and FUT2 polymorphisms lowering its expression have been implicated in susceptibility to Crohn’s disease and asthma.⁸²⁻⁸⁴ Notably, many other diseases involving aberrant fucosyltransferase activity are of pathogenic origin. There are two primary ways this occurs; in the first, the infectious pathogen activates host fucosyltransferase genes to increase infectivity and possibly immune evasion. For instance, T-cell leukemia retrovirus activates FUT7, increasing sLeX expression to colonize the skin.⁸⁵ Likely to similar ends, Herpes virus specifically activates FUT3, FUT5 and FUT6 expression,

leading to increased sLeX production in infected hosts.^{82, 86, 87} A slew of human fucosyltransferase genes are also transcriptionally activated by cytomegalovirus, Varicella-zoster virus.^{86, 88} A virus or pathogenic organism can also encode their own fucosyltransferases.

Of particular interest to some- perhaps the 50% of humanity by which it is infected- is the gram-negative *Helicobacter pylori*, listed as a carcinogen by the World Health Organization and the International Agency for Research on Cancer. It is at the cause of peptic ulcers and can result in the development of mucosa-associated lymphoma and gastric adenocarcinoma.^{89, 90} The mimicry of host surface glycans such as sLeX and LeX (Lewis X) by *H. pylori* has been found to play a key role in colonization and adhesion to the host environment.^{89, 91-97} As such, the inhibition of *H. pylori* fucosyltransferases such as FucT (a bacterial $\alpha(1,3)$ -fucosyltransferase), which catalyze the formation of cell-surface glycans such as sLeX and LeX, is of clinical importance .

1.2. Assays for Glycosylation and its Inhibition

1.2.1. The challenges of glycosylation assays

The search for inhibitors for glycosyltransferases such as FucT begins with the development of a glycosylation assay. Many glycosyltransferases require a metal ion, often Mg^{2+} or Mn^{2+} , to act as catalysts before the sugar-nucleotide donor can bind and the substrate or ligand molecule is accepted.⁹⁸ As such, there are four core components to an assay: (1) the glycosyltransferase, (2) the metal ion, (3) the nucleotide sugar donor, and (4) the acceptor glycan.

Developing assays to study or monitor for the occurrence of these reactions presents some challenges. On the whole, the number of binding site interactions with low-to-high affinities and the many components involved can complicate assay development.⁹⁹ Furthermore, to report the adequate signal type and strength for the assay's platform of choice, additional components and reactions may need to be coupled to the addition of a sugar to a glycan substrate in a glycosylation reaction. *Ex-vivo*, glycans can be identified by immunohistochemistry- though antibodies are not specific to one glycan, but rather report a range of glycans.^{100, 101} Many other possible strategies have been employed *in vitro*. Lastly, some of the four core components of a glycosylation assay can be themselves difficult to obtain for an *in vitro* assay.

It is difficult to obtain sufficient amounts of human glycosyltransferases for *in vitro* testing, as these often suffer from lowered activity, low concentrations within the proteome, and a heterogeneity that makes them notoriously difficult to acquire and purify, alongside the additional issue of low half-lives.¹⁰²⁻¹⁰⁴ To express these, yeast (ex.: *Pichia pastoris*),

insect (ex.: *Spodoptera frugiperda*), and mammalian cell (ex.: chinese hamster ovary) lines are preferentially used for their compatibility with eukaryotic codon profiles and ability to perform the relevant post-translational modifications. The differences between the glycosylation pathways between these recombinant organisms have prompted efforts to ‘humanize’ these cell lines.¹⁰⁵⁻¹⁰⁹ Eukaryotic cells have lower protein synthesis and folding rates than in prokaryotes, and mammalian cells are also more fragile, with lower growth rates.^{110, 111} When it comes to bacterial glycosyltransferases such as FucT, which can be produced using *E. coli*, the material cost and labor intensity is lower than for human fucosyltransferases for which yeast is employed for production.

Another component of glycosylation assays that can be difficult to obtain are the acceptor glycans. The inherent variability of glycosylation in organisms results in heterogenous mixtures of subtly different glycans that are difficult to distinguish and purify, which makes cells a poor factory for specific glycans. To obtain them, an *in vitro* approach is preferred: with either (1) solid-phase synthesis reactions or (2) one-pot chemoenzymatic reactions. Solid-phase synthesis is a laborious chemical process, especially when it comes to longer glycans such as oligosaccharides. For every monosaccharide unit to be added to a template molecule, protecting groups must be added and removed (i.e., deprotected) in sequential reactions before glycosylation is achieved.¹¹² Since 1971, however, many tools and protocols such as oligosaccharide-to-polymer-support linkers, specialized glycosyl donors, and resin washes between steps have been created to further enhance, diversify, increase specificity, and automate this process.¹¹²

The innate biological ability of glycosyltransferase enzymes offers an attractive alternative to chemical synthesis in their efficiency as a tool, once they are either discovered

or engineered for that glycosylation reaction. Called ‘one-pot chemoenzymatic synthesis’, this less laborious technique employs an ever-growing repertoire of characterized glycosylation and glycoside-hydrolase proteins to synthesize myriad glycans with growing ease.^{113, 114} The genes encoding these enzymes are often sequenced and cloned in a plasmid expression vector for expression in a bacterial or yeast production strain. Whilst new glycosyltransferases continue to be discovered and characterized from all domains of life, many improved enzymes have been engineered to facilitate the choice of glycosylated products for use as acceptor glycans in assays, or other applications.

To date, there is no standardized method to assay for glycosylation, but many assays require additional components so as to enhance the reporting signal, such as the use of tryptic peptides in MALDI-TOFMS spectrometry for the ion enhancement of glycans in femtomole concentrations and simultaneous ion suppression of peptide ions.¹¹⁵ Other assay designs have paired glycosylation to a type of reporter signal separate from the glycan’s chemical or structural properties, such as absorbance, fluorescence, or fluorescence polarization.

1.2.2. Overview of approaches to inhibition assays for α -(1,3)-fucosyltransferases

The transition-state for fucosyltransferase involves four components: a divalent metal and nucleotide-sugar donor must work in concert with the acceptor substrate, both of which fucosyltransferase suffers a low affinity for.¹¹⁶⁻¹¹⁸ This has prompted the development of a myriad of differing strategies to efficiently assay for the inhibition.

To search for inhibitors of human fucosyltransferases, compound libraries have been tested. A high-throughput study which yielded many potential inhibitors of Fut6 and Fut7, for example, screened the Maybridge Hitfinder Collection (comprising 16,000 drug-like compounds at the time of the study) by monitoring for fluorescence polarization upon the addition of chemically synthesized fluorescein-tagged analog donor substrates to CMP-NeuAc and GDP-Fucose, to the commercially available glycoprotein fetuin.¹¹⁹ Due to the large size of fetuin, fluorescence polarization readings were made possible. This method was successful in finding inhibitors with a low (6%) rate of false positives.

Another study with extensive work screened a focused compound library derived from sugar nucleotides for inhibitors of Fut6 by MALDI-TOFMS-based monitoring of glycosylation of specially designed and synthesized acceptor glycans. To have their glycosylation reliably detected by MALDI-TOFMS, these glycans were modified for higher ion-sensitivity by tagging them with tryptophanylarginine and stable isotope.¹²⁰

Monitoring by TLC has also been employed as a manner of detecting fucosylation.¹²¹ In that study, three compounds isolated from the fungal organism *Stachybotrys cylindrospora* were screened for their ability to prevent the fucosylation of LacNAc by Fut6.

Another approach that has been used to detect this reaction is a pyruvate kinase/lactate dehydrogenase coupled-enzyme assay. In this assay, inhibition of Fut6 was detected for the fucosylation of LacNAc through a fluorescence reading, which indirectly measures the amount of GDP byproduct resulting from fucosylation with GDP-fucose. First, pyruvate kinase produces pyruvate from phosphoenolpyruvate and GDP, then lactate dehydrogenase uses NADH in solution to produce lactate from pyruvate.¹²² This results in a fluorescent signal inversely

proportional to the amount of GDP in solution, which itself is a measurement of how much GDP-fucose has been consumed by fucosylation.

While these assays have yielded potential candidate inhibitors, assay components and the libraries of potential inhibitors themselves are often expensive or otherwise difficult to obtain. Lowering the quantities required to perform assays as well as increasing the sensitivity are advantages that microfluidics can address.

1.3. Microfluidic Devices

1.3.1. Introduction to microfluidics platforms

A relatively recent field, microfluidics is described by the use of micro to pico-volume fluid handling systems for applications ranging from point-of-care medical diagnostics to the directed evolution of enzymes and microorganisms.¹²³⁻¹²⁶ PubMed lists more than 3000 publications with the “microfluidics” keyword published last year. According to a search on fluidicmems.com, an impressive 274 microfluidics companies are currently in existence. As the next step in the miniaturization and automation of laboratory protocols, microfluidic devices are often described as ‘labs-on-a-chip’. The throughput, materials, and cost of machinery involved differ between platforms (paper, droplet, channel and digital microfluidics) with continuous advances made which further lower their cost, already undercutting micro/nano fluid handling systems in price.

All microfluidics platforms benefit from reduced volumes. The conservation of reagent is important when these are difficult or costly to obtain, as it is for many chemically synthesized potential pharmaceuticals, or in limited availability such as blood samples from newborn infants, which can only be collected at a precious low volume; without conservative use per test, they

may not be able to subject it to every test needed. Besides the conservation of reagent, the heightening of surface area to volume ratio is another one of the boons of working at reduced volume; it accelerates heat transfer and mass transfer rates, resulting in the greater efficiency of exo- and endothermic reactions.^{127, 128} The increase of surface-area-to-volume ratios has long been a method of engineering the enhancement of biosensors and reaction cells for various applications.¹²⁹⁻¹³²

Channel microfluidics is the most widespread method in which microchannels are suffused with fluid and subjected to flow via syringe pumps or another pressure gradient. Given the small diameter of the channels ($\sim 1 \mu\text{m}$), flow is dominated by viscosity. This creates laminar flows characterized by low Reynold's numbers in which multiple fluid streams can flow in parallel within the same channels. Though the reliance on valves requires considerable expertise to fabricate and maintain, this system's advantages lie in multiplexing and high-throughput application, the increased resolution of separation granted by capillary gel electrophoresis, as well as the simulation of *in vivo* conditions such as blood vessels using synthetic vascular networks.¹³³⁻¹³⁶

Another popular microfluidics technique is droplet microfluidics, similar to channel microfluidics but with the automated generation of oil/water droplets in water/oil channels, often passively by junctions. These droplets are pinched off as the droplet volume exits the channel by the interruption of its flow by the volumes flowing out of adjacent channels. This allows for the ultra-rapid generation of droplets for high-throughput applications (10-100 kHz). Each droplet is analogous to a test tube, especially in systems that can perform operations downstream of droplet formation such as the sorting or merging of droplets to perform a reaction.¹³⁷⁻¹³⁹

Much like Thin-Layer Chromatography (TLC), paper microfluidics requires a minute amount of substrate to be introduced to a paper device, which can be three-dimensional, connect multiple devices, and easily fabricated or modified for different adsorptive or absorptive properties.^{140, 141} Paper microfluidics enjoys lower material costs than other microfluidics techniques, but is less integrable with certain applications that would demand responsive automated operation (ex.: sorting), the preservation of certain kinds of degradable samples, or assays with non-colorimetric output readings. Since its conception, many point-of-care diagnostics devices have been developed using this technology, which does not rely on any electronic components and can easily be transported to locations that are distant from any labs.^{142, 143}

Among the different microfluidic platforms, Digital MicroFluidics (DMF) alone allows for the individual addressability of discrete on-chip volumes (droplets) — seeing as one may move, split, merge, mix and dispense any droplet on demand, each droplet on the device could be processed differently based on one's desired need at every step of an experiment. DMF also enjoys ease of integration with standardized or homebrew software^{144, 145} and affordable electronics that can rapidly generate and respond to feedback based on visual, temperature, and electric signals among others¹⁴⁵⁻¹⁴⁸, enabling DMF to exhibit an unparalleled potential for intelligent automation. DMF has already been successfully explored as a miniature and cost-effective platform for enzymatic, immune, and DNA-based assays.¹⁴⁹⁻¹⁵³

1.3.2. Enzymatic assays on digital microfluidic devices

DMF devices have long been developed for a variety of enzymatic applications. Operations held on DMF devices include a three-enzyme pyrosequencing protocol which was used to successfully sequence a 229 base-pair *Candida parapsilosis* sequence with 100%

accuracy.¹⁵⁴ DMF devices have also been employed for the study of enzyme kinetics with alkaline phosphatase and fluorescein diphosphate, yielding values in accordance with the literature at a higher accuracy and while consuming less reagent.¹⁵⁵ The digestion of proteins by either trypsin or pepsin enzymes has also been performed with trypsin and pepsin immobilized to miniature agarose discs formed on DMF devices.¹⁵⁶ DMF has not only shown itself to be a platform suitable for enzyme assays, it also offers several advantages aside from those granted by individual addressability and automation.

Notably, the reduced volumes of droplets allow faster heating and cooling of samples in temperature-variable assays, increasing the speed at which they can be performed.¹⁴⁶ Time-efficiency is further increased by the faster rate of enzymatic reactions which has been observed for DMF droplets.¹⁵⁷ This is often attributed to the large surface area to volume ratio of small volumes, whose associated faster rates of mass and heat transfer can result in sped-up enzyme kinetics.^{137, 158} Another reason that assays can be sped up in DMF is due to the heightened concentration of substrates that can be used when these are of a precious or limited volume. This has been the case for an FDA-approved DMF device called SEEKER®, which is used to perform screens for lysosomal storage disorders.¹⁵⁷ Capable of performing 5 enzymatic assays for up to 48 samples, they estimate that while conventional methods could perform up to 10 tests per newborn blood sample, their DMF device can perform hundreds. Impressively, assays which took 20+ hours to incubate were reduced to 1 hour incubation times on the DMF device. These assays were all fluorometric in nature, using tools such as fluorescently tagged substrate glycans to report the hydrolytic action of enzymes involved in disease in a standardized manner for an automated, computer-controlled device.

As for glycan-modifying reactions, there has been a DMF device by Martin *et al.*, which quantifies the sulfonation of glycans performed enzymatically on-chip.¹⁵⁹ Solutions in on-chip reservoirs, containing assay components, epimerase or one of three sulfosyltransferases, could be dispensed in order to sequentially glycosylate heparan sulfate. The assay was aided both by biotin-tagging the glycans so that streptavidin-tagged magnetic nanoparticles would bind to them, and by using the radionuclide PAPS 35S to attach a radioactive sulfate to the glycans so that sulfonation could be quantified by scintillation counting.¹⁵⁹

1.3.3. Types of digital microfluidic devices

DMF devices exist in many forms, and while devices that employ acoustics, magnet-based, or photonic methods of producing droplet motion are sometimes included under the umbrella of DMF, here we talk purely about devices based on ‘electrowetting’ and ‘dielectrophoresis’.¹⁶⁰⁻¹⁶² Just like paper microfluidics, some of these devices have been construed that can transport liquids across 3D planes of various shapes, though 2D devices are the most prevalent.^{163, 164} In either case, a one-plate or a two-plate configuration can be used. Both of these utilize metallized electrodes on a surface, much like an electrical circuit wherein every electrode is ‘off’ during device operation until it is ‘actuated’, meaning that it has been switched ‘on’ to a high-voltage state. These surfaces are then coated with a dielectric layer; this can be any non-conductive material, which can be polarized to induce electric fields. Some chips are then treated with a hydrophobic layer to ease the movement of aqueous liquids across its surface (ex.: Teflon).

In a one-plate configuration, each electrode is accompanied by an adjacent ground electrode. This can complicate design steps, seeing as ground electrodes must be positioned such that droplets are in contact with both actuation and ground electrodes at all times during droplet

motion. Furthermore, exposed droplets are more prone to evaporation, and their electric fields are weaker, to the detriment of droplet movement and especially splitting and dispensing operations.¹⁶⁵

In a two-plate configuration, a top-plate is held above the chip, sandwiching the droplets between them. This not only helps in preventing evaporation, it functions as a continuous grounded electrode that spans every actuation electrode on-device. This top-plate is usually a transparent glass plate coated with indium tin oxide (ITO), which functions as the ground electrode and is biocompatible, nonetheless allowing visual monitoring of on-chip operations from above. As such, a two-plate configuration is more suited to performing the fucosyltransferase inhibition assay on-device as imagined, wherein on-device dispensing would permit the serial dilution of inhibitors to obtain a dose-response inhibition curve.

1.3.4. Theory of droplet movement

In DMF, droplet motion was long described as ElectroWetting-On-Dielectric (EWOD). The first instance of electrowetting-based actuation of liquid droplets for microfluidic application was reported in 2000 by Pollack *et al.*¹⁶⁶ As a recent field, the theories behind its electromechanics and fluid dynamics have yet to be entirely elucidated. Here we present an overview of commonly used models and equations.

Typically, volumes are deposited to the hydrophobic-coated surface of a device in the nanoliter to microliter scale. At rest, the large surface area to volume ratio of these small volumes minimizes inertial and body forces, allowing surface tension to become the dominant force. The study of fluid dynamics on electrowetted devices has resulted in the Lipmann-Young equation,

which describes the effect of applied voltages on the interfacial tension by the change in the angle of contact between the liquid interface and the surface upon which it rests. (Equation 1)

Equation 1) Lipmann-Young equation

$$\cos \theta_v = \cos \theta_0 + \frac{\epsilon_0 \epsilon_i V^2}{2t\gamma_{LG}}$$

In the Lipmann-Young equation, $\cos\theta_v$ is the final contact angle, $\cos\theta_0$ the starting contact angle, ϵ_i is the dielectric constant of the insulating layer (the combination of all layers between the droplet itself and the electrode), ϵ_0 that of a vacuum, and γ_{LG} is the surface tension between the droplet and the medium around it (this can be air). While some have used contact angles to calculate driving force for droplet movement, that model is incomplete; even though increase of contact angle associated with droplet movement is reflected by Lippmann-Young for liquids with higher surface tension, it fails to apply to liquids who are themselves dielectric or who exhibit low surface tension, for which droplet movement can occur without significant contact angle changes.^{167, 168} This is because rather than being a result of a change in interfacial tension, droplet movement is a result of electrostatic pressure driven by excess charge at the three-phase contact line (droplet, surrounding medium, bottom/top plates).¹⁶⁹ This discovery led to the emergence of the term ‘Digital Microfluidics’, and many now prefer to refer to DMF theory by the electromechanical model rather than EWOD.

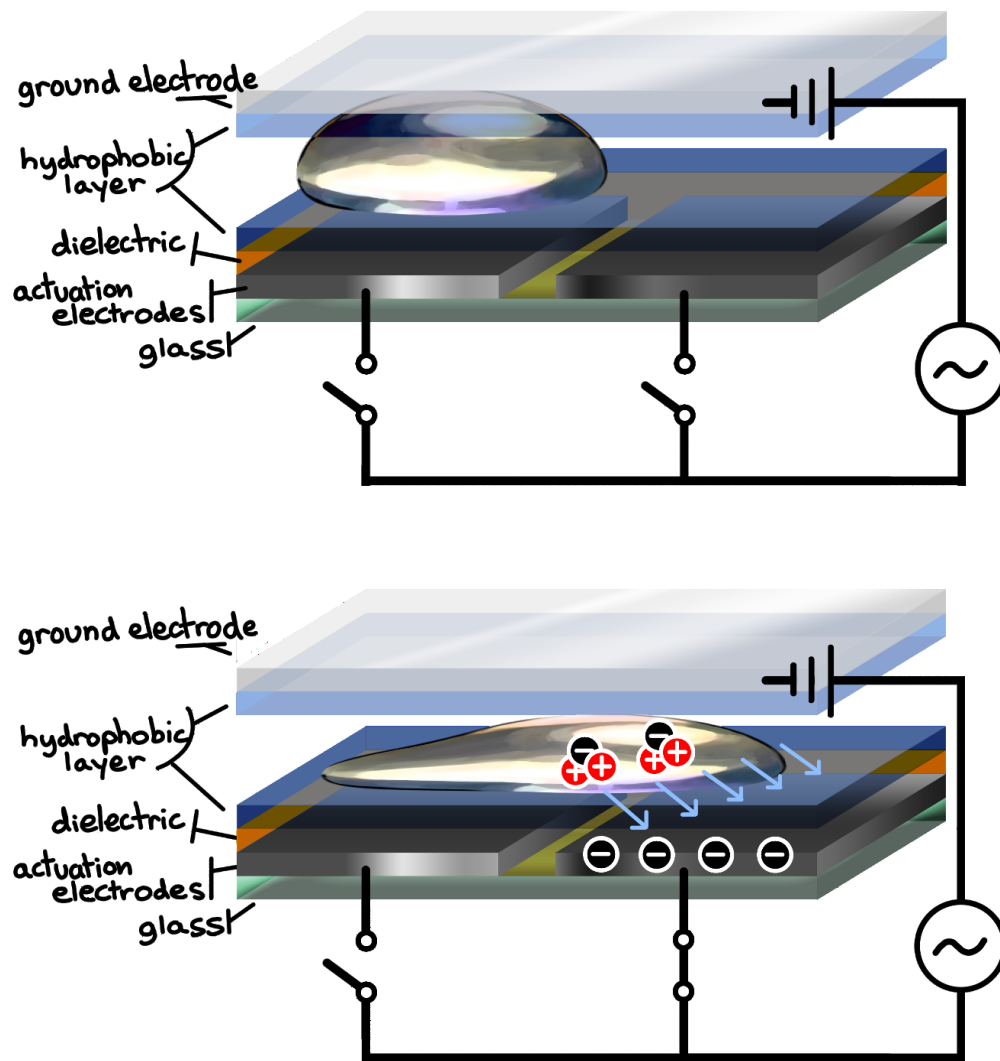


Figure 3) Electrostatic motion of a droplet on a digital microfluidics device

Depiction of droplet motion by electrostatic forces induced upon the application of voltage to an electrode. Top: All switches are open. Bottom: Right-side switch is closed, actuating the right-side electrode.

Dielectrophoresis can be observed at the macro-scale. Just like a stream of tap water bends by the induced static charge in a comb, electrostatic force drives droplet motion: when an alternating potential is applied to an electrode, the electric field around it induce the alternating polarization of the dielectric layer above it. This dielectric layer insulates the droplet from being subjected to electric potential (allowing it to remain electroneutral) while inducing dipole moments for molecules in aqueous solutions, which are then drawn toward the area of high field strength – in other words, the actuated electrode.¹⁷⁰⁻¹⁷² (Figure 3) The polarizability of particles in these droplets subjected to EWOD is given by the Clausius-Mossotti factor (Equation 2).

Equation 2) Clausius-Mossotti factor

$$K(\omega) = \frac{\epsilon_p^* - \epsilon_m^*}{\epsilon_p^* + 2\epsilon_m^*}$$

The Clausius-Mossotti factor measures the polarizability of a spherical particle in a given medium, wherein $K(\omega)$ describes the Clausius-Mossotti factor with the angular frequency ω , ϵ_p^* describes the complex permittivity of the particle, and ϵ_m^* the describes the complex permittivity of the medium.^{173, 174} The complex permittivity of each of these elements is determined by two of its properties: its dielectric constant, ϵ , and its electrical conductivity, σ . (Equation 3)

Equation 3) Complex Permittivity

$$\epsilon^* = \epsilon + \frac{i\sigma}{\omega}$$

In complex permittivity, ϵ represents the dielectric constant (also known as relative permittivity), σ is the electrical conductivity, ω is the field frequency, and i is the imaginary unit $\sqrt{-1}$. By inputting these complex permittivity values to obtain the Clausius-Mossotti factor, it is possible to calculate a dielectrophoretic force for a spherical particle in a given medium.¹⁷⁰⁻¹⁷² (Equation 4)

Equation 4) Time-averaged dielectrophoretic force

$$\bar{F}(t) = 2\pi r^3 \varepsilon_0 \varepsilon_m \text{Re}[K(\omega)] |\nabla |E_{rms}|^2$$

The time-averaged dielectrophoretic force equation applies to spherical particles suspended in a medium, wherein $F(t)$ is the time-averaged force exerted upon the particle, r is the particle's radius, ε_0 is the permittivity (or dielectric constant) of a vacuum, ε_m is the permittivity of the medium, Re is a mathematical symbol designating that the real part of the following imaginary number must be used, $K(\omega)$ is the Clausius-Mossotti factor, and E_{rms} is the root mean-square electric field. This has been used before to calculate the dielectrophoretic motion induced for *E. coli* cells by the actuation of electrodes in a liquid-immersed device, allowing precise cell sorting to distinguish between phenotypes of a bacterial population.¹⁷⁵

However, this only describes the force exerted on suspended particles and does not directly translate into droplet motion in DMF; to do so, one must take into account surface tension and electric-field determinants such as the frequency of the applied voltage. The predominant model used to describe the driving forces of droplet motion in DMF is the electromechanical model. This model uses the frequency of the voltage applied and the droplet position to calculate the total energy of the system, from which force can be derived.¹⁷⁶ (Equation 5)

Equation 5) Electromechanical model for horizontal force acting on a liquid

$$F = \frac{\varepsilon_0 y}{2} \left[\frac{\varepsilon_t \{(v - v_0)^2 - (v - v_2)^2\}}{d'} + \frac{\{\varepsilon_d (v_0 - v_1)^2 - (v_2 - v_3)^2\}}{D} + \frac{\varepsilon_p \varepsilon_t (v_1^2 - v_3^2)}{\varepsilon_p d' + \varepsilon_t d} \right]$$

F is the horizontal force acting on a droplet on a two-plate DMF chip, ε_0 , ε_t , ε_d , and ε_p are the dielectric constants/permittivity of vacuum, the hydrophobic layer, the droplet's media, and the dielectric layer respectively. y is the width of the electrode, and d' , D and d are the heights of the hydrophobic layer, the gap between the two plates, and the dielectric layer, respectively. Finally, v , v_0 , v_1 , v_2

and v_3 are, respectively, the voltages between the top-electrode and top-hydrophobic layer, top-hydrophobic layer and droplet, droplet and bottom-electrode, top-hydrophobic layer and filler medium, and filler medium and bottom-electrode.

From this model, the critical frequency, f_c , can be obtained, which can be used to predict whether or not droplet movement can occur.¹⁷⁶ (Equation 6)

Equation 6) Critical frequency from the electromechanical force model for two-plate DMF

$$f_c = \frac{g_L(C_{pt} + C_t)}{2\pi (C_{pt}C_L + C_tC_L + C_{pt}C_t)}$$

f_c describes the critical frequency in Hz, g_L is the conductance of the droplet, C_L is its capacitance, C_{pt} is the total capacitance added together from the layers between the droplet and the bottom electrode, and C_t refers to the same, but between the droplet and the top electrode (ITO layer on the top-plate).

In a study by Chatterjee *et al.* using similar DMF materials, frequencies ~8 kHz were used at a driving voltage of 100 V_{RMS} to move aqueous liquids.¹⁷⁶ However, protein-rich solutions such as those used for an enzyme inhibition assay exhibit higher viscosity and hydrophilicity, which both impact the ease of movement for the droplet. Higher frequencies in the 10 kHz-15kHz range should then be used; when inserting this range into the equation for force given by the electromechanical model (Equation 5), with Teflon as the hydrophobic layer, parylene-C as the dielectric, and air as the medium between two plates, possible driving voltages for performing the assay-on-chip range from 100-300 V_{RMS} .

1.3.5. The challenges of DMF

Still in early development, many aspects of DMF materials and design remain to be engineered to achieve their full potential. Some of the challenges in the continued development of DMF technology for screening involve increasing throughput¹⁴⁸, minimizing dielectric breakdown^{177, 178}, and reducing the chance of electrode fouling when handling protein-rich solutions.^{179, 180}

Much like the visual display revolution that occurred when LCD displays were invented, many are working on increasing the throughput of DMF by packing more into less. Just like how a pixel in LCD displays is the vehicle for one color at a time, each electrode in DMF is the vehicle to carry one sample- and like how the number of pixels in an image contributes its detail and complexity, the number of electrodes on a device influences the complexity of the experiments that can be held, as well as their throughput. Technologically, DMF is already inherently scalable, as one needs only include more switches and/or increase device area to add more electrodes- but another approach to increasing DMF throughput is to minimize the size of each electrode, which can be achieved by polishing fabrication techniques, and to decrease the number of switches needed for an electrode array by engineering more advanced switches and circuitry.

To minimize dielectric breakdown, in which the insulating layer is worn down between the electrode and droplets resulting in burns to the device, typically a balance is struck in selecting a dielectric layer height that is thin enough to provide a strong electric field to influence droplet movement while being thick enough not to wear down too fast for a device to complete its tasks.¹⁷⁶ This can be further improved by selecting stronger dielectric materials or by reducing the voltages (and thus, the strength of the electric fields) necessitated on devices by improving other factors affecting droplet motility, such as hydrophobicity.

This can also address another of the significant challenges in DMF, biofouling. This occurs when proteins adsorb to the surface of a device, preventing any further movement across those areas. This can be circumvented to an impressive degree by the addition of DMF surfactants and oils. The expansion of this repertoire of additives continues, driven by the need for surfactants compatible with various experimental needs.

Concerning assays that involve many separate steps of component addition, the consistency of dispensed droplet volumes is pivotal. Dispensed droplet volumes and their reproducibility can vary based on multiple factors; the viscosity of the solution, gap pitch and height, ratio between volume in the reservoir and volume on the destination electrode, electrode size and shape, number of serial electrodes in the liquid finger, interfacial tension, and the speed of sequence actuation, among others.¹⁸¹⁻¹⁸³ If volumes dispensed on-device differed, so would the concentrations of assay components in each sample. Specifically for inhibition assays, the ability to obtain inhibition curves is a critical component used to compare the cost and viability of inhibitors, which usually requires concentrations spanning orders of magnitude.

As DMF continues to be characterized, developed with optimized materials, and integrated with other hardware, and as software is eventually written to be universally applicable to any DMF experiment, DMF could one day create a true “lab-on-a-chip”.

Chapter 2. Thesis Objectives

The thesis objectives are; first, to test a hypothetical fucosyltransferase inhibition assay using a synthetic fluorescently labelled disaccharide, MU- β -LacNAc. Secondly, to implement this assay on a microfluidics device.

2.1. Testing a hypothetical inhibition assay using a synthetic fluorescently labelled disaccharide, MU- β -LacNAc

Toward a future goal of screening for potential inhibitors of fucosyltransferases, a fluorescence-based inhibition assay was developed for the fucosylation of the labeled synthetic disaccharide, 4-methylumbelliferyl β -N-acetyllactosaminide (MU- β -LacNAc). MU- β -LacNAc does not fluoresce in itself. Upon treatment with the glycoside hydrolase enzymes including the β -galactosidase from *S. pneumoniae* (BgaA), which catalyzes the hydrolysis of terminal LacNAc on oligosaccharides¹⁸⁴, and *N*-acetylhexosaminidase from *S. plicatus* (SpHex), which hydrolyzes the remaining terminal GlcNAc¹⁸⁵, fluorescent 4-methylumbelliferone (4-MU) is released (Figure 4). However, fucosylation of the labeled oligosaccharide prior to this treatment results in a structure that is not recognized by the glycosidases, preventing hydrolysis and the subsequent fluorescent signal. As such, when the fucosyltransferase is inhibited, the first case in which hydrolysis can occur and its associated fluorescent signal is restored.

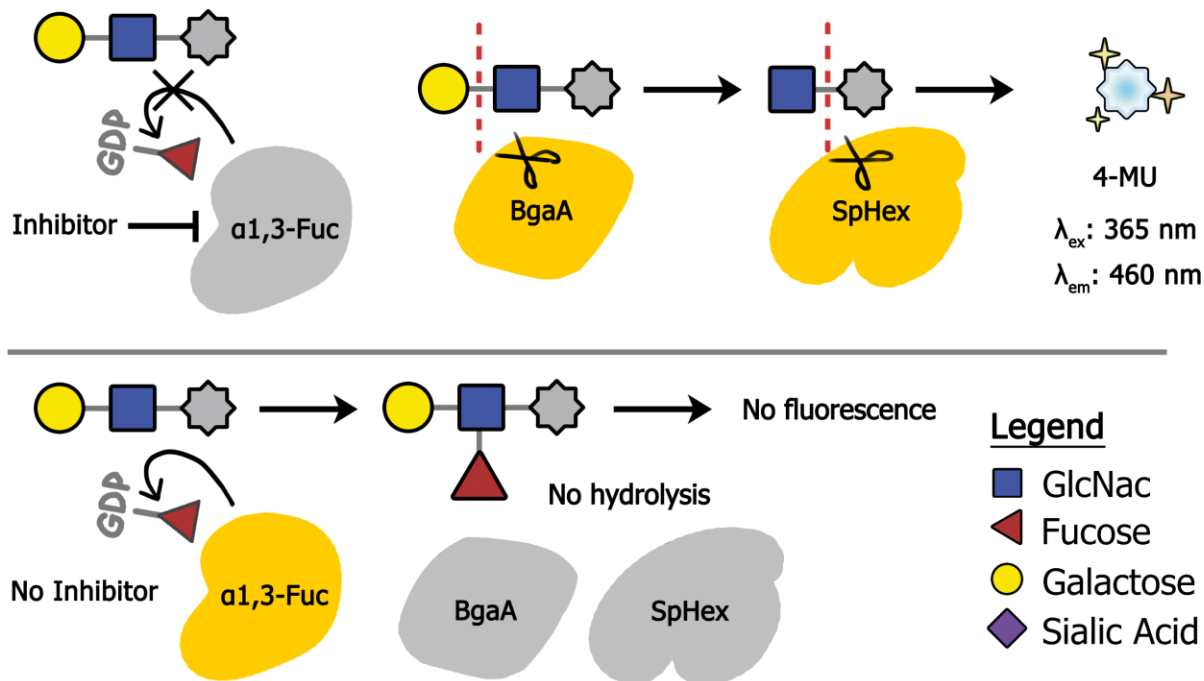


Figure 4) Schematic of MU- β -LacNAc Inhibition Assay

Depiction of the interactions between assay components in conditions with or without inhibitor.

*In the first case, (top), glycoside hydrolases β -gal from *S. pneumoniae* (BgaA) and N-acetylhexosaminidase from *S. plicatus* (SpHex) sequentially cleave fluorogenically tagged disaccharide, MU- β -LacNAc, into its monosaccharide components, releasing fluorescent 4-methylumbelliferone (4-MU). In the second case, (bottom), BgaA and SpHex do not recognize their target, seeing as it has been fucosylated.*

2.2. Implementing the Fucosylation Inhibition Assay on a DMF Device

The next thesis objective involved multiple aspects. First, DMF devices had to be designed, fabricated and tested which could (1) perform serial dilutions on-chip, (2) perform the entirety of the assay on device, and (3) incubate enough samples to produce an inhibition curve of sufficient

range to report IC_{50} values. Besides developing a DMF design with novel electrodes, DMF software, and analytical methods which were then validated, implementation of the assay on the DMF device also entailed making changes to optimize solutions and conditions for this platform regarding droplet movement and the addition of surfactants and oil to assay reagents. These changes were also validated in a series of tests, finally leading to IC_{50} curves for proof-of-concept (GDP) inhibitor in a 384-well plate and on a digital microfluidics (DMF) device. Here, we introduce the integration of a fucosyltransferase enzyme inhibition assay on DMF using an oil-core and air medium. To our knowledge, this setup is only described in two studies;^{186, 187} and although both of these systems were characterized, no biological application was presented or the range of tested concentrations was minimal (only ~one order of magnitude). Here, we describe the first fucosylation inhibition assay performed on DMF using an oil-core with air configuration along with generated proof-of-principle results, showing tested concentration of multiple orders of magnitude for the first time, followed by a comparison to gold-standard techniques (e.g., 384-well plate).

Chapter 3. Methodology

In this chapter, the reagents and materials, as well as the methodologies employed for both the biological and engineering aspects of this project are described in detail.

3.1. Reagents and Materials

Unless specified otherwise, general-use chemicals and kits were purchased from Sigma-Aldrich (St. Louis, MO). Competent *E. coli* BL21(DE3) strains were stored at -80 °C before transformation procedures. Four plasmids were used in this study: pET29-Abg2F6, pET28-BgaA, pET3a-His6-SpHex, and pET21-FucT. Media formulations included 1 L volumes of LB media were prepared with 1 % w/v tryptone, 0.5 % w/v yeast extract and 0.5 % w/v NaCl, then sterilized by autoclave. 100 mL SOC media was prepared by the addition of dry stocks to these final concentrations: 10 mM NaCl, 2.5 mM KCl, 10 mM MgCl₂, 10 mM MgSO₄, 2% tryptone, and 0.5% yeast extract, after which the solution was sterilized by autoclave. Glucose was sterilized through a 0.22 µm syringe filter and added to the SOC media to a 20 mM final concentration. Ampicillin plates were prepared in 10 cm petri dishes with 500 mL LB media with the addition 7.5g agar and 50 µg/mL kanamycin. 100 mM GDP solutions were prepared by dissolving 44.3 mg in 1 mL ddH₂O. 1 M pH 7.5 Tris buffer was prepared by dissolving dry solid Tris in ddH₂O and adjusted to pH 7.5 with the dropwise addition of concentrated NaOH. 500 mM, pH 8.0, EDTA buffer was prepared by dissolving dry solid in ddH₂O with constant stirring on a slightly heated hot plate and gradual adjustment to pH 8.0 with the dropwise addition of concentrated NaOH. 100 mM MgCl₂ solution was prepared by dissolving solid MgCl₂ in ddH₂O. 5 mL 1 M HEPES buffer

was prepared by dissolving 1.192g dry solid in 4 mL ddH₂O, then adding concentrated NaOH dropwise to pH 7.0. 1 mM GDP-Fucose solution previously synthesized by Dr. Ching-Ching Yu and Teng-Wei Tsai at the Chemistry Department at National Chung-Cheng University in Taiwan, was also prepared by dissolving solid in ddH₂O. Solutions used for the fucosylation assay consisted of 80 mM GDP solution, 0.135 mg/mL FucT solution, reaction initiating ‘Glycosylation’ solution (40 mM MgCl₂, 0.04 mM MU-β-LacNAc, 0.08 mM GDP-fucose), and hydrolytic ‘Hydrolysis’ solution (125 mM EDTA, 0.25 mM BgaA, 0.25 mM SpHex). All solutions were prepared with either 50 mM Tris (Proof-of-principle) or 25 mM HEPES buffer (other). With GDP:FucT: ‘Glycosylation’: ‘Hydrolysis’ volumes in the ratio 2:1:1:1, the highest concentration of GDP at the time of the reaction was 40 mM, concentrations in ‘Glycosylation’ mix were at (10 mM MgCl₂, 0.01 mM MU-β-LacNAc, 0.02 mM GDP-fucose), and concentrations of ‘Hydrolysis’ components at the hydrolysis step were of (25 mM EDTA, 0.05 mM BgaA, 0.05 mM SpHex). Except for the proof-of-principle experiments, minutes before the assay, 0.05% Pluronic F68 was applied to 10-12 μL aliquots of each solution.

Microfluidic device fabrication reagents and supplies included chromium-coated glass slides with S1811 photoresist from Telic (Valencia, CA), indium tin oxide (ITO)- coated glass slides, $R_s = 15-25\Omega$ (cat no. CG-61IN- S207, Delta Technologies, Loveland CO), FluoroPel PFC1601V from Cytonix LLC (Beltsville, MD), MF-321 positive photoresist developer from Rohm and Haas (Marlborough, MA), CR-4 chromium etchant from OM Group (Cleveland, OH), AZ-300T photoresist stripper from AZ Electronic Materials (Somerville, NJ), DuPont AF from DuPont Fluoroproducts (Wilmington, DE). Transparency masks for device fabrication were printed from CAD/Art (Bandon, OR) and polylactic acid (PLA) material for 3D printing were

purchased from 3Dshop (Mississauga, ON, Canada). De-ionized (DI) water had a resistivity of 18 M Ω •cm at 25 °C.

3.2. Transformation of Abg2F6, BgaA, SpHex and FucT expression strains

After thawing on ice, cells of *E. coli* BL21(DE3) were incubated in separate 2 mL Eppendorf tubes into which pET29-Abg2F6, pET28-BgaA, pET3a-His6-SpHex, or pET21-FucT was added (see Fig. S1 for plasmid maps). A negative control tube contained cells and a plasmid without the gene insert (e.g., pET28). Before transformation, cells were kept on ice for 5 min, then heat shocked at 42°C for 45 s and returned to ice for 2 min. 1 mL of SOC media was added to each tube, after which cells were heat shocked at 42°C for 45 s and returned to ice for 2 min again. After 1 h of incubation at 37°C, the tubes were centrifuged at 14,000 x g for 1 min. 100-200 μ L of the transformed cells were plated on the LB-agar plates prepared with the appropriate antibiotic selection marker. Plates were left in the incubator at 37°C overnight and colonies were counted after 24 h.

3.3. Protein Expression and Purification for Abg-2F6, BgaA, SpHex and FucT

Colonies of *E. coli* BL21(DE3) transformed with pET29-Abg2F6, pET28-BgaA, pET3a-His6-SpHex or pET21-FucT were picked from their plates and used to inoculate 4 mL volumes of LB containing 100 μ g/mL of their respective antibiotics. Each starter culture was grown overnight at 37°C with shaking at 220 rpm. 400 mL LB was then inoculated with 4 mL of starter culture and grown in the same conditions for 2-5 hours at 37°C until OD₆₀₀ reached ~0.6, at which point

protein expression was induced with 0.1 mM IPTG. BgaA and FucT were expressed overnight at 30°C and SpHex at 25°C, all with shaking at 220 rpm.

Cells were harvested by centrifugation (10,000g, 4°C, 15 minutes), then resuspended in lysis/wash buffer (For BgaA and SpHex: 50 mM Tris; 500 mM NaCl; 7.5 mM imidazole; pH 8. For Abg2F6: 20 mM Tris; 500 mM NaCl; 5 mM imidazole; pH 8. For FucT: 35 mM Tris; 500 mM NaCl; 7.5 mM imidazole; pH 8). Cell suspensions were frozen at -20°C before purification could resume.

After thawing on ice, Lysozyme, DNase I, and RNase A were each added to 5 µg/mL. For each protein, one half of a Roche protease inhibitor tablet (Sigma-Aldrich, Inc.) was dissolved in 500 µL deionized water and then added. Cells were lysed by sonication (Amplitude 25%; Pulse on 5s; off 15s; total time 3 minutes) then centrifuged at 4°C with 15,000×g for 30 minutes. 0.22 µm syringe filters were used to filter each supernatant.

After using 10 mL lysis/wash buffer to equilibrate the 1mL Thermo Scientific™ HisPur™ Ni-NTA Resin cartridges, filtered protein lysates were added to the cartridges and the lysate flow-through collected for later analysis with SDS-PAGE. Once again, 10 mL lysis/wash buffer were added and the wash flow-through collected.

FPLC was performed with an Äkta FPLC System and an increasing imidazole gradient (0 mM to 400 or 800 mM) over 30 mL, collecting thirty 1 mL fractions. This was achieved by gradually increasing the ratio of elution buffer to lysis/wash buffer being pumped into the cartridge. The elution buffers used for BgaA, SpHex and FucT were identical to their lysis/wash buffers with the addition of 400 mM imidazole (BgaA and Abg2F6) or 800 mM imidazole (SpHex and FucT). Lysis/wash and elution buffers were degassed before use. Fractions were stored at 4°C.

After collecting fractions of interest identified by peaks in UV absorbance at 280 nm, SDS-PAGE was performed to identify fractions that contained the protein of interest by their bands (Abg2F6 ~51 kDa; BgaA ~99 kDa; FucT ~55 kDa; SpHex ~55 kDa). Each selected fraction was visually assessed to be $\geq 95\%$ pure. Selected fractions for the same protein were pooled together. Pooled samples were concentrated by centrifugation with Vivaspin® 20 concentrators to < 0.5 mL by spinning at $4200 \times g$ for 16-43 minutes at 4°C . 10DG Desalting columns (Bio-Rad) were equilibrated with 20 mL storage buffer (20 mM Tris, 150 mM NaCl, pH 7.5 for Abg2F6, BgaA, SpHex, and 25 mM Tris, 150 mM NaCl, pH 7 for FucT). Concentrated protein samples were buffer exchanged with storage buffer using the equilibrated 10DG Desalting columns according to the manufacturer specifications and stored at 4°C and -20°C .

Protein concentrations were quantified by BCA assay using the Pierce™ BCA Protein Assay Kit (Thermo Scientific™).

3.4. Enzymatic Synthesis and Purification of MU- β -LacNAc

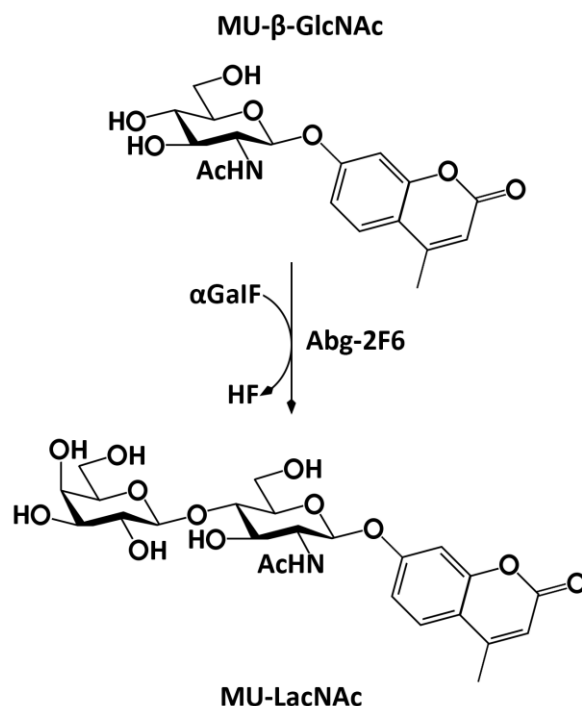


Figure 5) Synthesis of fluorogenic 4-MU tagged oligosaccharide

*MU- β -LacNAc one-pot chemoenzymatic synthesis using the mutant *Agrobacterium* glycosynthase Abg2F6 to catalyze the addition of a Galactose sugar unit from an α -GalF donor to MU- β -GlcNAc, resulting in a fluorogenic 4-MU tagged LacNAc molecule.*

Mutant glycosynthase Abg2F6 from *Agrobacterium sp.* from a directed evolution experiment by Kim et al. was obtained.¹⁸⁸ As in previous work by Kwan et al., Abg2F6 was used *in vitro* to chemoenzymatically synthesize MU- β -LacNAc from 4-methylumbelliferyl N-acetyl- β -D-glucosaminide (MU- β -GlcNAc) and α -GalF⁵⁰ (Figure 5). Briefly, the reaction was performed at room temperature with a solution containing 2.7% DMSO, 0.1 mM MU- β -GlcNAc, 4 mM α -GalF, and 0.5 mg/mL Abg-2F6 in 50 mM pH 7.15 potassium phosphate. Potassium phosphate buffer was prepared to pH 7.15.¹⁸⁹ The reaction was set on a rotating tube rack for 48 h, after which Thin

Layer Chromatography (TLC) was performed to assess the presence of new product. Spots were visualized and circled in pencil under a long-wave UV light lamp, then stained by treatment with p-Anisaldehyde. TLC spots were identified by comparing them to those reported previously, for which NMR characterization had been previously performed.¹⁹⁰ SpHex was added to the solution so as to hydrolyze remaining Glc-NAc. TLC analysis confirmed that the spot attributed to Glc-NAc had been removed. Column purification was performed with a C18 Hypersep™ hydrophobic, reverse phase column (Thermo Scientific™), washed with methanol prior to equilibration with dH₂O. The MU-β-LacNac reaction mix was added, after which 3 fractions were eluted with just dH₂O, then 11 fractions were eluted with increasing concentrations of MeOH by 5% increments. It was observed by TLC that the fractions at 30% MeOH and to a lesser degree, 35% MeOH contained the spot corresponding to MU-β-LacNac; however, a spot thought to be 4-MU impurity was still present on both.

Rotary evaporation was performed with a 40°C water bath gently evaporated MeOH and H₂O from the sample.

Liquid-liquid extraction with Ethyl Acetate was used to further purify the sample; residual 4-MU was separated into the organic Ethyl Acetate layer while MU-β-LacNac was retained in the aqueous layer. TLC verified that high purity was achieved after 4 extractions. MU-β-LacNac was freeze-dried to a final yield of 5.0 mg product.

3.5. Fucosylation Assay in Well Plates

To generate inhibition curves in a well plate, a blank (0 mM GDP) and 6 GDP solutions were manually prepared in four-fold dilutions for their reaction concentrations to range from 40 mM to 0.2 mM. These concentrations were assayed in triplicate, using multichannel micropipettes to simultaneously deliver volumes to the 7 samples (with different concentrations of GDP) of each replicate. The steps for each replicate were as follows, with each replicate started 30 seconds apart: (1) 5 uL FucT solution was added to 10 uL GDP solution and left to incubate for 5 minutes at room temperature. (2) 5 uL Glycosylation mix was added, followed by 10 minutes of incubation at room temperature. (3) 5 uL Hydrolysis mix was added, followed by 5 minutes of incubation at room temperature. (4) Fluorescence readings were taken.

3.6. Fluorescence Readings

3.6.1. Calibration in Well Plates

A Clariostar® Monochromator Microplate Reader (BMG Labtech, Ortenburg, Germany) was used. 4-Methylumbelliferone (4-MU) fluorescence was measured with 40 flashes at λ_{ex} : 360-20 λ_{em} :450-30 in 25°C. Well-plate assays were conducted with Nunc™ 384-Well Polystyrene Black Microplates (Thermo Scientific™). These were utilized in low throughput, using their smaller (~25 μL minimum volume) wells to conserve volumes. Using freshly prepared 4-MU standards with concentrations spanning 2.5 to 25 μM , focal height and gain were optimized by the Clariostar® software every time before measurements were taken.

3.6.2. Reading Fluorescence from DMF chips

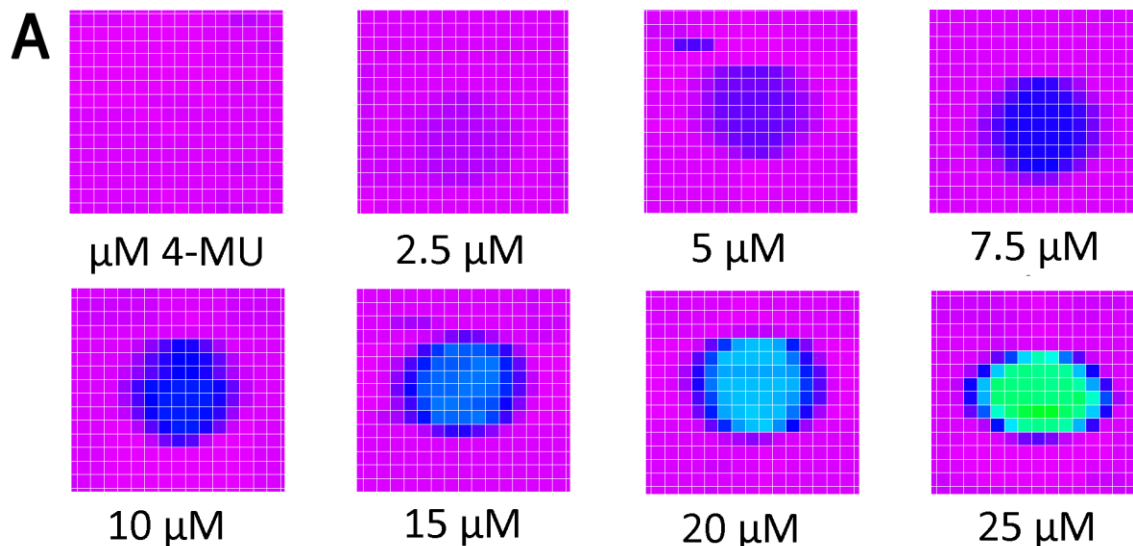


Figure 6) Scan of the surface of a DMF chip mounted on a well plate with fluorescence intensity.

Droplets represented are of a 4-MU standard with known concentrations from 0 μM (top left) to 25 (bottom right) μM , pipetted onto the surface of the chip. Visualized in MARS (©BMG Labtech) data analysis software with a “rainbow” heatmap setting to represent RFU units from low (purple) to high (red). Selected fluorescence readings are highlighted by a square in the center of each droplet.

DMF chip assays were scanned while mounted on the surface of the Nunc™ 384-Well Polystyrene Black Microplates. To obtain a composite fluorescence heatmap of the chip’s surface and droplets, a 96-square-well template was modified on the Clariostar® software to eliminate the gap space between wells. Each pixel represented one fluorescence reading (40 flashes) and every 30x30 pixel ‘well’ scanned represented 10 mm² of the chip’s surface (Figure 6).

3.6.3. Optimization of Settings

Focal Height was determined by scanning in 0.2 mm increments beginning from the height of the microplate (14.40 mm) until the droplets were no longer distinguishable from the chip by their fluorescent signal (17.9 mm). A favorable focal height was selected at 15.80 mm. A gain of 750, at which the lowest concentration of the 4-MU standard (2.5 μM) would be distinguishable, was chosen.

3.6.4. Normalization and Analysis

After optimizing settings, fluorescence heat maps could be obtained in the Clariostar's MARS (©BMG Labtech) data analysis software. However, the fluorescence exhibited by certain elements on the chip, namely the double-sided tape used to hold the top-plate in position, was far above the highest droplet fluorescence readings. Only by using a rainbow gradient for visualization with a manually set upper threshold of 40000 fluorescent units out of the maximum signal, 260 000, was it possible to visualize droplet positions within the data, after which areas of interest could be selected before porting data to Excel.

Analysis of DMF scans was done by taking the average of areas selected at the center of each droplet and zeroing them on the blank, defined as the average of background readings found at "empty" (no droplet) locations on a chip. In the case of pure water, readings were indistinguishable from the blank.

3.7.Automation Hardware Setup

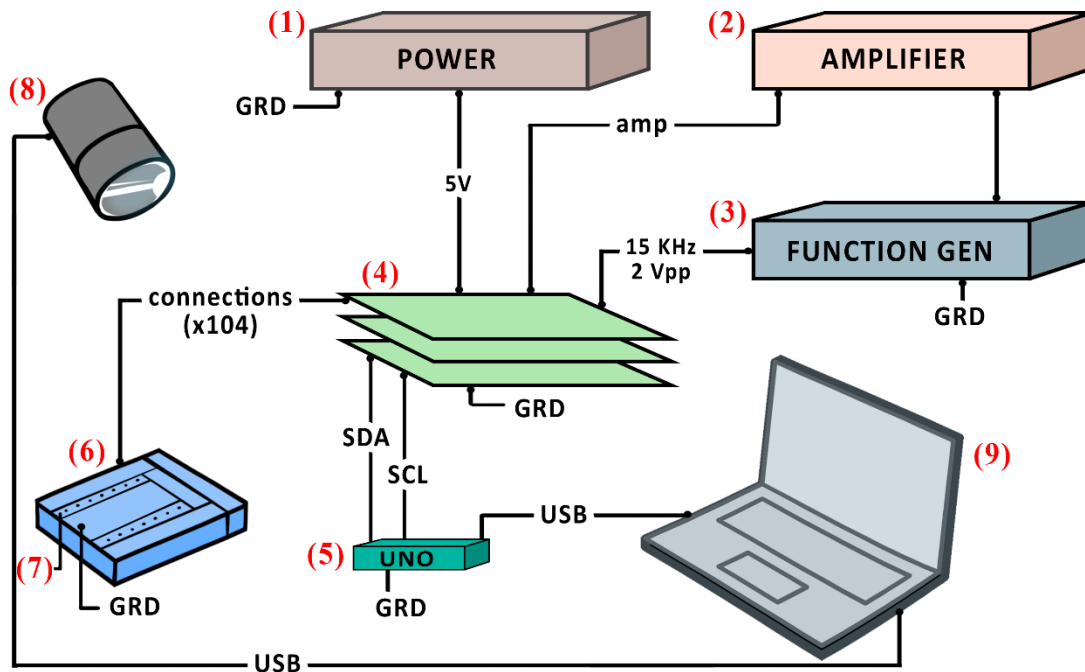


Figure 7) Automation system diagram

Diagram of DMF hardware and its connectivity labeled with 1. Power Supply, 2. Amplifier, 3. Function Generator, 4. Control Boards, 5. Arduino, 6. Contact Apparatus, 7. DMF chip, 8. Camera, 9. Laptop

The automation system consists of Python 2.7 softwares (described separately) used to control an Arduino Uno microcontroller (Adafruit, New York, USA). Driving input potentials of 160-220 V_{RMS} were generated by amplification of a square wave output from a function generator (Agilent Technologies, Santa Clara, CA) operating at 15 kHz by a PZD-700A amplifier, (Trek Inc., Lockport, NY) and delivered to the PCB control board. The Arduino controls the state of high-voltage relays (AQW216 Panasonic, Digikey, Winnipeg, MB) that are soldered onto the PCB control board. (Figure 7) The logic state of an individual solid-state switch is controlled through

an I²C communication protocol by an I/O expander (Maxim 7300, Digikey, Winnipeg, MB). This control board is mated to a pogo pin interface (104 pins), where each switch delivers a high-voltage potential (or ground) signal to a contact pad on the DMF device. See our GitHub registry (<https://github.com/shihmicrolab/Automation>) to assemble the hardware and to install the open-source software program to execute the automation system. Droplets operations were visualized by a 3.0 MP CMOS Color USB camera (EO-3112C, Edmund Optics, New Jersey, USA) attached to a 10× C-mount close focus zoom lens (54363, Edmund Optics, New Jersey, USA).

When switching an electrode on and in so doing, subjecting it to electric potential, the coating of parylene-C on the device acts as a dielectric layer allowing electrostatic force to induce the rapid movement of on-chip volumes without subjecting them directly to a voltage.¹⁹¹ Droplets were grounded via contact with an Indium Tin Oxide (ITO)-coated glass plate placed onto the chromium electrode-bearing bottom plate, joined by two layers of selectively placed double sided tape to a gap height of approximately 210 μm, measured by caliper.

3.8. Fabrication of Digital Microfluidics Chips

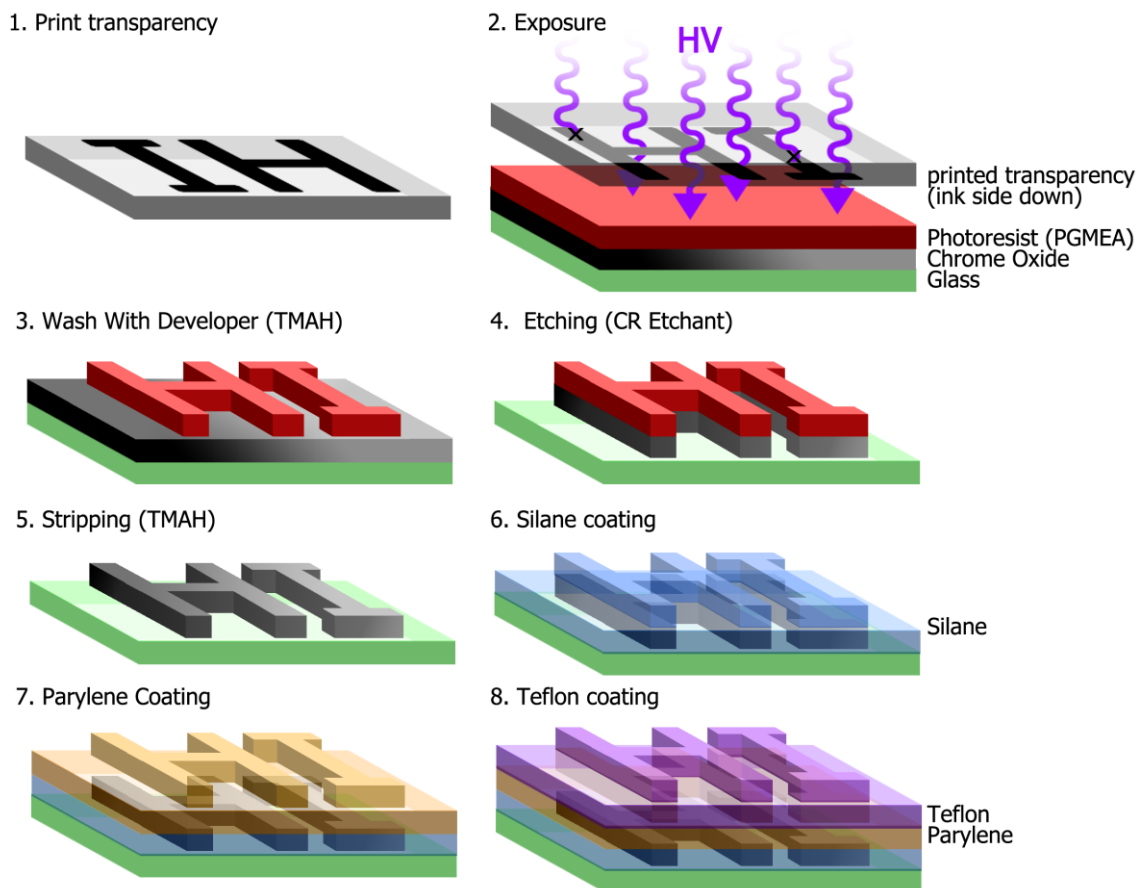


Figure 8) Photolithographic fabrication

A DMF device at different stages of photolithographic fabrication in a clean-room. (1) A transparency printed with dark ink. (2) Exposure under UV light with a superimposed transparency solubilizes PGMEA to TMAH (3) After TMAH stripping and baking on a hot-plate, photoresist only remains in the ink area of the transparency (4) Chromium Etchant strips the chromium oxide which is unprotected by photoresist (5) A different TMAH stripping solution is used to remove remaining photoresist (6) Silane is coated to aid parylene in bonding (7) Parylene is deposited (8) Teflon is spin-coated, ending the fabrication.

Photolithography was used to fabricate DMF chips in a cleanroom. (Figure 8) The 2x3 inch DMF design was prepared in AutoCAD. The transparency was printed by CAD/Art Services Inc. (Bandon, OR), with a minimum guaranteed feature size of 10 μm . 2x3 inch Glass slides metallized with chrome oxide and coated with AZ-1500 photoresist (1-methoxy-2-propanol acetate, or PGMEA) were ordered from Telic Company (Valencia, CA). These were exposed together for 5 seconds to UV light. This solubilizes the photoresist, allowing it to be washed away in the next step.

The solubilized photoresist was removed with MF-321 developer acquired from Rohm and Haas Company (Marlborough, MA). Etching was performed with CR-4 chromium etchant from OM Group Inc. (Cleveland, OH). AZ-300T from AZ Electronic Materials plc (Somerville, NJ) was used for stripping.

DMF devices were primed for 15 minutes with 50:50:1 *deionized water : isopropanol : silane* solution, seeing as silane enhances the bonding of plastics such as parylene to silicates such as the glass surface of the chip. Contact pads on the DMF devices were then covered with heat-resistant tape. The SCS Labcoter 2 PDS 2010 from Specialty Coating Systems Inc. (Indianapolis, IN) was used for the chemical vapor deposition of Parylene-C, after which further steps were performed outside of the clean room.

CG-611N-S207 ITOs (Indium tin oxide coated glass slides) were acquired from Delta Technologies Limited (Loveland CO). 1% Teflon was prepared by baking dry pellets in FC-40 from Sigma-Aldrich at 65°C for 5 days followed by 0.22 μm syringe filter sterilization. A WS-650 Spin Coater from Laurell Technologies Corporation (North Wales, PA) was used to apply a Teflon hydrophobic coating to both the device and the ITOs.

Two layers of double-sided tape were used to adhere the ITO to the DMF chip. Gap height was measured by caliper, subtracting the height measured for each of the individual plates from the total height measured where the two plates and the tape.

3.9. Design, Fabrication and Operation of Digital Microfluidics Devices

3.9.1. Design and operation of chip

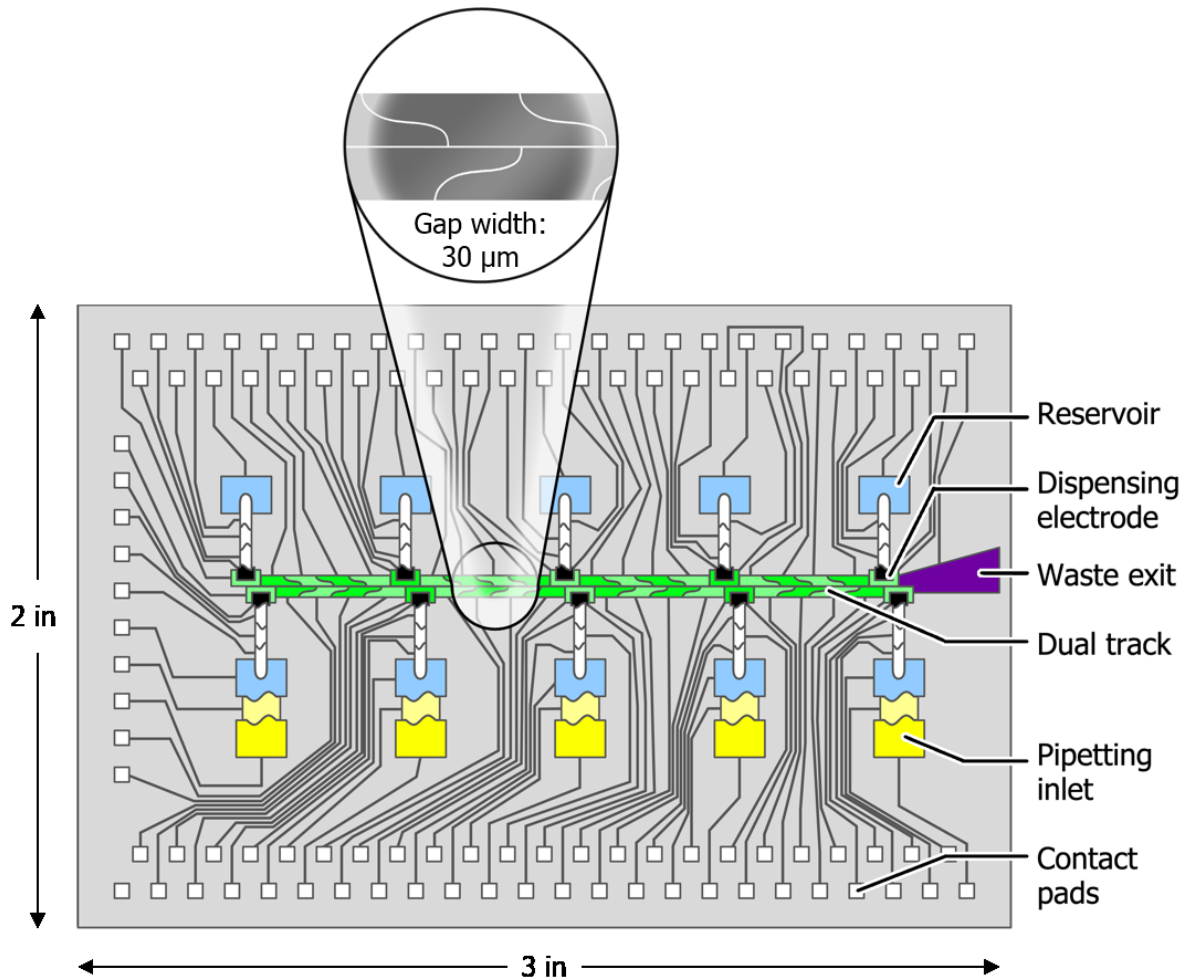


Figure 9) Design of DMF Device

Schematic of the electrode layout of the DMF design created to run the inhibition assay. The 2x3 inch digital microfluidics chip design comprised 103 electrodes among which a waste collection electrode, two adjacent tracks connecting every section, and 10 reservoirs, 5 of which included pipetting inlets. A zoomed-in view of a skewed-wave electrode used on the track is shown.

As shown in Figure 9, the device layout designed in AutoCAD featured an array of 93 actuation electrodes (9 types, various sizes) connected to 10 reservoir electrodes (2 variants, 4.1 x 3 mm ea.), with an average of inter-electrode gap size of 30 μm . Each electrode was connected to a square contact pad at the edge of the chip using 70 micron wide lines; when the devices were mounted, each of these contact pads would be in contact with a pin connected to the electrical setup.

Aqueous solutions could be pipetted directly onto the reservoirs before the ITO was affixed to the chip. Removal and addition of volumes to device mid-operation was achieved by pipetting to one of 5 strategically exposed electrodes on the edge of the ITO. The electrodes, for which a third of the surface area is positioned under the ITO, could pull droplets underneath the ITO whenever actuated. (Figure 10) Generally, all droplets containing proteins were supplemented with 0.05% Pluronic F-68. The pipette tips used to dispense these volumes to the chip were first coated in silicone oil by pipetting the oil in and back out of the tips. Waste and unused fluids were removed by delivering them to reservoirs and removed using paper strips at the waste reservoir.

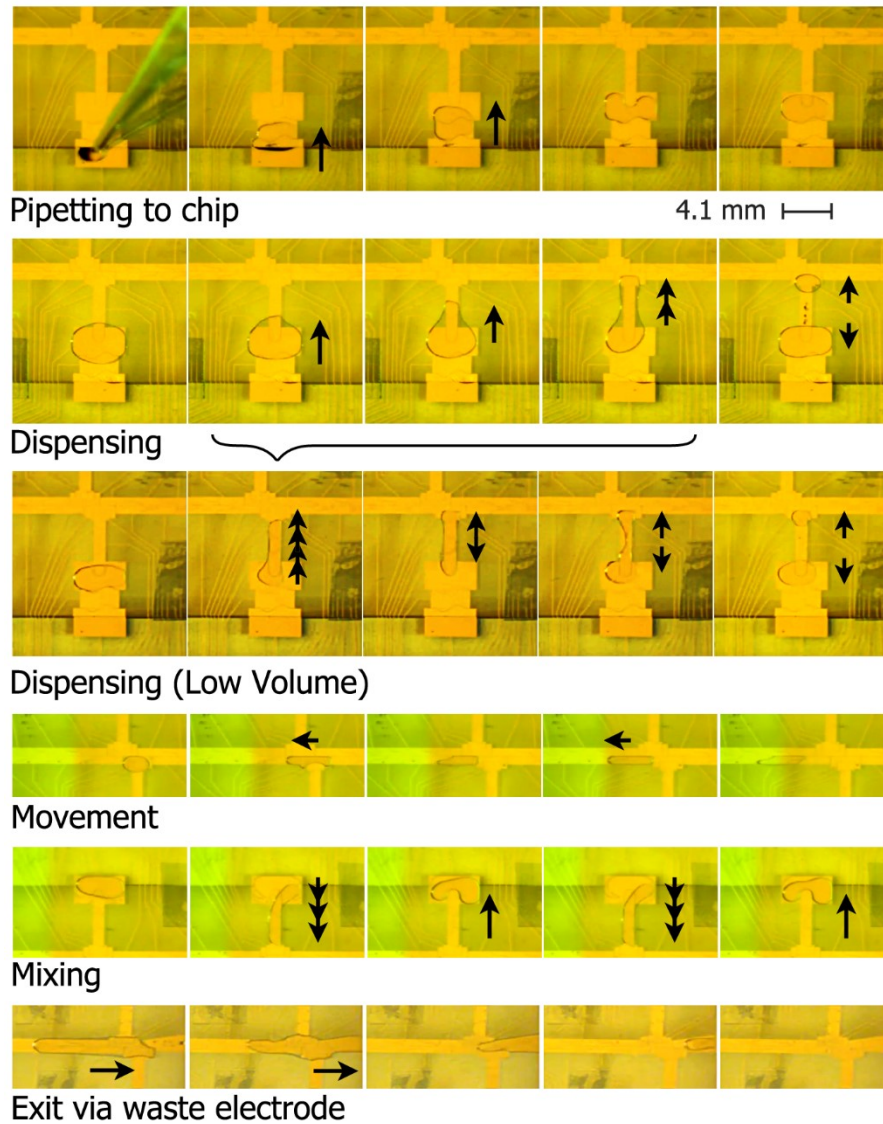


Figure 10) Volume manipulations on DMF device

Camera images of the types of operations (ex.: dispensing, mixing...) performed on the digital microfluidic device.

Several types of sequences were made with the software for each location on the chip so that droplets could move, mix, or be dispensed on demand. These sequences were used to run the enzyme inhibition assay on-device, using the steps as described in Figure 11.

3.9.2. Fucosylation inhibition assay on a DMF device

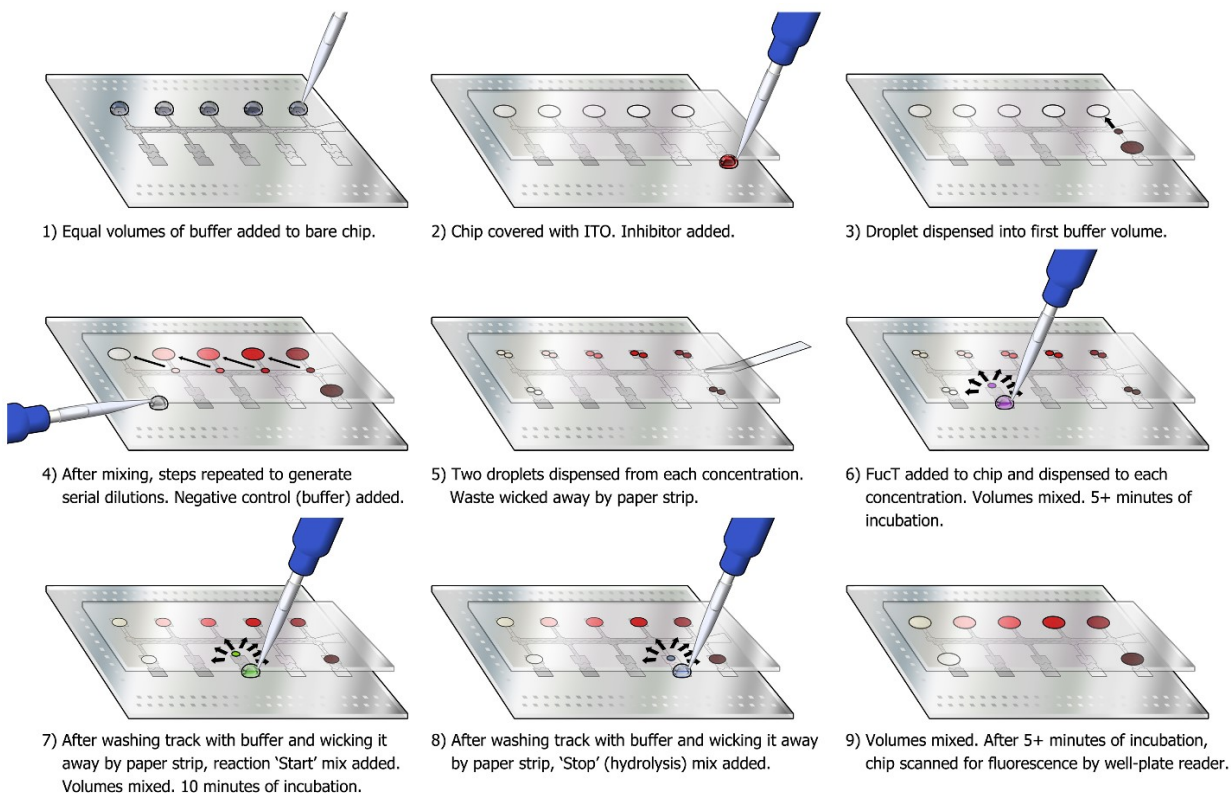


Figure 11) Illustrated protocol for performing the assay on-chip

1-5: Serial dilution spanning up to 3 orders of magnitude within 5 dilutions. 6: Addition of Fucosyltransferase to inhibitor followed by 5+ minutes of incubation allowing the inhibitor to bind. 7: Addition of MU- β -LacNAc to the solution, which results in its fucosylation depending on the degree of inhibition attained in the previous step. 8: Introduction of a reaction stopping mix which consists of EDTA, SpHex and BgaA; EDTA to prevent further Fucosyltransferase activity, and the glycoside hydrolases to sequentially cleave unfucosylated MU- β -LacNAc into its monosaccharide components. 9: After 5+ minutes of incubation, chip scanned for fluorescence by well-plate reader. (See video of one assay-on-chip run uploaded at:

<https://www.youtube.com/watch?v=Ehot1basdzM>)

To obtain inhibition curves from assays performed on-chip, DMF chips were used to prepare 6 GDP solutions for reaction concentrations ranging from 40 mM to an estimated ~ 0.008 mM from performing serial dilutions of an estimated ~ 5.5 -fold per step on-chip. All solutions had 0.05% pluronics F68 added to them prior to the beginning of the experiment, and pipette tips were coated in silicone oil before being used to dispense the solutions.

A 28-step protocol was used (Figure 11). The steps were as follows: (1) Five 2.7 μ L droplets of 25 mM HEPES buffer were manually pipetted onto the reservoirs after which the ITO plate was placed on top of the device. (2) A 3.1 μ L droplet of the inhibitor (i.e. 80 mM GDP) was added to the edge of the ITO (aligned with a reservoir electrode) and the droplet was loaded into the reservoir by applying a driving potential on the reservoir. (3) A one-unit droplet of GDP-fucose (~ 500 nL) was dispensed from the reservoir. (4) The dispensed droplet was brought to one of the reservoirs already primed with 2.7 μ L buffer and mixed twice (this was done by pulling the liquid out of the reservoir gradually along a linear path, then actuating the reservoir electrode to pull the entire volume back in one step.) This created an average serial dilution of ~ 5.5 -fold. (5) A unit droplet of the dilution was dispensed. (6-9) Steps 4-5 were repeated with the subsequent buffer-containing reservoirs to generate a total of five different inhibitor concentrations (~ 14.5 , ~ 2.64 , ~ 0.48 , ~ 0.087 , ~ 0.016 mM) in addition to the 80 mM starting concentration. (10) A 3.1 μ L droplet containing the negative control (25 mM HEPES buffer, without inhibitor) was added to an empty reservoir (as in step 2). (11) Two one-unit droplets (~ 500 nL each) were dispensed from each of the 7 filled reservoirs and moved aside to merge into a two-unit droplet (~ 1 μ L) and clear the way for the leftover volume droplet to exit the reservoir. (12) The leftover volume droplet was moved to the waste electrode, where it was wicked away by a paper strip and disposed of off-chip. (13-18) Steps 11-12 were repeated for the

other 6 concentrations of GDP (incl. 0 mM). (19) A 3.1 uL droplet of FucT was added to an empty reservoir (as in step 2) and a one-unit droplet was dispensed and mixed with the two-unit droplets containing inhibitor. (20-25) Step 19 was repeated for the other 6 concentrations of GDP (incl. 0 mM). (26) 5 or more minutes after step 19 for each droplet (+/- 1 minute between samples but all >5 min allowing the inhibitor enough time to bind), Glycolysis solution was added to each droplet (as in steps 19-25). (27) After 10 minutes of incubation, Hydrolysis solution was added to each droplet (as in steps 19-25). (28) After 5 minutes of incubation, fluorescence readings could be taken. (Occasional Steps) At any point during the run of the assay, when impurities were suspected on the common surface (main linear track) of the chip (ex.: a small residual droplet left on the track, dust having slid under the ITO), buffer was introduced to an empty reservoir (as in step 2) and used to wash the track before it was actuated to waste and removed with a paper strip, after which chips could be scanned by the well plate reader.

3.9.3. Software setup

Four software programs were used to execute the droplet operation protocols. ArduBridge.py, scripted by Guy Soffer, provided the framework for the Arduino to interpret actuation instructions and to switch the target pin(s) to its high voltage state for a specified time. This framework also used the pySerial.py open-source module¹⁹² to access the USB port and communicate with the Arduino. ArduBridge commands included `setup.seq['x'].start('y')`, in which `x` is the name of the sequence and `y` is the number of times to actuate it, and `setup.stop()`, which were inputted into the Python shell.

Protocols and sequences were stored in a .py (Python) script in which users could define names, lists representing sequences of electrodes to actuate, the length of their actuation ('onTime'), and the time between the actuation ('period') of each electrode or set of electrodes in a sequence. Users could use this script to customize and input their own additional functionality into ArduBridge. Here, a GUI was created (called LLGUI) to be used as an interface for ArduBridge, providing buttons for each sequence with which actuation script was copied to the clipboard for ease of input to the shell.

A program called Pasemaker.py was created to construct electrode sequences for automation on any DMF design.

3.9.4. Software operation: Running an assay-on-device

While this only has to be done once, electrode actuation sequences must be prepared before running an experiment on-chip. To do this, one must first create a .csv (comma-separated values) file representing the layout of the chip's electrodes. A csv file can be written in Notepad,

any script writing program, or programs that can save as csv (ex.: Microsoft Excel). The electrodes do not need to be listed in order, but if there is bussing on the design, each bussed electrode must be listed on a separate line/row (Figure 12).

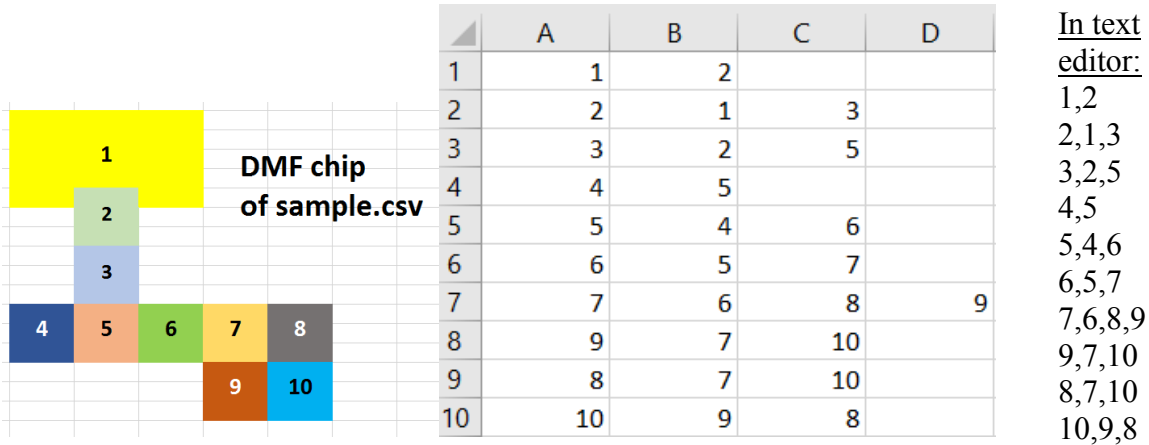


Figure 12) Example of a DMF device and its corresponding .csv

Diagram of the electrode layout of a sample device (left) comprising 10 electrodes and its corresponding input .csv files either written in a spreadsheet (center) or text editor (right).

In a spreadsheet, each electrode is listed in the first column, and subsequent numbers in adjacent columns are the numbers of the electrodes connected to it.

In a text file, each electrode is listed on a separate line, then the numbers of the electrodes connected to it are listed on the same line, separated by commas.

PaseMaker is a homebrew software developed for sequence construction and formatting for integration with other softwares. As a python script, it can be opened in IDLE. When File>Load is selected, the file browser appears and asks for a csv file to load into the program, which then automatically generates a graph from the file (Figure 13).

Using the text formatter, it was possible to efficiently change up to six substitutable values. Here, the text formatter was primed with text formatted for compatibility with ArduBridge automation.

The substitutable values defined were {1} the name of the category to file that sequence under {2} the name used to identify the sequence, which was different for every sequence {3} the description of the sequence, unnecessary if the sequence name and category already serve as sufficient identification {4} the amount of time (in seconds) the electrodes remain in the ON (actuated) state and {5} the period (in seconds) given to each actuation step of the sequence.

To generate a sequence, the fields for 'Electrode A' and 'Electrode B' must be filled with the electrode numbers designating the start and end destination electrodes, or the electrodes at the two extremities relevant to the sequence being constructed. PaseMaker solves the shortest path between those electrodes and copies the formatted text string including that sequence to the clipboard. (Figure 13)

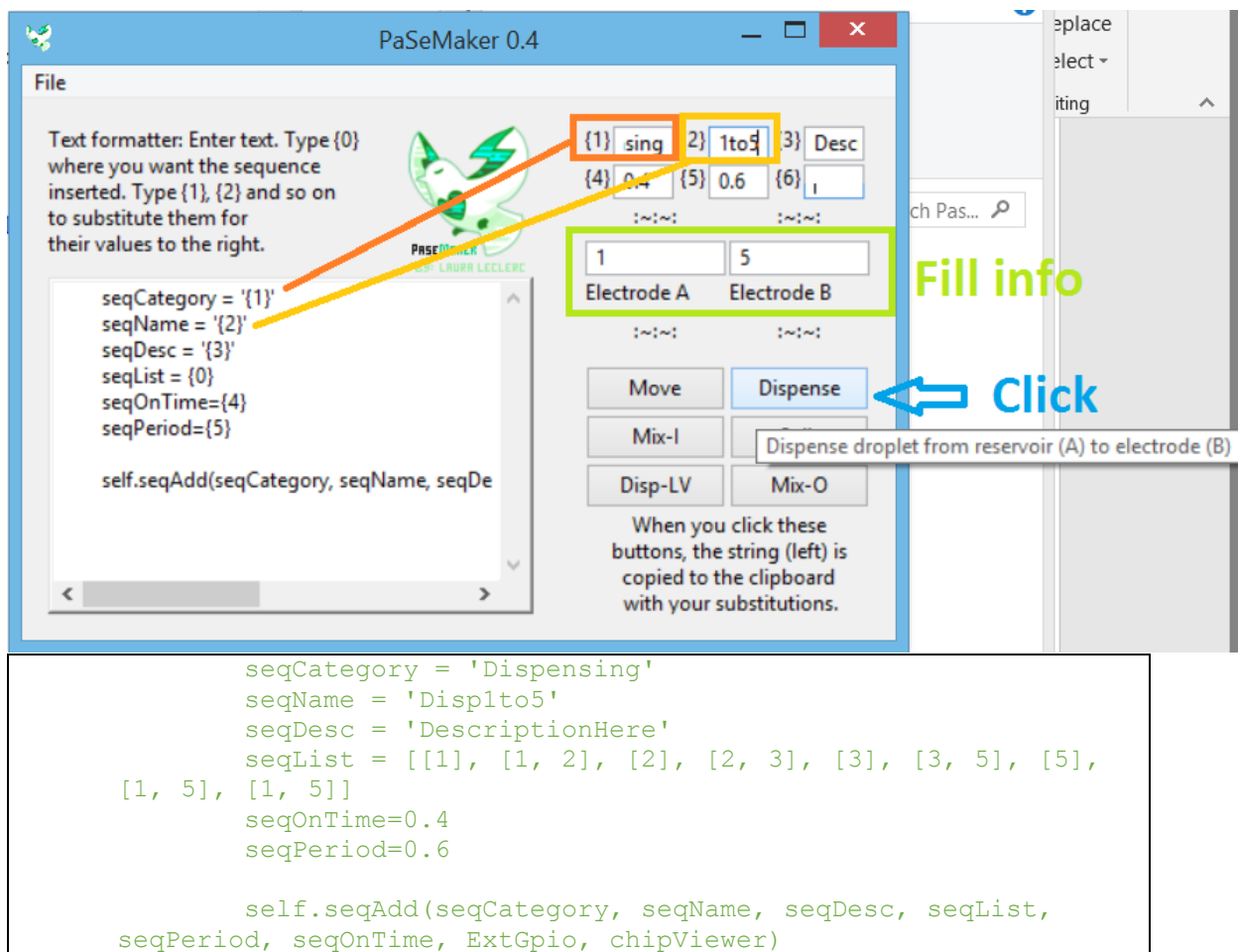


Figure 13) PaseMaker sequence construction example

Example of sequence generation using PaseMaker. PaseMaker interface with text formatter (left) is primed with text formatted for the automation system's ArduBridge software, and its substitutable values (top right) are primed with desired values. Here, the fields for Electrode A and B were assigned the values 1 and 5 to create a sequence which dispenses from electrode 1 to electrode 5. (Top) The resulting text is generated and copied to one's clipboard in a split-second. (Bottom)

After all sequences needed for the assay had been constructed this way, they were added into a python file in IDLE, referred to as the protocol file. This is a file necessary for ArduBridge

automation software to run. Until this step, every step only had to be done once. The next steps preceded every experiment.

Once the protocol file contained all of the assay sequences, it was opened with LLGUI.exe.

Opening LLGUI.exe makes the file browser pop up, so that one can find and select the protocol file. LLGUI reads the protocol and constructs a button interface with each buttons, representing a sequence, grouped under their category. Each category is initially collapsed. Clicking a category shows the buttons. (Figure 14)

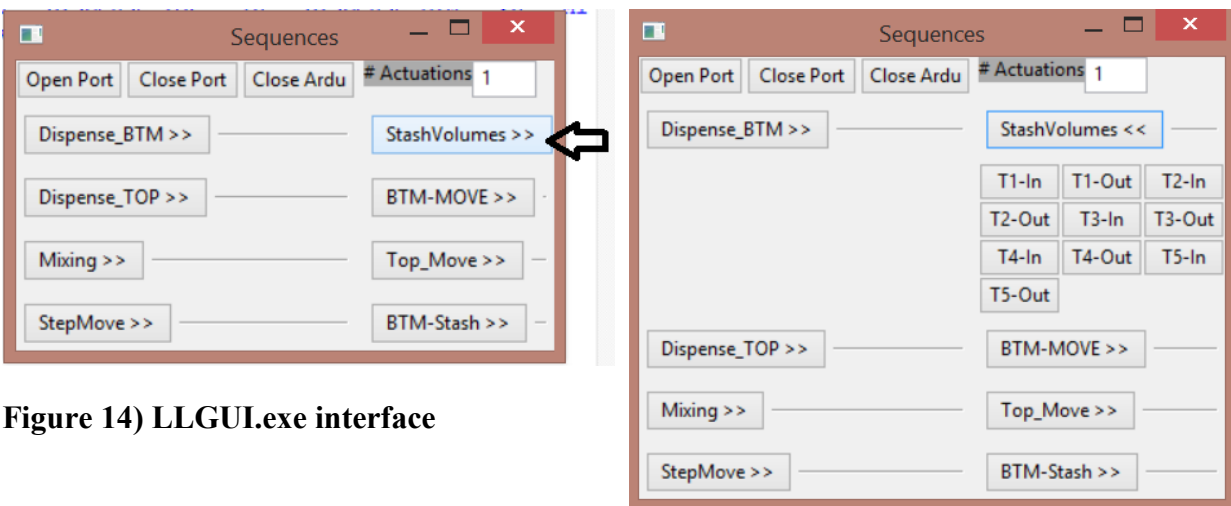


Figure 14) LLGUI.exe interface

Each button represents a sequence. Every sequence is grouped under its category. Clicking a category will open or collapse that category. The number of times the sequence will be run is determined by the number entered into the #actuations text field (top right). The Arduino or its USB port can be closed or opened using the Open Port, Close Port, and Close Ardu buttons.

Before beginning the experiment, unless this was already done and no other sketch had been uploaded since to the Arduino UNO, the compiled automation sketch was uploaded as a HEX file using an anonymously authored freeware bootloader program, XLoader.

The camera's visualization software (uEye Cockpit) was opened to size and position the window before initializing the camera. (Figure 15)

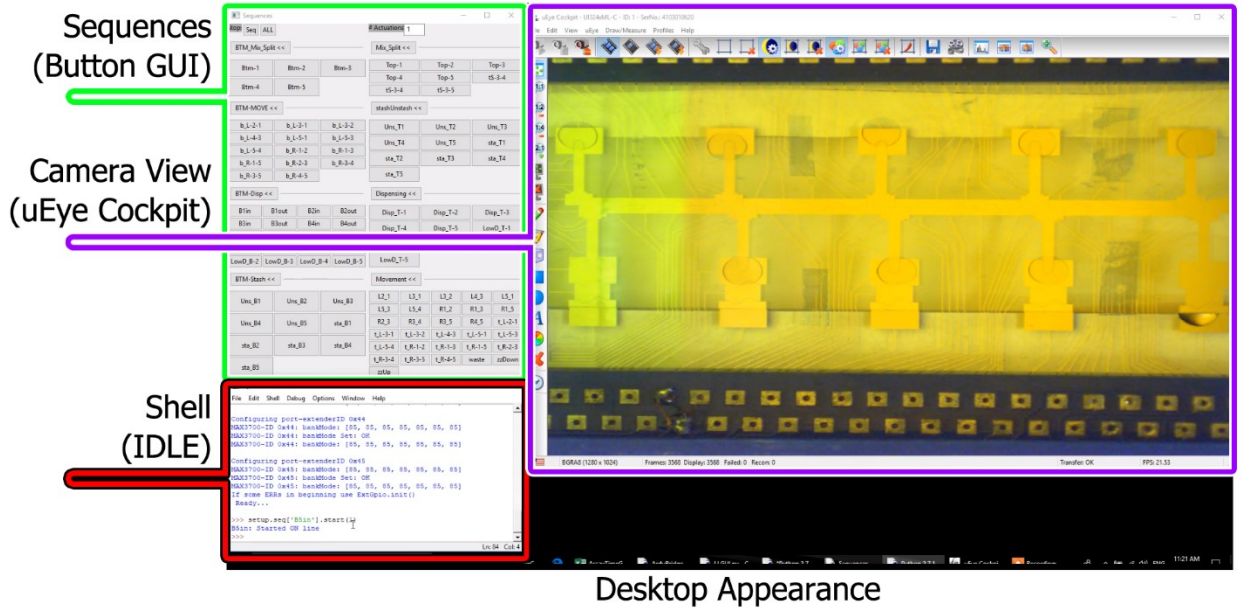


Figure 15) Desktop during a DMF experiment

Screenshot of desktop appearance during an experiment with python-based GUI, python shell, and uEye camera software.

Finally, ArduBridge could be opened in IDLE and run. However, there are differences that must be verified between users. First, the user's choice of protocol file must be in the same folder as Ardubridge. Secondly, the user's protocol filename and the comport specified for the Arduino has to be correct. These details are specified and changed by the user in the ArduBridge script, which can be opened in IDLE (Figure 16).

```
ArduBridgeLL.py - C:\Users\Lore\OneDrive - Concordia University - Canada\Python\U...
File Edit Format Run Options Window Help

import time

from GSOFArduBridge import ArduBridge

from GSOFArduBridge import ElectrodeGpioStack
from GSOFArduBridge import threadPID
from GSOFArduBridge import threadElectrodeSeq
from GSOFArduBridge import UDP_Send
#import UdpToConViewer

import LLprotocol

if __name__ == "__main__":
    udpSendPid = UDP_Send.udpSendPid
    udpSendChip = UDP_Send.udpSendChip
    port = 'COM9'
    baudRate = 115200
    ardu = False
    ExtGpio = False

    ardu.gpio.pinMode(2,0)
    print 'type PID.start() to start the PID t
    ""
    setup = LLprotocol.Setup(ExtGpio=ExtGpio,
    setup.enOut(True)

at bottom of script
```

Figure 16) ArduBridge script by Guy Soffer

Highlighted areas of the ArduBridge script which need to be changed between users and automation protocols.

Chapter 4. Assay Validation

This chapter consists of work done in well plates to validate the MU- β -LacNAc assay. First, its ability to produce fluorescent methylumbelliferone upon hydrolysis is verified, after which inhibition of hydrolysis by fucosylation is tested. Enzyme concentration is optimized, followed by testing the inhibition of fucosyltransferase by GDP to produce an inhibition curve and measure IC50.

4.1. Testing the Hydrolysis of MU- β -LacNAc

To confirm the functionality of the assay as well as optimize certain conditions, SpHex and BgaA were tested for their ability to hydrolyze MU- β -LacNAc. In a 384-well-plate, a solution with 10 μ M MU- β -LacNAc, 50 mM Tris (pH 7.5), and 10 mM MgCl₂ was incubated for 10 minutes with either, neither or both of BgaA and SpHex at 0.05 mg/mL concentrations. It was demonstrated that SpHex and BgaA must both be included in the reaction to release a signal equivalent to ~6 μ M fluorescing 4-MU from 10 μ M MU- β -LacNAc. (Figure 17)

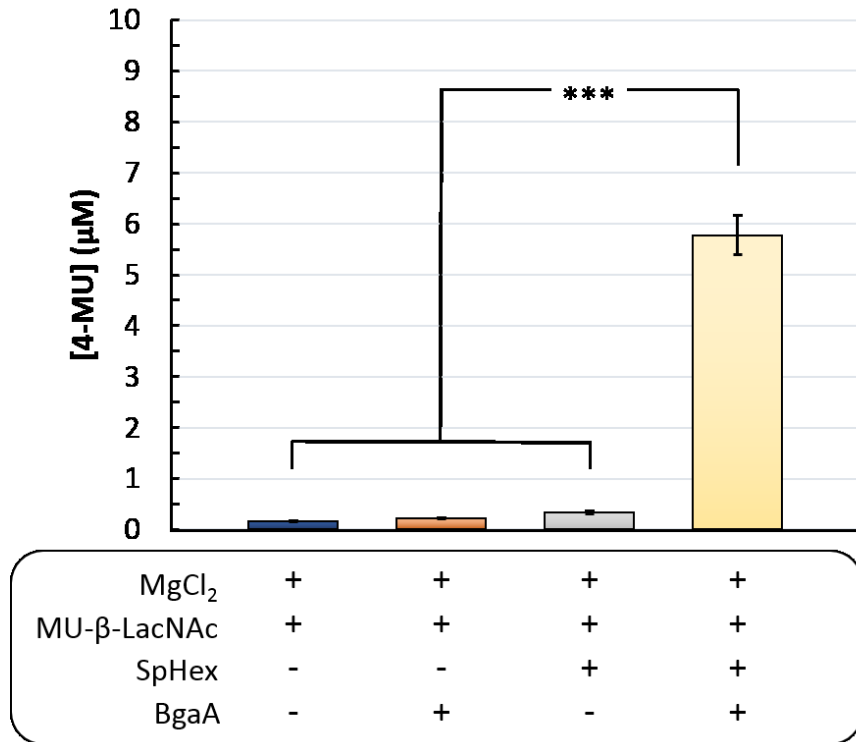


Figure 17) The hydrolysis of MU-β-LacNAc by BgaA and SpHex

Bar graph reporting fluorescence of samples incubated either without, with one or with both of the Glycoside hydrolases β-gal from *S. pneumoniae* (BgaA) and N-acetylhexosaminidase from *S. plicatus* (SpHex). Glycoside hydrolases sequentially cleave synthetically methylumbelliferated disaccharide, MU-β-LacNAc, into its monosaccharide components, releasing fluorescent 4-methylumbelliferone (4-MU). Equivalent 4-MU concentrations for fluorescent signal was calculated by 4-MU standard curve. Experiments done in triplicate in a 384-well plate. Error bars represent standard error. *** : $p < 0.01$. (n=3)

4.2. Optimization of Enzyme Concentration and Hydrolysis Incubation Time

Optimal FucT concentration and hydrolysis reaction times were determined using the Clariostar® well-plate reader. With a negative control (0 nM FucT), seven concentrations of FucT were tested, spanning 1.248 nM (~0.07 mg/mL) to 0.089 nM. 770 uL each of 'glycosylation' and 'hydrolysis' solution were prepared and primed into separate injectors. 11 uL of negative control and every FucT concentration was added to each well in advance, in triplicate. Clariostar® settings were created to automatically inject 'glycosylation' solution at the 5 minute timepoint for each well. 10 minutes later for each well, hydrolysis solution was machine injected, after which fluorescence readings began; 10 timepoints were taken each 1 minute apart and it was observed that fluorescence for each of the FucT concentrations reached a plateau in 5 minutes (Figure 18). Given these results, 5 minutes was selected as the minimum length of the assay's hydrolysis step. A FucT concentration of 0.03 mg/mL, or 0.6 nM, was also chosen, given that the maximum fluorescent signal given by that concentration was sufficiently lower (20%) compared to the same reaction in the absence of FucT, providing a wide effective range of fluorescence for the assay to distinguish between the strength of inhibitors.

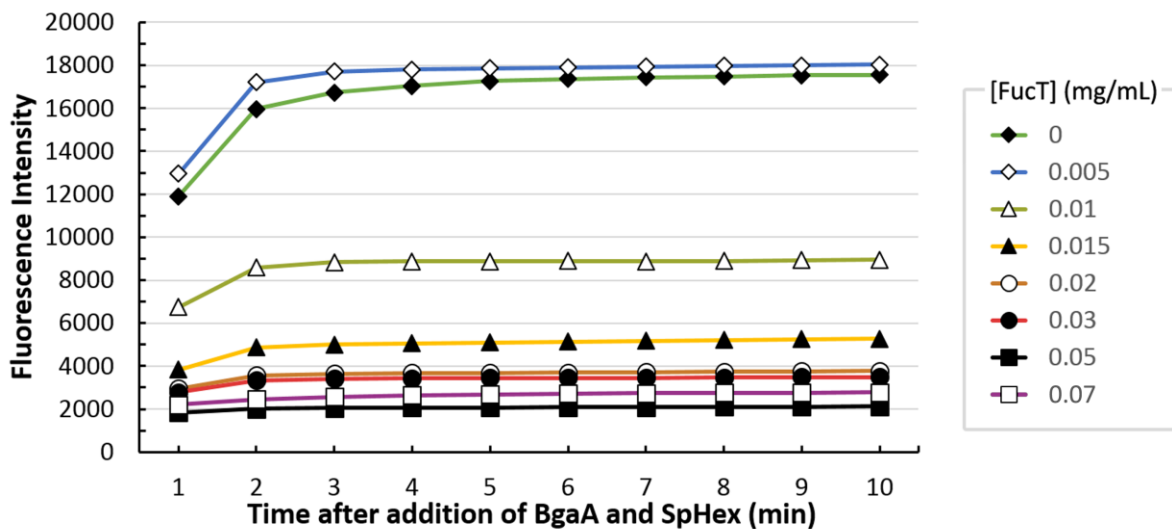


Figure 18) Determination of optimal FucT concentration and length of hydrolysis reaction

Experiments done in triplicate a 384-well plate showing fluorescence intensity (y-axis) plotted against time (x-axis) for different FucT concentrations (legend – right side). When MU- β -LacNAc was incubated in 50 mM Tris (pH 7.5) with MgCl₂, GDP-Fuc and different concentrations of FucT, the resulting fluorescent signal was inversely related to the concentration of FucT. Fluorescence was measured once per minute for 10 minutes, showing that the time to completion of the hydrolysis is around 5 minutes.

The precision of this test was examined by repeating the prior experiment with a single reading after 5 minutes, and only two FucT concentrations- 0.6 nM as a negative control (no hydrolysis; minimum fluorescent signal) and 0 nM as positive control (maximum hydrolysis; maximum fluorescent signal).(Figure 19) This assay yielded $Z' = 0.78$ (n=8), which is excellent for potential future high throughput applications.¹⁹³

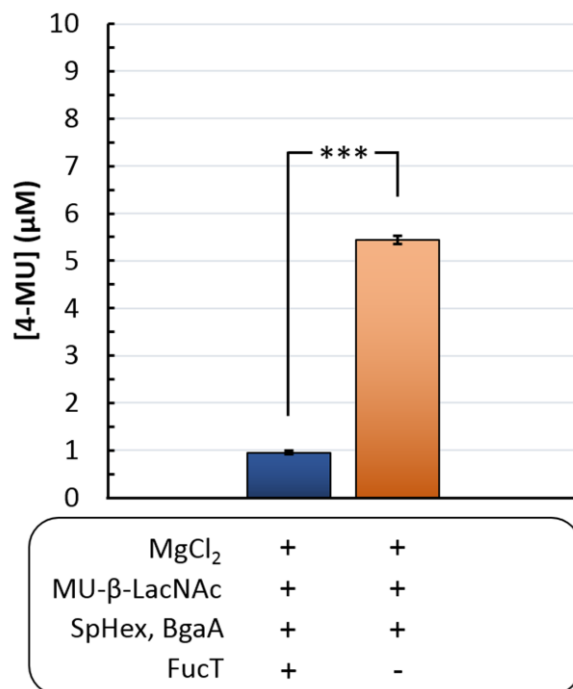


Figure 19) Fucosylation prevents hydrolysis and subsequent fluorescent signal

Fluorescence bar graph evaluating the MU-β-LacNAc-based assay's potential for throughput application by comparing the signal with and without FucT and measuring its precision.

*Fluorescence reading performed after 5 minutes of hydrolysis reaction with MU-β-LacNAc and prior 10 minute incubation with 0.6 nM FucT or buffer. Equivalent 4-MU concentration calculated by fluorescence standard. Experiments done in a 384-well plate. Error bars represent standard error. *** : $p < 0.01$. (n=8)*

A baseline fluorescence was observed up to around the signal of $\sim 1 \mu\text{M}$ 4-MU, possibly due to the incomplete quenching effect of MU-β-LacNAc on its 4-MU moiety. Though it has not been verified, it is possible that fucosylation further decreases the quenching effect, seeing as minimum fluorescence was higher in samples which included fucosylation compared to those

which did not. (Figures 17 and 19) In the future, this could be tested by measuring the fluorescence of MU- β -LacNAc over time while it is being fucosylated.

In low-throughput assay runs, the Z-factor (Z') value is a statistic that quantifies the response of an assay by comparing a set of positive and negative controls (Equation 7).¹⁹³ It is often used to determine whether or not an assay is suited for potential high-throughput application.

Equation 7) Estimated Z' Factor

$$Z' = 1 - \frac{3(\hat{\sigma}_+ + \hat{\sigma}_-)}{|\hat{\mu}_+ - \hat{\mu}_-|}$$

In this formula, σ_+ and σ_- are the sample standard deviations of the positive and negative controls, and μ_+ and μ_- are the sample means. If $Z' < 0$, then the positive and negative controls have too many similar readings for the assay to be useful. At $0 > Z' < 0.5$, then the assay is marginal. At $0.5 > Z' < 1.0$, the assay is excellent for high throughput. At $Z' = 1$, the assay is ideal for high throughput. To obtain this value for the MU- β -LacNAc assay, the *H. pylori* $\alpha(1,3)$ -fucosyltransferase—FucT— was used, for which GDP-fucose could act as the nucleotide sugar donor, with $MgCl_2$ to supplement the metal ion.¹⁹⁴ It was shown that this fucosylation assay presents potential for high throughput application ($Z'=0.78$ in 384 well-plate). GDP was used as an inhibitor for FucT in proof-of-concept and IC_{50} values were collected, setting the groundwork for future screens of potential inhibitors for FucT and potentially many other glycosyltransferases that can recognize MU- β -LacNAc as an acceptor substrate.

4.3. Inhibition by GDP: Proof-Of-Concept

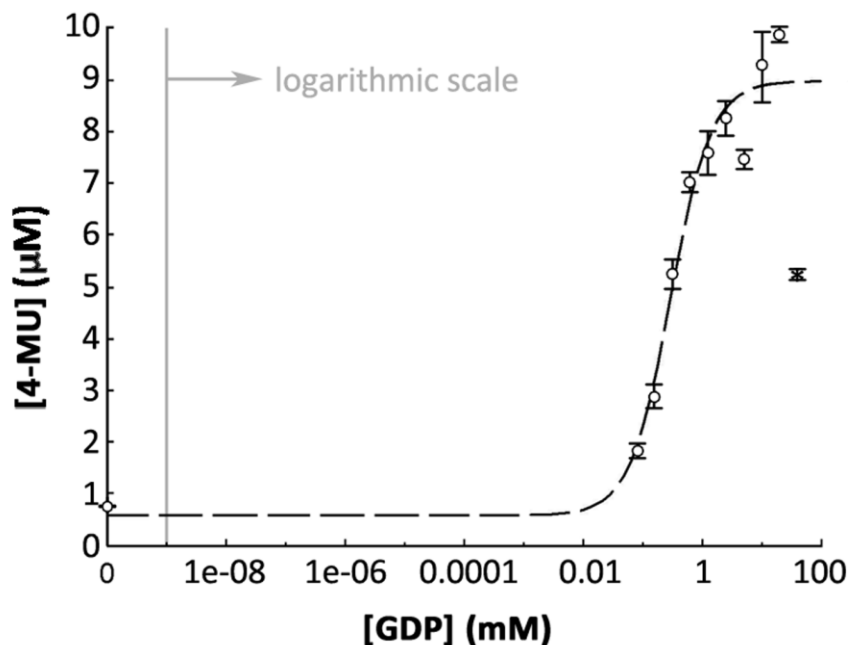


Figure 20) Proof-of-concept: Inhibition curves using GDP

*Proof-of-concept fluorescence-reported inhibition curve obtained for GDP inhibition of FucT using the MU- β -LacNAc-based assay. Experiments done in a 384-well plate. Error bars represent standard error. 0 mM GDP was plotted as 10^{-10} mM. *Excluding the last point (40 mM GDP) results in the dashed sigmoid curve. ($n=3$)*

Previously, the nucleoside diphosphate GDP had been shown to be a weak ($IC_{50} = 0.05$ mM) inhibitor for a recombinant human $\alpha(1,3)$ -fucosyltransferase via monitoring the fucosylation of di- and trisaccharides into tri- or tetrasaccharides.¹⁹⁵ As such, GDP was used as a proof-of-concept inhibitor for the fucosylation of MU- β -LacNAc by FucT. A blank and a range of 10 GDP concentrations ranging from 0.08 mM to 40 mM during the reaction step were at first given 5 minutes of incubation with FucT mix (0.6 nM FucT), then the reaction was started with

the addition of 'glycosylation' mix. 10 minutes later, 'hydrolysis' mix was added, 5 minutes after which fluorescence readings were taken, yielding GDP an $IC_{50} = 0.25 \pm 0.10$ mM. (Figure 20) It is worth noting that at the highest concentration of GDP (40 mM), fluorescence intensity had dropped by nearly half relative to the next highest concentration (a 20 mM GDP reaction). Excluding measurements taken at 40 mM GDP for the inhibition curve calculation would result in $IC_{50} = 0.29 \pm 0.07$ mM, lowering calculated uncertainty but heightening calculated IC_{50} . The bell shape of the inhibition curve was investigated after the inhibition assay had been otherwise optimized for DMF. All in all, these well-plate results were in accordance with GDP's weak profile as an inhibitor as well as the assay's model, in which the fucosylation of MU- β -LacNAc prevents its hydrolysis, and consequently, the fluorescent signal produced by the release of 4-MU is only observed when FucT has been inhibited.

Chapter 5. DMF Platform Validation

This chapter consists of the validation of the MU- β -LacNAc-based assay for DMF application, beginning with design considerations to improve droplet movement and dispensing, followed by the testing of surfactants toward the same ends, and then the validation of methods used to analyze data when performing the assay-on-chip. This concludes with the performance of the inhibition assay on DMF and the comparison of IC₅₀ results obtained with those obtained in a well plate.

5.1.Optimization of Fucosylation Inhibition Assay for Digital Microfluidics

A chip was designed (Figure 11) which brings several novel features, from electrode shapes to serial dilutions on 3 or more orders of magnitude, to the area of digital microfluidic designs for enzymatic assays, allowing a variety of droplet operations on the device using our automation system (Figures 7 and 15). In the work reported here, we used a two-plate configuration (as opposed to one-plate) to minimize droplet evaporation and permit droplet dispensing.

5.1.1. Optimization of dispensing to prevent biofouling

In initial experiments, droplet movement failure was experienced with assay reagents containing proteins such as FucT, BgaA or SpHex, who could not dispense from their reservoirs. We hypothesize that this is most likely due to protein biofouling^{179, 180}. Biofouling occurs when solutes adsorb to the chip surface, preventing any further droplet movement on the device. To minimize fouling at the dispensing step, five reservoirs were connected to additional inlet electrodes such that the solutions would rest on the reservoir for a minimal length of time. The ITO would be aligned with a third of the inlet electrode's surface and by applying a driving potential to this inlet, the solution is loaded into the gap between the ITO and DMF surface. (See Figure 11 for loading steps.) These droplets can then be used immediately for the assay without having rested on-chip before they became needed. Dispensing was also optimized through the sequential design/fabrication/testing of DMF chips with different dispensing neck and electrode dimensions.

5.1.2. Optimization of movement using oil and surfactants

Merely optimizing dispensing was insufficient to prevent biofouling from all assay reagents. Aside from resting time spent by a solution on-chip, factors affecting droplet movement in DMF were studied: (1) the composition of reagents- from the properties of their solutes to the overall pH.^{179, 180, 196} and (2) the shape and size of electrodes relative to droplet volumes.^{197, 198} Many labs have addressed the former via the addition of PEO-containing triblock copolymers or 'Pluronics' (BASF, Florham Park, NJ) to their solutions, some of which have been shown to increase the fouling threshold of protein concentrations for DMF by 1000-fold and to enable, for initially immovable cell culture media, from 100 to >300 steps of movement.^{179, 180} An alternative

solution is to surround the droplets in an oil shell to minimize fouling and evaporation of the droplets. To these ends, the gap between the ITO and chip is commonly immersed with Silicone oil.^{199,200} To determine the conditions in which the protein solutions used in the fucosylation assay would be capable of movement on the DMF device, an initial movement test was conducted with each of the proteins separately to discern which of them held the strongest biofouling capacity. BgaA was the least capable of movement. Speculatively, this could be due to its large size (~247 kDa, which is 4.5 times the mass of SpHex and FucT). Larger molecules do not flow past each other as easily and are more polarizeable; both of these factors increase viscosity.

As such, 0.05 mg/mL BgaA solutions were prepared with three different surfactant conditions: no surfactant, 0.05% Pluronic F-68, and 0.05% Pluronic F-68 while using pipette tips coated in silicone oil to dispense droplets (this process will simply be referred to as ‘with silicone oil’, although the resulting concentration is negligible). We also speculate that buffer conditions have an effect on droplet movement, and hence, we prepared solutions with three different buffer conditions: no buffer, 50 mM Tris, and 25 mM HEPES for a total of nine test solutions. Using the automation system, we manipulated the droplet between two target electrodes (crossing three electrodes in either direction to reach the other extremity) to implement the worst-case scenario until either movement failed 3 times consecutively or until movement had been successful 24 times (3 more times than the maximum number of movements expected across any electrode for this assay).

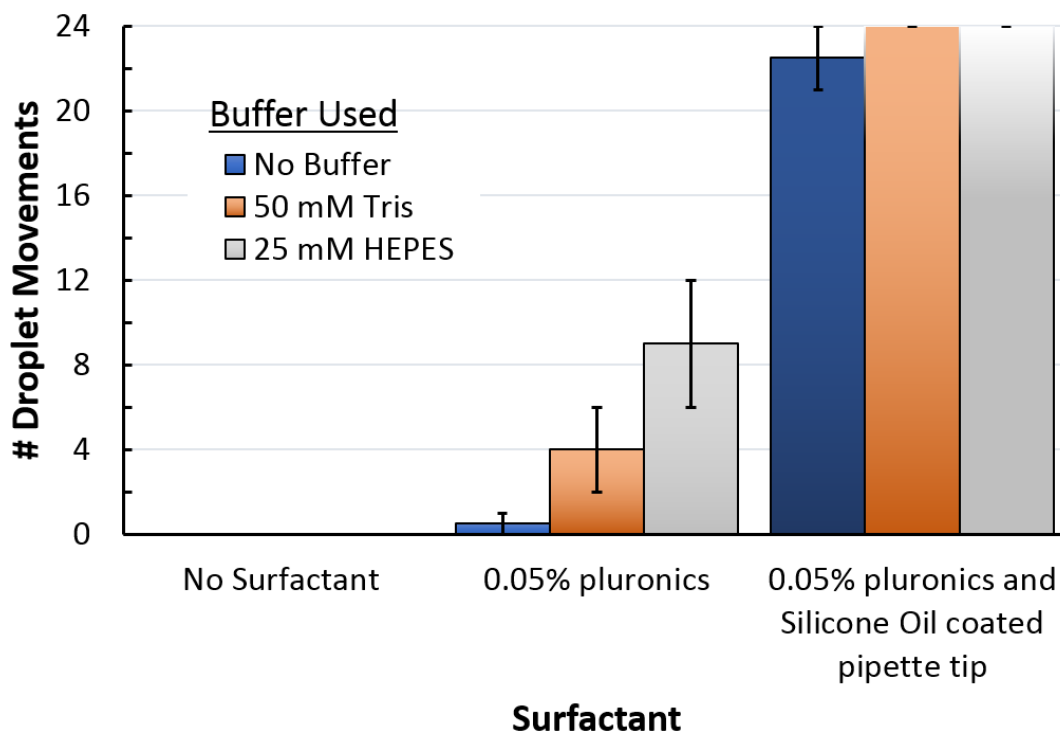


Figure 21) Movement of bulky protein solution using different buffers and surfactants

Bar graph evaluating the effect of different surfactant conditions and silicone oil on the number of movements from one extremity to the other for a span of 4 electrodes for 0.05 mg/mL BgaA protein solutions on a DMF device before the movements would fail consistently (3 times in a row). Error bars represent standard error. (n=2)

As shown in Figure 21, without the addition of surfactant, solutions were immobilized from the start. When 0.05% Pluronics F-68 was added to each of the three buffer conditions, droplet movement improved. Interestingly, without silicone oil, buffer composition also has an impact on droplet movement, in which fouling occurred after (on average) four movements for 50 mM Tris-HCl and eight movements for 25 mM HEPES buffer. We are unsure what is the cause, but we speculate higher ionic strength prevents the ‘salting-in’ biofouling of molecules.¹⁹⁶ The pH of buffers could also cause the degradation of the hydrophobic layer²⁰¹, though this would have been

unlikely to be the cause given that pH 7.5 Tris-HCl was less acidic than the pH 7.0 HEPES buffer. The possibility remains, seeing as the pH of HEPES buffer is less sensitive to temperature than Tris buffer, only changing by 0.17 from 25°C to 37°C whereas the pH of 50 mM Tris changes by 0.28. This could indicate greater suitability to DMF since the temperatures of electrodes can change upon actuation and could also be useful for future application when the assay is to be performed at biological temperature. The most notable improvement of droplet movement came with the application of both 0.05% Pluronic F-68 and silicone oil shells to BgaA solutions prepared with either buffer. Even though movement was stopped at 24 actuations, the droplets did not show any signs of slowing down. As a result of these tests, 0.05% F-68 with an oil shell and HEPES buffer were used to perform all subsequent runs of the fucosyltransferase inhibition assay.

5.1.3. Testing DMF surfactant and oil impact on 4-MU fluorescence

One of the major concerns in using an oil shell is the possible interactions it has with the aqueous droplet. Hence, we tested the impact of surfactants and silicone oil on 4-MU fluorescence by preparing standards using two different DMF surfactants at 0.05%. For each of these concentrations, an identical set was prepared with 5% silicone oil. With the two surfactants tested, Ethylenediamine tetrakis(ethoxylate-block-propoxylate) tetrol (Tetronics 150R1) and Pluronic F68, oil had no effect on 4-MU fluorescence ($p = 0.228$, $p = 0.143$, N.S. > 0.05) (Figure 22, right). Increasing Tetronics 150R1 concentration heightened 4-MU fluorescence, but Pluronic F68 had the same impact on 4-MU fluorescence for each of the five concentrations tested (Figure 22, left). Seeing as oil and F68 concentration did not present a source of error for fluorescence readings and given the superior performance of droplet movement with this surfactant, Pluronic F68 with an oil shell was chosen as the ideal candidate for performing the inhibition assay on a DMF device.

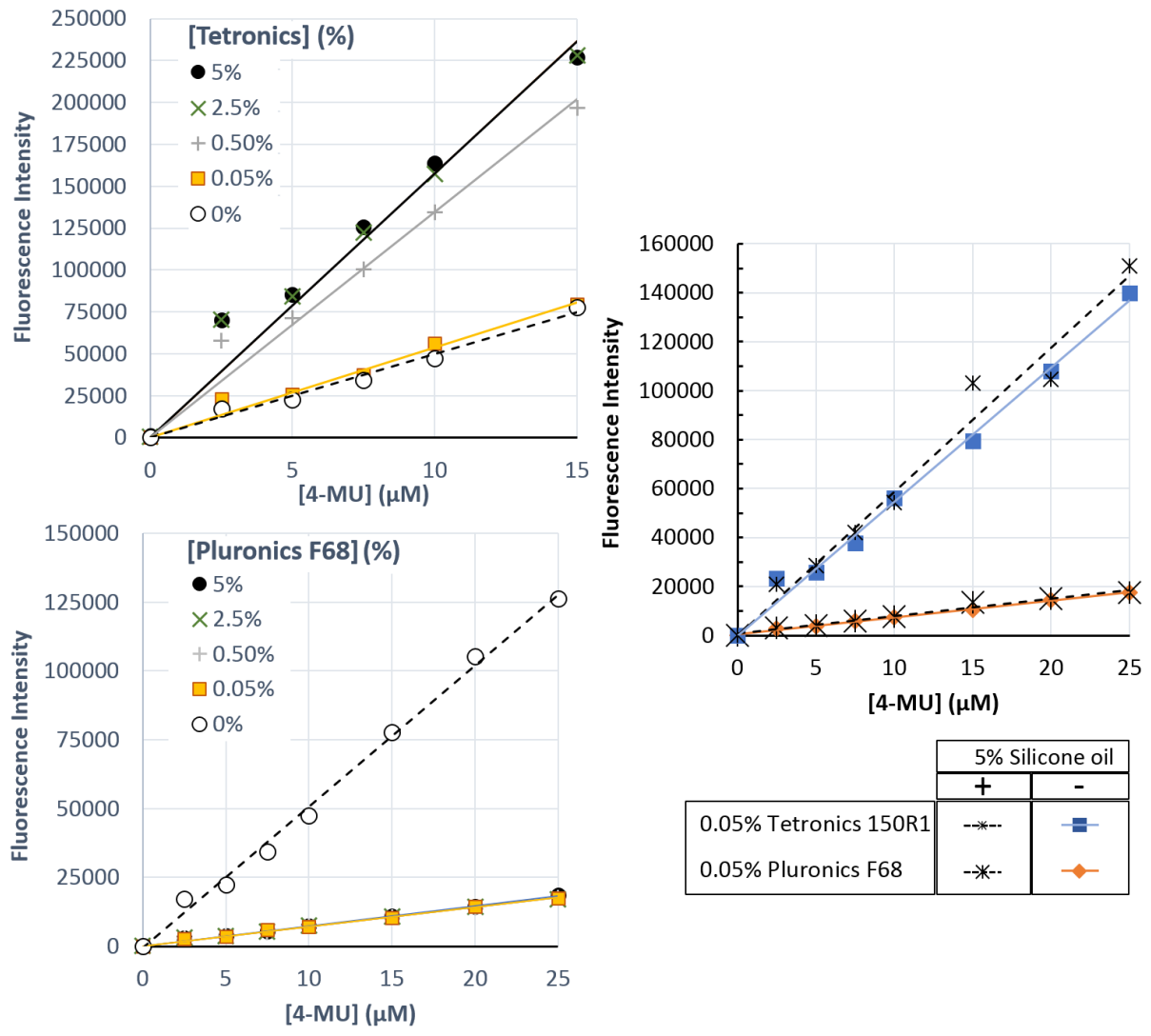


Figure 22) 4-MU Fluorescence with different surfactant concentrations

Standards prepared in a 384 well plate with different concentrations of Tetronics 150R1 and Pluronic F68 (left) and at DMF concentrations (0.05%), with or without 5% silicone oil (right).

(n=1)

5.1.4. Optimizing electrode shape for droplet movement

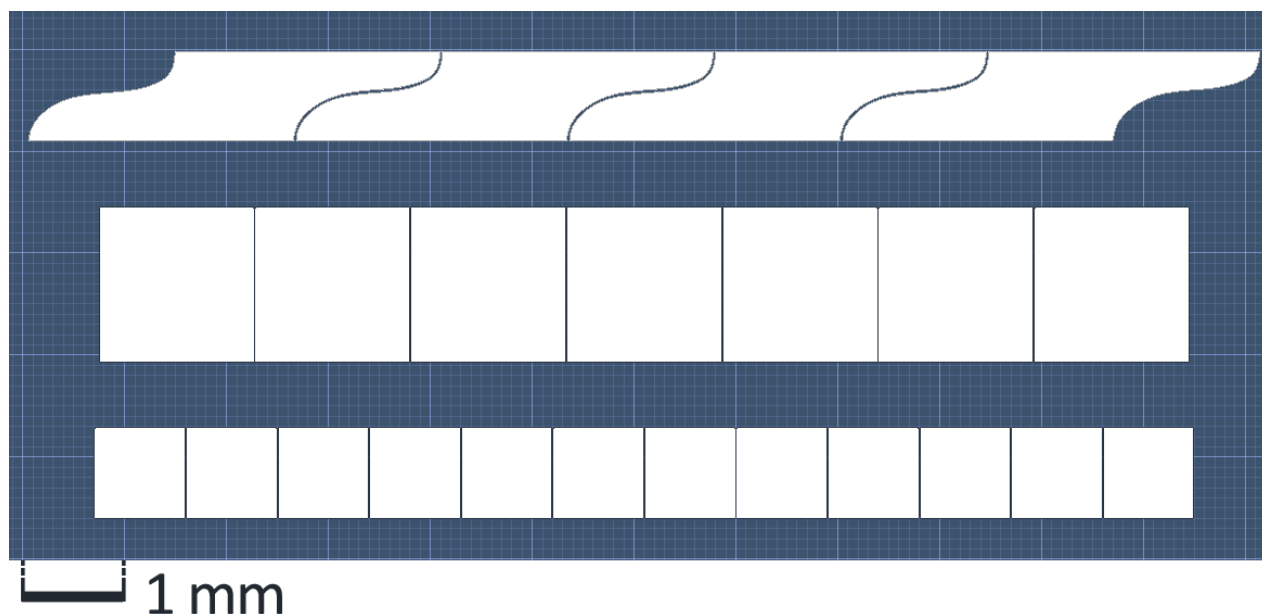


Figure 23) Skewed-wave electrodes compared to square electrodes

View of shapes prepared in AutoCAD with a 1 mm scale for comparison. The first row shows four skewed-wave electrodes, the second row shows 7 square electrodes of equal area to skewed-wave electrodes, and the third row shows 12 square electrodes of equal height to the skewed-wave electrodes. All electrodes have 30 μm gaps between them.

With the composition of assay solutions optimized for movement, another factor concerning droplet mobility was to be examined. Movement on a DMF device depends on the electric field between the top and bottom plates,¹⁶⁵ which is affected by the shape of actuated electrodes. Typical electrode shapes are square or rectangular given the simplicity of drawing these shapes and the ease of their fabrication; however, droplets are known to become stranded, or ‘static’ on an electrode when these volumes fail to overlap with adjacent electrodes, ceasing all movement.²⁰² In response, some groups have designed interdigitated (ex.: “comb” or “zig-zagged”

edges) or otherwise original electrode shapes (ex.: alternating triangles).^{197, 203} Although this allows droplet movement for smaller volumes than simple rectangular electrodes, pointed shapes create regions with high electric fields $> 10^8$ V/cm which can cause dielectric breakdown.^{197, 203} To alleviate this problem, intercalating electrodes were created with sinusoidal curves and minimum angles of $\sim 90^\circ$ where its edges join together, referred to as “skewed-wave” shaped. (Figure 23, top). Their dimensions (4.0 mm x 0.87 mm) were chosen so that upon actuation, the smallest resting droplet (~ 480 nL) would shrink vertically and stretch horizontally to reach adjacent electrodes in either direction. The length of these electrodes presented a second advantage: droplets could bridge long distances across the chip with a fewer number of electrodes and actuations. If square electrodes of the same area as a skewed-wave (1.5 mm x 1.5 mm) were used for the linear track, it would require up to 8 to bridge the length of 4 skewed-waves (thus increasing total electrode area by 75-100%), but the minimum volume of droplets would need to increase by $\sim 27\%$ to avoid becoming static. (Figure 23, middle) Square electrodes of the same height could be used to span the distance of 4 skewed-wave electrodes without increasing area or minimum volumes, but in this case, up to 13 electrodes would be required. (Figure 23, bottom) This is the first time that such an electrode shape is presented, and it can be used for experiments requiring reliable droplet movement with limited space on the substrate or pins/switches in the automation system.

5.1.5. Optimization of dispensing by actuation sequence

Initially, droplets were dispensed with a two-step process in which a liquid finger is pulled out from the reservoir by adjacent electrodes until the volume reaches a destination electrode, part of it still resting on the reservoir. Voltage was then applied to both the reservoir and the destination electrode to create a break in the liquid finger, splitting it into two volumes, the bulk of which

remained in the reservoir. Generally, droplets were successful in dispensing so long as the volume initially in the reservoir did not exceed 3.3 μL , at which point too much of the volume remained in the reservoir and on the neck to cause its separation at the splitting step, or drop below 2 μL , at which point the liquid finger was no longer in contact with the reservoir on the crucial splitting step. Reservoir volume generally dipped below the lower threshold after 2 or 3 dispensed droplets. However, this dispensing limit was circumvented by replacing the two-step dispensing process with a 'Low-volume dispensing' sequence that would gradually separate the volume from its droplet by continuously actuating the destination electrode while also actuating the electrodes leading back to the reservoir, inching back toward it two electrodes at a time until splitting occurred. (Figure 10.) This actuation sequence ensured that we were capable of dispensing 3-4 additional droplets until the entire volume of the reservoir had been consumed.

5.1.6. 'Pixel Count': Image analysis to obtain droplet volume from area occupied

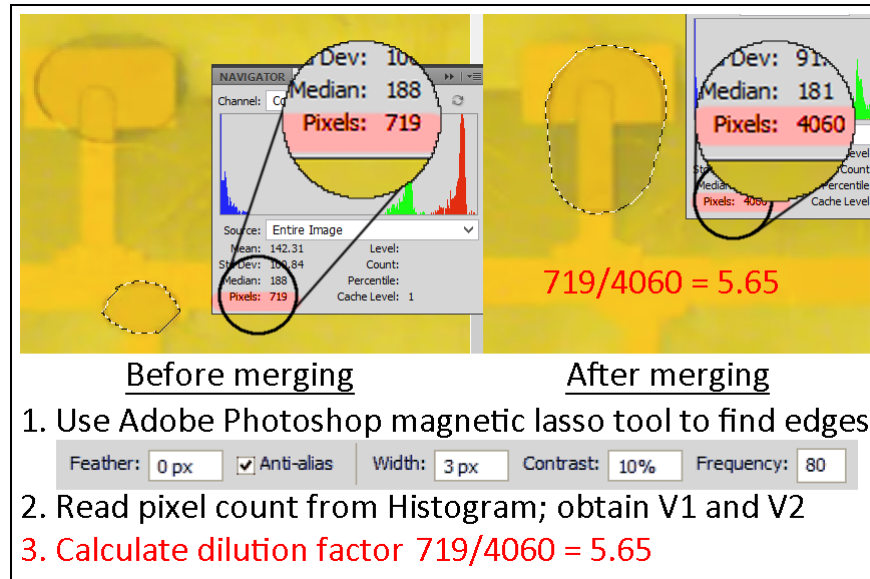


Figure 24) Pixel count being used to calculate a dilution factor

Magnetic lasso tool was used in Adobe Photoshop CS5 and Creative Suite with anti-aliasing (takes into account the blurriness of edges while counting pixels), 3 px width (influences sensitivity), 10% contrast (influences sensitivity), and 80 frequency (how often it searches for the next point while tracing the edge).

Given all of the factors that could impact droplet size (See 1.3.4) and hence the validity of our analyses of the data obtained downstream, and one of the benefits of digital microfluidics- its amenability to automation, we worked towards the goal of creating an automated analysis tool that can directly calculate the concentrations in our samples instead of using inline detectors or external plate readers. We have created an image analysis method, referred to here as Pixel Count (PC) which measures the volumes on the device and uses a standard dilution equation ($C_1V_1=C_2V_2$) to

calculate the final concentration of the sample. (Figure 24) The workflow of this consists of recording images of the device and porting these to Adobe Photoshop where an edge-finding algorithm was used to determine droplet areas from which volume can be extrapolated (similar to work by Vo et al.¹⁴⁵). In the future, Pixel Count should be used with open source edge-finding algorithms integrated into DMF programs which could record and respond to these concentrations from automated image analyses.

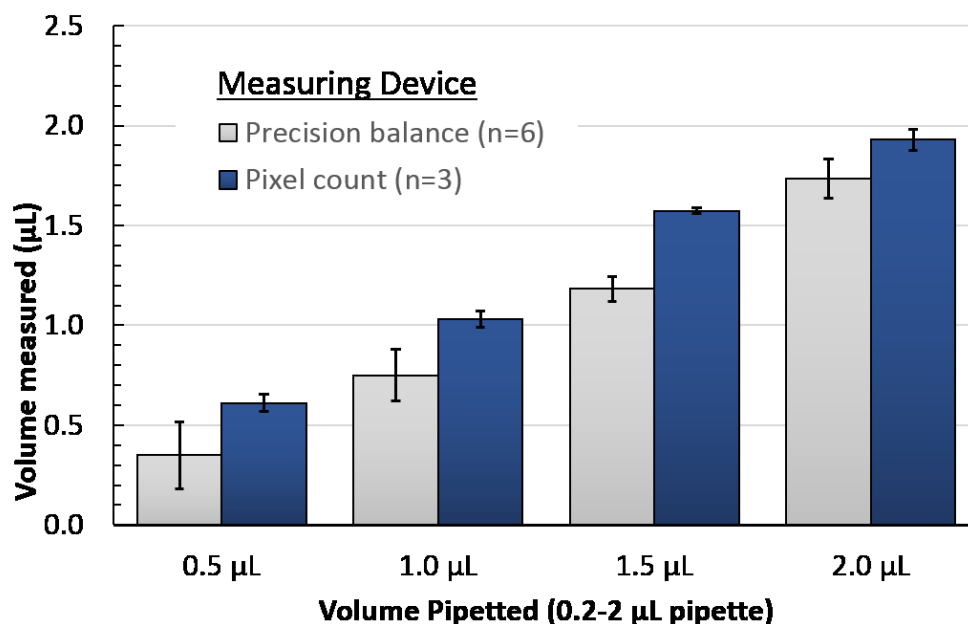


Figure 25) Accuracy and Precision of Pixel Count as a method of volume measurement

Bar graph plotting volumes measured by either precision balance or pixel count (y axis) grouped by the volumes pipetted by micropipette (x axis). Error bars represent standard error. Different small volumes (0.5, 1, 1.5 and 2 µL represented on the x axis) were pipetted onto a DMF device from a 0.2-2 µL micropipette and volume measured by weight using a precision balance (n=6) and by area to volume translation using pixel count (n=3).

Using PC, initial volume (before dilution) and final volume (after dilution) could be determined. To validate PC, we first tested it against the volumes given by micropipette and by precision balance. (Figure 25) A range of volumes (0.5-2 μL) were pipetted onto the device mounted on a precision balance, for which a change of weight reported volume. The same range of volumes was pipetted onto a device which was rapidly covered by an ITO then measured by PC. As shown in Figure 25, the volumes calculated by PC are a closer match to those given by the micropipette and are exhibit more precision than those reported by the precision balance.

To calculate droplet volume by pixel count, the known dimensions of an element of the chip image could be used to obtain the equivalent area of the droplet in mm^2 , which can then be multiplied by the measured gap height of the chip to result in a mm^3 measurement of the droplet. (Table 2 and 3) The volume of these aqueous solutions is obtained given that 1 mm^3 of volume should approximate 1 μL . (Equation 8)

Equation 8) Calculation of droplet volume by pixel count

$$V_{droplet} = droplet_{pixels} \times \frac{known_{mm^2}}{known_{pixels}} \times gap_{mm}$$

Where $V_{droplet}$ is the volume of the droplet in μL , $droplet_{pixels}$ is the area of the droplet measured in pixels, $known_{mm^2}$ is the known area of a measurable feature in the chip image in mm^2 , $known_{pixels}$ is that same feature's area measured in pixels, and gap_{mm} is the height of the gap between the bottom and top plate of the DMF device in mm.

Table 2) Calculating the mm² per pixel factor using the known size of a visual element of the chip design

Area of reservoir	mm ²	pixels	mm ² per pixel
Pixel count 1	12.41	7920	0.0016
Pixel count 2	12.41	7986	0.0016
Pixel count 3	12.41	8107	0.0015
Average	12.41	8004.33	0.0016

Table 3) Pixel count-determined volumes for different volume settings on a 0.2-2 μ L micropipette

Volume set on micropipette (μ L)	Droplet area (pixels)	Droplet area (mm ²)*	Volume (1 mm ³ = 1 μ L)**	Average volume	Standard error (%)
2.0	5669	8.79	1.85	1.93	2.282582
	6128	9.50	1.99		
	5980	9.27	1.95		
1,5	4720	7.32	1.54	1.57	2.547805
	5079	7.87	1.65		
	4700	7.29	1.53		
1.0	3240	5.02	1.05	1.03	1.305528
	3097	4.80	1.01		
	3162	4.90	1.03		
0.5	1922	2.98	0.63	0.61	8.472708
	2126	3.30	0.69		
	1581	2.45	0.51		

For each initial solution, the initial concentration was known- and with pixel count, initial volume and final volume were also known. As such, the final concentrations could be calculated as long as mixing was homogenous, which was the next factor to be tested.

5.1.7. Testing homogeneity of solutions mixed on DMF device

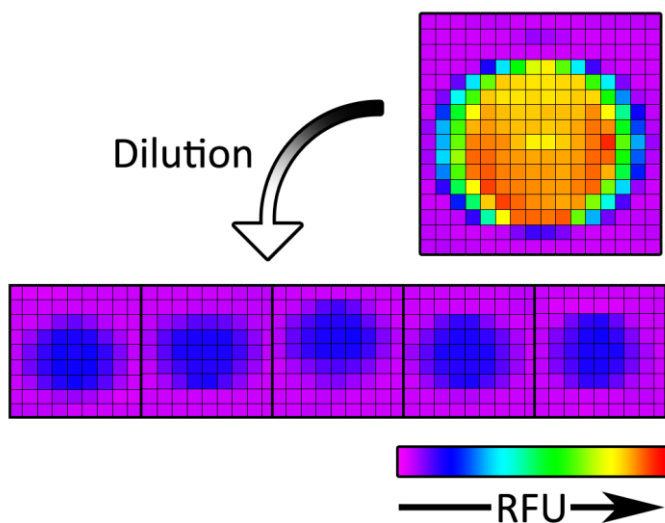


Figure 26) Testing the homogeneity of the fluorescence of dispensed droplets from a volume mixed on-device

Droplet of 50 μM 4-MU solution (top), from which one droplet was dispensed and mixed with a droplet of buffer. 5 droplets were then dispensed from this dilution (middle) and scanned, then visualized with a fluorescence heat-map.

The homogeneity of mixing solutions on device was tested by dispensing a droplet of 4-MU at high and low concentrations into 2.7 μL buffer. These volumes were then mixed and from each, 5 droplets were dispensed. The fluorescence of these resulting droplets was measured, showing a high degree of homogeneity among the concentrations of droplets dispensed from a mixed volume (<3%). (Figure 26, 27)

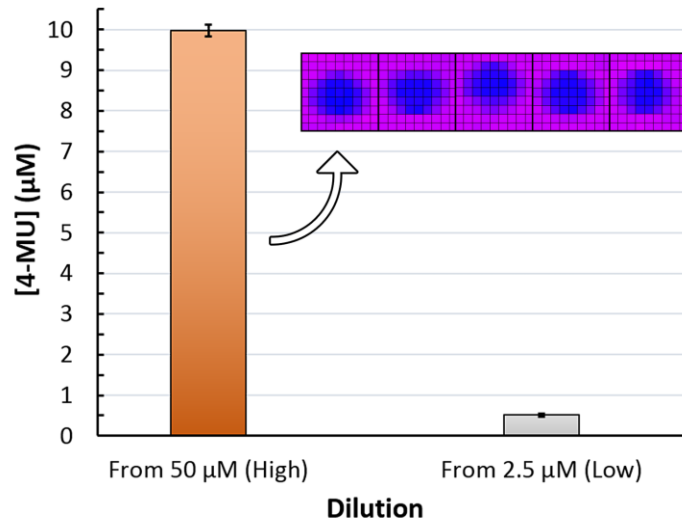


Figure 27) Dispensed droplets fluoresce homogeneously from a volume mixed on-device

Fluorescence bar graph comparing the fluorescence of droplets diluted from different initial 4-MU concentrations to determine homogeneity of mixing. Corresponding 4-MU was calculated by fluorescence standard obtained on device. Droplets were dispensed from $[4\text{-MU}]_{\text{ini}} = 50 \text{ mM}$ (High), 2.5 mM (Low; Left) ($n=5$)

5.1.8. Testing calculation of 4-MU concentration: Pixel Count validation

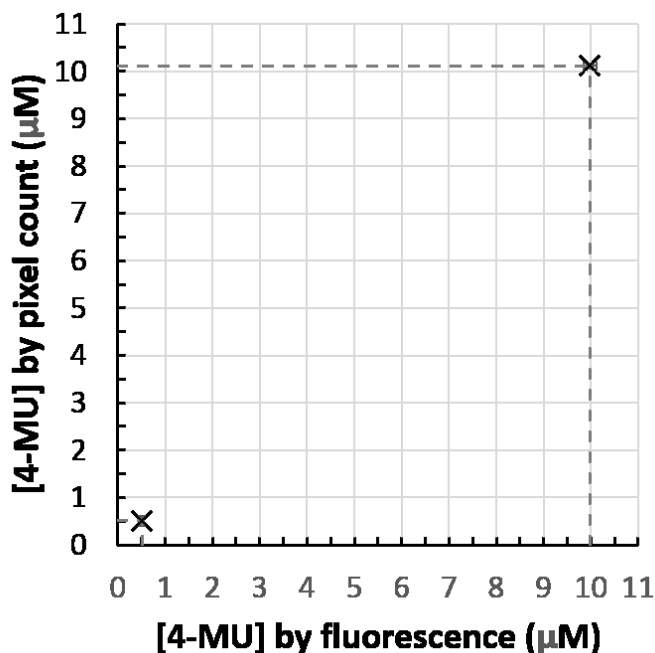


Figure 28) Concentration of diluted 4-MU droplets calculated by fluorescence VS. pixel count.

Comparing, with diluted droplets from high and low initial 4-MU concentrations in 25 mM HEPES buffer, the concentration of 4-MU calculated by fluorescence standard VS. that which is calculated by pixel count. [4-MU] calculated by fluorescence were done through 4-MU standards on device. [4-MU] calculated by pixel count were done by dividing the initial calculated [4-MU] (by fluorescence) by the dilution factor calculated by pixel count. (n=5)

Finally, we quantitatively verified PC-based calculation of concentrations. Both the parent solution droplets and each of their 5 diluted progeny droplets had their 4-MU concentrations calculated using a standard linear regression from 4-MU standards pipetted and measured on-device. From the same initial concentration of 4-MU, PC was used calculate the

concentrations of the diluted droplets. Both fluorescence-based and PC-based methods showed excellent agreement in their values (Figure 28). Hence, the PC method for calculating concentrations seems to be analogous to the well plate reader as long as C_1 is known, without requiring a fluorometric solute, and with the additional benefit of camera image-analysis based automation potential.

5.2. Inhibition Assay on DMF Device

5.2.1. Serial dilutions on chip

Inhibition assays generally span at least 3 degrees of magnitude. However, serial dilutions insofar have been limited on DMF devices. Sequential 2-fold dilution factors, wherein a droplet of buffer and of solution are mixed together then split apart into two equal volumes, have been used to generate up to 8-fold dilutions at which point errors in dilution factor reached ~25% in only three dilution steps.^{181, 204, 205} Most of this error can be accounted for by variations in dispensed and split volumes.¹⁸¹ To span a 1000-fold dilution factor, 10 such 2-fold dilution steps would have been needed. To avoid the considerable compounding error this would entail, a different dilution strategy was necessary. Five reservoirs were primed with 2.7 μL buffer. A ~ 0.5 μL droplet of GDP solution serving as inhibitor for proof-of-concept was dispensed and mixed with the contents of the first reservoir. (Figure 11.) A droplet was then dispensed from this reservoir and mixed with the buffer in the second reservoir, and so on until 5 cycles of approximately 5-fold serial dilution had been achieved. Given the initial GDP stock and negative control (only buffer), by the end of these steps, there were 7 samples spanning a dilution factor surpassing 5000-fold on-device, for which each concentration could be calculated using the pixel count method with an estimated $\pm 2.4\%$ standard error for each dilution step accounted for by the pixel count method (obtained by measuring different reservoirs of known equal area across the same snapshots of a chip ($n=15$) and compounding the average $\pm 1.7\%$ standard error of the measurements for initial and final volumes). As such, the error of pixel-count calculated GDP concentration should span from $\pm 2.4\%$ at the first dilution up to a compounded $\pm 12\%$ after 5 steps of serial dilution (>5000 -fold), which is a marked improvement over $\pm 25\%$ at the 8-fold dilution mark. After two droplets were dispensed from each

dilution of GDP and the remaining waste volumes removed, the inhibition assay could take place (Figure 11.) Despite using pixel count to lessen the compounding error in serial dilution steps for the inhibitor concentration, other sources of error for the IC₅₀ value reported on DMF device remain present. Notably, the variation in the reaction concentrations of the assay components can be expected to be slightly different between every sample due to the variability in dispensed volumes. While pixel count could technically report the concentrations for other important assay components (the glycan MU-β-LacNAc, the sugar-donor GDP-fucose, the fucosyltransferase FucT...) this information could not be used to reduce the error that this variation in other concentrations has introduced to the fucosyltransferase inhibition assay.

5.2.2. Inhibition of a fucosyltransferase on chip

To evaluate the potential for testing inhibitors for fucosylation assays on digital microfluidic devices, we created a microfluidic system that generates a serial dilution of the inhibitor, spanning at least four orders of magnitude. After optimizing conditions for this assay to be held on a digital microfluidic device, GDP was tested as a proof-of-concept inhibitor for FucT. Figure 20 shows the evaluation of the dose-responsive inhibitory activity of GDP, reported by fluorescence, together with well plate results for comparison.

On the DMF device, in addition to the blank (0 mM GDP), six GDP concentrations were generated via a series of ~5.5-fold dilutions, for which each concentration was calculated using our PC method. The assay was then performed on-device with 0.03 mg/mL FucT. (Figure 11, Online video: <https://www.youtube.com/watch?v=Ehot1basdzM>) Compiling the results from three runs of the assay, the IC₅₀ value initially obtained for GDP inhibition of FucT was 0.180

mM \pm 0.199. Similarly, we implemented the same assay in a well plate and achieved an IC₅₀ value of 0.108 mM \pm 0.205 (Figures 29a, 29c).

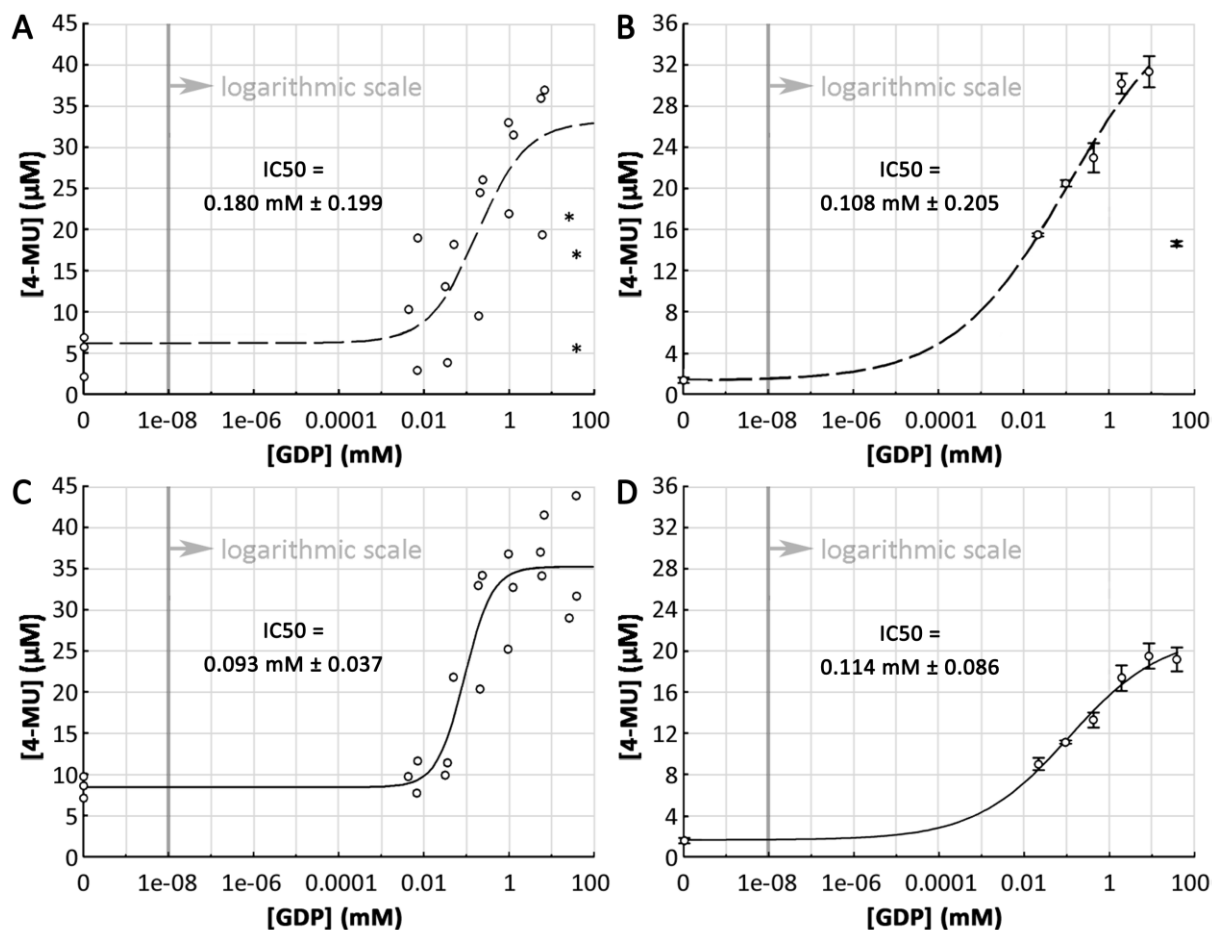


Figure 29) Inhibition curves using GDP

FucT inhibition assays with GDP done in a 384-well plate (A, C) or on DMF device (B, D) before (A, B) and after (C, D) glycine dilution. Error bars represent standard error. IC_{50} s were drawn and fitted to the formula $y=b+\frac{(a-b)}{1+(x/c)^d}$ using a least squares routine by GNUPLOT-powered software available online at: (<http://www.ic50.tk>). Sigmoid curves and corresponding 0 mM GDP was plotted as 10^{-10} mM. Before glycine dilution, 40 mM GDP points were marked with an asterisk (*) and excluded as outliers. (n=3)

However, as previously seen at the proof-of-concept stage, the fluorescence intensity recorded for samples at the highest GDP concentration (~40 mM) was dramatically lowered.

Typically, this reversal of response to inhibitor concentration following what appears to be peak inhibition is attributed to bell-shaped dose-response curves, in which multiple binding sites, multiple targets, or the aggregation of drug into colloids at certain concentrations negatively impacts inhibition after inhibitor concentration crosses above a certain threshold.²⁰⁶⁻²⁰⁸ Given that 4-MU is prone to shifts in its emissions peak in response to differences in ionic conditions, pH, and % water content,²⁰⁹ it was hypothesized that the bell-shaped dose-response curve was not due to differences in inhibition, but rather, that it could be due to an as-of-yet unidentified quenching effect of our concentrated neutral-pH GDP solution upon 4-MU. (For structurally related compounds to 4-MU, halide ions, aromatic amines, acetone and flavonoids have all been reported as quenchers.²¹⁰) To test our speculation, we equilibrated assay solutions by subjecting them to a 5-fold dilution in pH 10.4 1M glycine. As shown in Figure 29, this immediately restored the curve to a sigmoidal fit when performed, both on the well plate ($R^2 = 0.718$, $p > 0.05$; N.S. to $R^2 = 0.989$, $p < 0.01$; **) and on the DMF device ($R^2 = 0.492$, $p < 0.05$; * to $R^2 = 0.85$, $p < 0.01$; **).

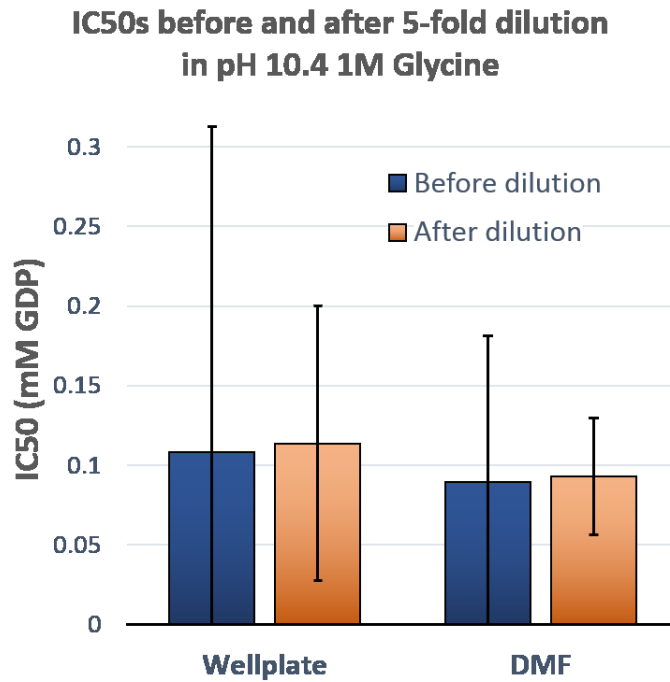


Figure 30) IC₅₀ comparison before and after glycine dilution on both well plate and DMF device

Bar graph comparing the IC₅₀ reported by DMF device and that reported by the same assay solutions (with oil and surfactant) in a 384-well plate. Data points taken at 40 mM GDP were excluded in the IC₅₀ calculation prior to glycine dilution on well plate only. (n=3)

Due to the heightened fluorescence it displayed at an elevated pH, it was not necessary to adjust gain and settings on the well-plate reader: similar standard linear regressions were obtained for 4-MU with these settings both prior and after the glycine step on both well-plate and DMF device (Figure 31). The values reported by the inhibition assay after glycine dilution were relatively consistent with each other at 0.114 mM ± 0.086 on well plates and 0.093 mM ± 0.037 on DMF devices. (p=0.53; N.S. at α = 0.05)

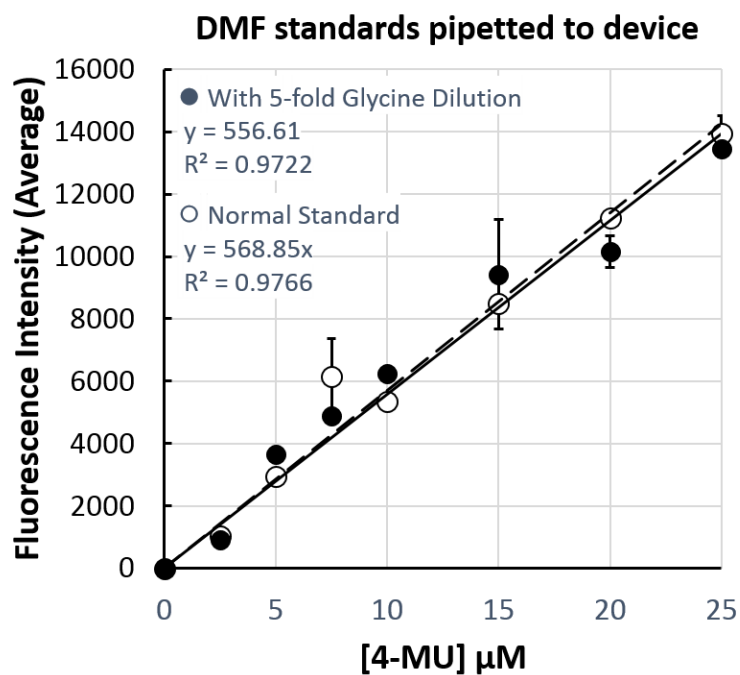


Figure 31) 4-MU standards subjected to 5-fold dilution in pH 10.4 1M Glycine

Standard linear regressions of 4-MU fluorescence on a DMF device before and after a 5-fold dilution in pH 10.4 1M glycine. Error bars represent standard error. All standards prepared with 0.05% pluronics and pipette tips coated with silicone oil.

Even prior to glycine dilution, reaction solutions in DMF conditions further altered the fluorescence intensity observed to report equivalent 4-MU concentrations which were much higher than the theoretical maximum given by the 10 μM MU- β -LacNAc present in solution, despite that the 4-MU standards had been prepared with the same buffer and surfactant conditions. While heightened fluorescence could in part be explained by the reflectivity of metallized electrode surfaces in DMF, the well plate results demonstrate highly similar behavior, indicating that some property of the reaction components other than buffer and surfactant alone might enhance 4-MU fluorescence. Due to the nature of concentration dose-response curves, this discrepancy between

the fluorescence intensity reported by 4-MU standards in contrast with the product of hydrolyzed MU- β -LacNAc in reaction conditions had no impact on their ability to report IC₅₀ values.

Additionally, the early proof-of-concept inhibition curve obtained in non-DMF optimized conditions (no surfactant, oil, or HEPES buffer) had neared its lowest inhibition state with only a 500-fold dilution, whereas dilutions of GDP tested in DMF conditions in the well plate were of 7 concentrations spanning from 1 to 1845-fold and still hadn't attained their lower plateau. This would suggest heightened inhibitory effect on FucT (higher fluorescence) even at lower concentrations of GDP, possibly due to the inhibitory effect oil surfactants can have on enzymes.²¹¹

Chapter 6. Concluding Remarks

In conclusion, the labelled synthetic disaccharide MU- β -LacNAc has shown itself to be a reliable target substrate and a useful probe for fucosylation and fucosylation inhibition by FucT, with potential for high throughput application ($Z' = 0.78$ in 384 well plate,) although such an application is not found in this work. Though the DMF system used is outperformed by robotics when it comes to multiplexing, it has served to develop methods^{145, 148} and other types of enzymatic assays on digital microfluidics devices²¹² at an affordable fraction of the cost associated to robotic fluid-handling systems, while economizing on substrate-consumption costs. In this work, DMF permitted the same reactions to be held at an 87.5% reduction of the minimal volume used in a 384-well plate. It was used to generate serial dilutions of GDP for the inhibition of *H. pylori* α -1,3-fucosyltransferase, FucT, using MU- β -LacNAc as a target substrate. Dose-response curves were obtained. We also show results related to optimizing the device conditions for performing the assay, such as electrode design and the testing of droplet dispensing and movement with surfactants and an oil shell. Serial dilutions spanning 4 degrees of magnitude were carried out on a DMF device for the first time, with inhibitor concentrations calculated through image analysis so as to circumvent part of the error typically associated to serial dilutions on this platform. Comparable performance was shown between 384-well plate and DMF device, with similar IC_{50} values for GDP ($0.114 \text{ mM} \pm 0.086$ and $0.093 \text{ mM} \pm 0.037$, respectively).

We report the alteration of a bell-shaped inhibition curve for GDP into a sigmoidal shape when assay samples are subjected to a 5-fold glycine dilution on well-plate and on DMF device, demonstrating that the dip in fluorescence at high GDP concentration was not due to a change in

the reaction, but rather, to a change in the fluorescence of 4-MU. In future work, we hope to discern the assay component(s) responsible for enhanced 4-MU fluorescence in assay conditions; for now, we know that DMF surfactants and HEPES buffer are not solely responsible.

We also report a skewed-wave electrode design allowing droplets in a large range of sizes to move quickly across longer spans per electrode used. Additionally, a GUI was built as a controller for a Python 2.7-based framework. PaseMaker (Path Sequence Maker), a Python 2.7-based universal path-solver, was created to generate electrode actuation sequences for dispensing, mixing, moving, splitting, low-volume dispensing, and circular mixing on any digital microfluidics chip design. It has been made available as an open-source software. Its true potential lies in its integration with DMF control programs which include a visual representation of one's electrode layout, allowing it to generate the actuation sequence after a user visually designates electrodes. One such DMF control program, Nelumbo, which integrates PaseMaker is already in the works by Philippe Vo. Due to its ease of integration with other softwares and universal applicability to DMF designs, I envision that PaseMaker could some day help in speeding up the pace of DMF work in many labs. In future work done on this program, perhaps it could be developed into a python module or have a visual electrode layout builder incorporated in its GUI. PaseMaker has also been structured in a manner that it should be possible to instruct it to route droplets through alternate paths when necessary to avoid fouled electrodes, or to automatically solve the path through the least used electrodes, but this functionality has not yet been implemented.

The ease of integration of DMF automation with computer electronic hardware and software components, combined with the individual manipulation of on-device volumes, grants it unparalleled versatility when it comes to computerizing and automating laboratory protocols- in

the future, image-processing algorithms using the pixel count concept tested in this work could be used for DMF operation to automatically respond to visually cued variables to reduce experimental error by maintaining reservoir volumes in specific ranges for dispensing reproducible droplet volumes, precisely calculating concentrations generated on-chip instead of relying on estimates, and using alternate dispensing options (such as the low-volume dispensing sequence described in this work).

Finally, toward the continued facilitation of drug discovery for inhibitors of fucosyltransferases, as well as the development of diagnostic and research tools for glycome-modifying diseases, future work could continue to expand the repertoire of tools available to test for glycosylation and its inhibition. For example, MU- β -LacNAc could also be used as an acceptor substrate in other glycosylation assays. One could also synthesize the sialylated form of MU- β -LacNAc, a methylumbelliferated Sialyl-LacNAc, to assay for the inhibition of Sialyl-LewisX formation. Like the LewisX formed by the fucosylation of MU- β -LacNAc, screening for inhibitors of glycosyltransferases involved in Sialyl-LewisX formation could lead to the discovery of drugs to combat metastasis, drug-resistance and proliferation in cancers, host colonization by pathogens, chronic inflammation, and even autoimmune diseases such as asthma.^{28, 64, 66, 82, 213}

References

1. Varki, A.J.D.E.K.J.C. Essentials of Glycobiology. Ch3: Cellular organization of glycosylation, Edn. 2. (Cold Spring Harbor Laboratory Press, NY; 2009).
2. Weerapana, E. & Imperiali, B. Asparagine-linked protein glycosylation: from eukaryotic to prokaryotic systems. *Glycobiology* **16**, 91R-101R (2006).
3. Messner, P. Prokaryotic glycoproteins: unexplored but important. *J Bacteriol* **186**, 2517-2519 (2004).
4. Apweiler, R., Hermjakob, H. & Sharon, N. On the frequency of protein glycosylation, as deduced from analysis of the SWISS-PROT database. *Biochim Biophys Acta* **1473**, 4-8 (1999).
5. Houry, G.A., Baliban, R.C. & Floudas, C.A. Proteome-wide post-translational modification statistics: frequency analysis and curation of the swiss-prot database. *Sci Rep* **1** (2011).
6. Macedo, C.S., Schwarz, R.T., Todeschini, A.R., Previato, J.O. & Mendonca-Previato, L. Overlooked post-translational modifications of proteins in *Plasmodium falciparum*: N- and O-glycosylation -- a review. *Mem Inst Oswaldo Cruz* **105**, 949-956 (2010).
7. 'Committee on Assessing the Importance and Impact of Glycomics and Glycosciences, B.o., Chemical Sciences and Technology, B.o.L.S., Division on Earth and Life Studies, National & Council', R. in Transforming Glycoscience: A Roadmap for the Future. (eds. T. National & A. Press) (Washington (DC); 2012).
8. Bourne, Y. & Henrissat, B. Glycoside hydrolases and glycosyltransferases: families and functional modules. *Curr Opin Struct Biol* **11**, 593-600 (2001).
9. Varki, A.L., John B. Essentials of Glycobiology. Ch6: Biological Roles of Glycans, Edn. 2. (Cold Spring Harbor Laboratory Press, NY; 2009).
10. Perez, S., Sarkar, A., Rivet, A., Breton, C. & Imberty, A. Glyco3D: a portal for structural glycosciences. *Methods Mol Biol* **1273**, 241-258 (2015).
11. Marth, J.D. Essentials of Glycobiology. Ch8: O-Glycans, Edn. 2. (Cold Spring Harbor Laboratory Press, NY; 2009).
12. Varki, A. Biological roles of oligosaccharides: all of the theories are correct. *Glycobiology* **3**, 97-130 (1993).
13. Deddish, P.A. et al. Carboxypeptidase M in Madin-Darby canine kidney cells. Evidence that carboxypeptidase M has a phosphatidylinositol glycan anchor. *J Biol Chem* **265**, 15083-15089 (1990).

14. Piesecki, S. & Alhadeff, J.A. The effect of carbohydrate removal on the properties of human liver alpha-L-fucosidase. *Biochim Biophys Acta* **1119**, 194-200 (1992).
15. Endreffy, I. et al. Plasma alpha-L-fucosidase activity in chronic inflammation and autoimmune disorders in a pediatric cohort of hospitalized patients. *Immunol Res* **65**, 1025-1030 (2017).
16. Lau, K.S. et al. Complex N-glycan number and degree of branching cooperate to regulate cell proliferation and differentiation. *Cell* **129**, 123-134 (2007).
17. Scott, J.E. Supramolecular organization of extracellular matrix glycosaminoglycans, in vitro and in the tissues. *Fed Am Soc Exp Biol J* **6**, 2639-2645 (1992).
18. Jiang, D., Liang, J. & Noble, P.W. Regulation of non-infectious lung injury, inflammation, and repair by the extracellular matrix glycosaminoglycan hyaluronan. *Anat Rec (Hoboken)* **293**, 982-985 (2010).
19. Hakomori, S. Structure, organization, and function of glycosphingolipids in membrane. *Curr Opin Hematol* **10**, 16-24 (2003).
20. Whitlow, M., Iida, K., Marshall, P., Silber, R. & Nussenzweig, V. Cells lacking glycan phosphatidylinositol-linked proteins have impaired ability to vesiculate. *Blood* **81**, 510-516 (1993).
21. Helenius, A. & Aebi, M. Roles of N-linked glycans in the endoplasmic reticulum. *Annu Rev Biochem* **73**, 1019-1049 (2004).
22. Kornfeld, R. & Kornfeld, S. Assembly of asparagine-linked oligosaccharides. *Annu Rev Biochem* **54**, 631-664 (1985).
23. Bause, E. Structural requirements of N-glycosylation of proteins. Studies with proline peptides as conformational probes. *Biochem J* **209**, 331-336 (1983).
24. Paulson, J.C. & Colley, K.J. Glycosyltransferases. Structure, localization, and control of cell type-specific glycosylation. *J Biol Chem* **264**, 17615-17618 (1989).
25. Breton, C., Snajdrova, L., Jeanneau, C., Koca, J. & Imberty, A. Structures and mechanisms of glycosyltransferases. *Glycobiology* **16**, 29R-37R (2006).
26. Sharon, N. & Lis, H. Lectins as cell recognition molecules. *Science* **246**, 227-234 (1989).
27. Velupillai, P. & Harn, D.A. Oligosaccharide-specific induction of interleukin 10 production by B220+ cells from schistosome-infected mice: a mechanism for regulation of CD4+ T-cell subsets. *Proc Natl Acad Sci U S A* **91**, 18-22 (1994).
28. Dube, D.H. & Bertozzi, C.R. Glycans in cancer and inflammation--potential for therapeutics and diagnostics. *Nat Rev Drug Discov* **4**, 477-488 (2005).

29. Mahal, L.K., Yarema, K.J. & Bertozzi, C.R. Engineering chemical reactivity on cell surfaces through oligosaccharide biosynthesis. *Science* **276**, 1125-1128 (1997).
30. Tu, Z., Lin, Y.N. & Lin, C.H. Development of fucosyltransferase and fucosidase inhibitors. *Chem Soc Rev* **42**, 4459-4475 (2013).
31. Ledesma, M.D., Bonay, P., Colaco, C. & Avila, J. Analysis of microtubule-associated protein tau glycation in paired helical filaments. *J Biol Chem* **269**, 21614-21619 (1994).
32. Sasaki, N. et al. Advanced glycation end products in Alzheimer's disease and other neurodegenerative diseases. *Am J Pathol* **153**, 1149-1155 (1998).
33. Vitek, M.P. et al. Advanced glycation end products contribute to amyloidosis in Alzheimer disease. *Proc Natl Acad Sci U S A* **91**, 4766-4770 (1994).
34. Wang, J.Z., Grundke-Iqbal, I. & Iqbal, K. Glycosylation of microtubule-associated protein tau: an abnormal posttranslational modification in Alzheimer's disease. *Nat Med* **2**, 871-875 (1996).
35. Furukawa, K. & Fukuda, M. Glycosignals in Cancer: Mechanisms of Malignant Phenotypes. (2016).
36. Chang, F., Li, R. & Ladisch, S. Shedding of gangliosides by human medulloblastoma cells. *Exp Cell Res* **234**, 341-346 (1997).
37. Hakomori, S. Aberrant glycosylation in cancer cell membranes as focused on glycolipids: overview and perspectives. *Cancer Res* **45**, 2405-2414 (1985).
38. Aarnoudse, C.A., Garcia Vallejo, J.J., Saeland, E. & van Kooyk, Y. Recognition of tumor glycans by antigen-presenting cells. *Curr Opin Immunol* **18**, 105-111 (2006).
39. Block, T.M. et al. Use of targeted glycoproteomics to identify serum glycoproteins that correlate with liver cancer in woodchucks and humans. *Proc Natl Acad Sci U S A* **102**, 779-784 (2005).
40. Schnaar, R.L. Glycobiology simplified: diverse roles of glycan recognition in inflammation. *J Leukoc Biol* **99**, 825-838 (2016).
41. Kogan, G. et al. Structural and immunochemical characterization of the type VIII group B Streptococcus capsular polysaccharide. *J Biol Chem* **271**, 8786-8790 (1996).
42. Stowell, S.R. et al. Innate immune lectins kill bacteria expressing blood group antigen. *Nat Med* **16**, 295-301 (2010).
43. van Die, I. & Cummings, R.D. Glycan gimmickry by parasitic helminths: a strategy for modulating the host immune response? *Glycobiology* **20**, 2-12 (2010).

44. Summers, R.W., Elliott, D.E., Urban, J.F., Jr., Thompson, R. & Weinstock, J.V. Trichuris suis therapy in Crohn's disease. *Gut* **54**, 87-90 (2005).
45. Zheng, X. et al. Soluble egg antigen from *Schistosoma japonicum* modulates the progression of chronic progressive experimental autoimmune encephalomyelitis via Th2-shift response. *J Neuroimmunol* **194**, 107-114 (2008).
46. Astronomo, R.D. & Burton, D.R. Carbohydrate vaccines: developing sweet solutions to sticky situations? *Nat Rev Drug Discov* **9**, 308-324 (2010).
47. Yin, X.G. et al. IgG Antibody Response Elicited by a Fully Synthetic Two-Component Carbohydrate-Based Cancer Vaccine Candidate with alpha-Galactosylceramide as Built-in Adjuvant. *Org Lett* **19**, 456-459 (2017).
48. Uro-Coste, E. et al. Cerebral amyloid angiopathy and microhemorrhages after amyloid beta vaccination: case report and brief review. *Clin Neuropathol* **29**, 209-216 (2010).
49. Yamamoto, F. Review: ABO blood group system--ABH oligosaccharide antigens, anti-A and anti-B, A and B glycosyltransferases, and ABO genes. *Immunohematology* **20**, 3-22 (2004).
50. Kwan, D.H., Ernst, S., Kotzler, M.P. & Withers, S.G. Chemoenzymatic Synthesis of a Type 2 Blood Group A Tetrasaccharide and Development of High-throughput Assays Enables a Platform for Screening Blood Group Antigen-cleaving Enzymes. *Glycobiology* **25**, 806-811 (2015).
51. Sturla, L. et al. Differential terminal fucosylation of N-linked glycans versus protein O-fucosylation in leukocyte adhesion deficiency type II (CDG IIc). *J Biol Chem* **278**, 26727-26733 (2003).
52. Marquardt, T. et al. Leukocyte adhesion deficiency II syndrome, a generalized defect in fucose metabolism. *J Pediatr* **134**, 681-688 (1999).
53. Hidalgo, A. et al. Insights into leukocyte adhesion deficiency type 2 from a novel mutation in the GDP-fucose transporter gene. *Blood* **101**, 1705-1712 (2003).
54. Block, T.M. et al. Treatment of chronic hepadnavirus infection in a woodchuck animal model with an inhibitor of protein folding and trafficking. *Nat Med* **4**, 610-614 (1998).
55. Block, T.M. et al. Secretion of human hepatitis B virus is inhibited by the imino sugar N-butyldeoxynojirimycin. *Proc Natl Acad Sci U S A* **91**, 2235-2239 (1994).
56. Cox, T. et al. Novel oral treatment of Gaucher's disease with N-butyldeoxynojirimycin (OGT 918) to decrease substrate biosynthesis. *Lancet* **355**, 1481-1485 (2000).
57. Cameron, H.S., Szczepaniak, D. & Weston, B.W. Expression of human chromosome 19p alpha(1,3)-fucosyltransferase genes in normal tissues. Alternative splicing, polyadenylation, and isoforms. *J Biol Chem* **270**, 20112-20122 (1995).

58. Wang, Y. et al. Loss of alpha1,6-fucosyltransferase suppressed liver regeneration: implication of core fucose in the regulation of growth factor receptor-mediated cellular signaling. *Sci Rep* **5**, 8264 (2015).
59. Moriwaki, K. & Miyoshi, E. Fucosylation and gastrointestinal cancer. *World J Hepatol* **2**, 151-161 (2010).
60. Pang, P.C. et al. Human sperm binding is mediated by the sialyl-Lewis(x) oligosaccharide on the zona pellucida. *Science* **333**, 1761-1764 (2011).
61. Foxall, C. et al. The three members of the selectin receptor family recognize a common carbohydrate epitope, the sialyl Lewis(x) oligosaccharide. *J Cell Biol* **117**, 895-902 (1992).
62. Takada, A. et al. Contribution of carbohydrate antigens sialyl Lewis A and sialyl Lewis X to adhesion of human cancer cells to vascular endothelium. *Cancer Res* **53**, 354-361 (1993).
63. Grabenhorst, E., Nimtz, M., Costa, J. & Conradt, H.S. In vivo specificity of human alpha1,3/4-fucosyltransferases III-VII in the biosynthesis of LewisX and Sialyl LewisX motifs on complex-type N-glycans. Coexpression studies from bhk-21 cells together with human beta-trace protein. *J Biol Chem* **273**, 30985-30994 (1998).
64. Cheng, L. et al. FUT family mediates the multidrug resistance of human hepatocellular carcinoma via the PI3K/Akt signaling pathway. *Cell Death Dis* **4**, e923 (2013).
65. Carrascal, M.A. et al. Inhibition of fucosylation in human invasive ductal carcinoma reduces E-selectin ligand expression, cell proliferation, and ERK1/2 and p38 MAPK activation. *Mol Oncol* **12**, 579-593 (2018).
66. Desiderio, V. et al. Increased fucosylation has a pivotal role in invasive and metastatic properties of head and neck cancer stem cells. *Oncotarget* **6**, 71-84 (2015).
67. Cordel, S., Goupille, C., Hallouin, F., Meflah, K. & Le Pendu, J. Role for alpha1,2-fucosyltransferase and histo-blood group antigen H type 2 in resistance of rat colon carcinoma cells to 5-fluorouracil. *Int J Cancer* **85**, 142-148 (2000).
68. Hallouin, F., Goupille, C., Bureau, V., Meflah, K. & Le Pendu, J. Increased tumorigenicity of rat colon carcinoma cells after alpha1,2-fucosyltransferase FTA anti-sense cDNA transfection. *Int J Cancer* **80**, 606-611 (1999).
69. Aubert, M. et al. Restoration of alpha(1,2) fucosyltransferase activity decreases adhesive and metastatic properties of human pancreatic cancer cells. *Cancer Res* **60**, 1449-1456 (2000).
70. Mathieu, S. et al. Transgene expression of alpha(1,2)-fucosyltransferase-I (FUT1) in tumor cells selectively inhibits sialyl-Lewis x expression and binding to E-selectin

- without affecting synthesis of sialyl-Lewis a or binding to P-selectin. *Am J Pathol* **164**, 371-383 (2004).
71. Hao, Y.Y. et al. alpha1,2-fucosyltransferase gene transfection influences on biological behavior of ovarian carcinoma-derived RMG-I cells. *J. Mol. Cell Biol. (Shanghai, China)* **41**, 435-442 (2008).
 72. Che, Y. et al. Critical involvement of the alpha(1,2)-fucosyltransferase in multidrug resistance of human chronic myeloid leukemia. *Oncol Rep* **35**, 3025-3033 (2016).
 73. Sakuma, K., Aoki, M. & Kannagi, R. Transcription factors c-Myc and CDX2 mediate E-selectin ligand expression in colon cancer cells undergoing EGF/bFGF-induced epithelial-mesenchymal transition. *Proc Natl Acad Sci U S A* **109**, 7776-7781 (2012).
 74. Hiller, K.M. et al. Transfection of alpha(1,3)fucosyltransferase antisense sequences impairs the proliferative and tumorigenic ability of human colon carcinoma cells. *Mol Carcinog* **27**, 280-288 (2000).
 75. Yang, X.S. et al. Overexpression of fucosyltransferase IV promotes A431 cell proliferation through activating MAPK and PI3K/Akt signaling pathways. *J Cell Physiol* **225**, 612-619 (2010).
 76. Li, J. et al. Human fucosyltransferase 6 enables prostate cancer metastasis to bone. *Br J Cancer* **109**, 3014-3022 (2013).
 77. Liu, F., Qi, H.L. & Chen, H.L. Regulation of differentiation- and proliferation-inducers on Lewis antigens, alpha-fucosyltransferase and metastatic potential in hepatocarcinoma cells. *Br J Cancer* **84**, 1556-1563 (2001).
 78. Zhang, J., Ju, N., Yang, X., Chen, L. & Yu, C. The alpha1,3-fucosyltransferase FUT7 regulates IL-1beta-induced monocyte-endothelial adhesion via fucosylation of endomucin. *Life Sci* **192**, 231-237 (2018).
 79. Laubli, H., Stevenson, J.L., Varki, A., Varki, N.M. & Borsig, L. L-selectin facilitation of metastasis involves temporal induction of Fut7-dependent ligands at sites of tumor cell arrest. *Cancer Res* **66**, 1536-1542 (2006).
 80. Kang, X. et al. Glycan-related gene expression signatures in human metastatic hepatocellular carcinoma cells. *Exp Ther Med* **3**, 415-422 (2012).
 81. Ji, J. et al. Expression of alpha 1,6-fucosyltransferase 8 in hepatitis B virus-related hepatocellular carcinoma influences tumour progression. *Dig Liver Dis* **45**, 414-421 (2013).
 82. Norden, R., Samuelsson, E. & Nystrom, K. NFkappaB-mediated activation of the cellular FUT3, 5 and 6 gene cluster by herpes simplex virus type 1. *Glycobiology* **27**, 999-1005 (2017).

83. McGovern, D.P. et al. Fucosyltransferase 2 (FUT2) non-secretor status is associated with Crohn's disease. *Hum Mol Genet* **19**, 3468-3476 (2010).
84. Ronchetti, F. et al. ABO/Secretor genetic complex and susceptibility to asthma in childhood. *Eur Respir J* **17**, 1236-1238 (2001).
85. Kannagi, R. Transcriptional regulation of expression of carbohydrate ligands for cell adhesion molecules in the selectin family. *Adv Exp Med Biol* **491**, 267-278 (2001).
86. Nystrom, K. et al. Induction of sialyl-Lex expression by herpes simplex virus type 1 is dependent on viral immediate early RNA-activated transcription of host fucosyltransferase genes. *Glycobiology* **19**, 847-859 (2009).
87. Norden, R., Nystrom, K. & Olofsson, S. Inhibition of protein deacetylation augments herpes simplex virus type 1-activated transcription of host fucosyltransferase genes associated with virus-induced sLex expression. *Arch Virol* **155**, 305-313 (2010).
88. Nystrom, K. et al. Virus-induced transcriptional activation of host FUT genes associated with neo-expression of Ley in cytomegalovirus-infected and sialyl-Lex in varicella-zoster virus-infected diploid human cells. *Glycobiology* **17**, 355-366 (2007).
89. Blaser, M.J., Chyou, P.H. & Nomura, A. Age at Establishment of Helicobacter pylori Infection and Gastric Carcinoma, Gastric Ulcer, and Duodenal Ulcer Risk. *Cancer Research* **55**, 562-565 (1995).
90. Crespo, A. & Suh, B. Helicobacter pylori infection: epidemiology, pathophysiology, and therapy. *Arch Pharm Res* **24**, 485-498 (2001).
91. Forman, D. et al. Association between infection with Helicobacter pylori and risk of gastric cancer: evidence from a prospective investigation. *BMJ* **302**, 1302-1305 (1991).
92. Rauws, E.A.J. & Tytgat, G.N.J. Cure of duodenal ulcer associated with eradication of Helicobacter pylori. *Lancet* **335**, 1233-1235 (1990).
93. Appelmek, B.J., Monteiro, M.A., Martin, S.L., Moran, A.P. & Vandenbroucke-Grauls, C.M. Why Helicobacter pylori has Lewis antigens. *Trends Microbiol* **8**, 565-570 (2000).
94. Edwards, N.J. et al. Lewis X structures in the O antigen side-chain promote adhesion of Helicobacter pylori to the gastric epithelium. *Mol Microbiol* **35**, 1530-1539 (2000).
95. Moran, A.P., Prendergast, M.M. & Appelmek, B.J. Molecular mimicry of host structures by bacterial lipopolysaccharides and its contribution to disease. *FEMS Immunol Med Microbiol* **16**, 105-115 (1996).
96. Larkin, M. et al. Spectrum of sialylated and nonsialylated fuco-oligosaccharides bound by the endothelial-leukocyte adhesion molecule E-selectin. Dependence of the carbohydrate binding activity on E-selectin density. *J Biol Chem* **267**, 13661-13668 (1992).

97. Galustian, C., Elviss, N., Chart, H., Owen, R. & Feizi, T. Interactions of the gastrotropic bacterium *Helicobacter pylori* with the leukocyte-endothelium adhesion molecules, the selectins--a preliminary report. *FEMS Immunol Med Microbiol* **36**, 127-134 (2003).
98. Qasba, P.K., Ramakrishnan, B. & Boeggeman, E. Substrate-induced conformational changes in glycosyltransferases. *Trends Biochem Sci* **30**, 53-62 (2005).
99. Collins, B.E. & Paulson, J.C. Cell surface biology mediated by low affinity multivalent protein-glycan interactions. *Curr Opin Chem Biol* **8**, 617-625 (2004).
100. Makita, Z., Vlassara, H., Cerami, A. & Bucala, R. Immunochemical detection of advanced glycosylation end products in vivo. *J Biol Chem* **267**, 5133-5138 (1992).
101. Schjoldager, K.T. et al. A systematic study of site-specific GalNAc-type O-glycosylation modulating proprotein convertase processing. *J Biol Chem* **286**, 40122-40132 (2011).
102. Morais, V.A. et al. Expression and characterization of recombinant human alpha-3/4-fucosyltransferase III from *Spodoptera frugiperda* (Sf9) and *Trichoplusia ni* (Tn) cells using the baculovirus expression system. *Biochem J* **353**, 719-725 (2001).
103. Lloyd, K.O. & Furukawa, K. Biosynthesis and functions of gangliosides: recent advances. *Glycoconj J* **15**, 627-636 (1998).
104. Christiansen, M.N. et al. Cell surface protein glycosylation in cancer. *Proteomics* **14**, 525-546 (2014).
105. Malissard, M., Zeng, S. & Berger, E.G. The yeast expression system for recombinant glycosyltransferases. *Glycoconj J* **16**, 125-139 (1999).
106. Jarvis, D.L. Developing baculovirus-insect cell expression systems for humanized recombinant glycoprotein production. *Virology* **310**, 1-7 (2003).
107. Jenkins, N., Parekh, R.B. & James, D.C. Getting the glycosylation right: implications for the biotechnology industry. *Nat Biotechnol* **14**, 975-981 (1996).
108. Yin, B. et al. Glycoengineering of Chinese hamster ovary cells for enhanced erythropoietin N-glycan branching and sialylation. *Biotechnol Bioeng* **112**, 2343-2351 (2015).
109. Hamilton, S.R. & Gerngross, T.U. Glycosylation engineering in yeast: the advent of fully humanized yeast. *Curr Opin Biotechnol* **18**, 387-392 (2007).
110. Bill, R.M. Playing catch-up with *Escherichia coli*: using yeast to increase success rates in recombinant protein production experiments. *Front Microbiol* **5**, 85 (2014).
111. Widmann, M. & Christen, P. Comparison of folding rates of homologous prokaryotic and eukaryotic proteins. *J Biol Chem* **275**, 18619-18622 (2000).

112. Plante, O.J., Palmacci, E.R. & Seeberger, P.H. Automated solid-phase synthesis of oligosaccharides. *Science* **291**, 1523-1527 (2001).
113. Hanson, S., Best, M., Bryan, M.C. & Wong, C.H. Chemoenzymatic synthesis of oligosaccharides and glycoproteins. *Trends Biochem Sci* **29**, 656-663 (2004).
114. Blixt, O. et al. Chemoenzymatic synthesis of 2-azidoethyl-ganglio-oligosaccharides GD3, GT3, GM2, GD2, GT2, GM1, and GD1a. *Carbohydr Res* **340**, 1963-1972 (2005).
115. Shinohara, Y., Furukawa, J., Niikura, K., Miura, N. & Nishimura, S. Direct N-glycan profiling in the presence of tryptic peptides on MALDI-TOF by controlled ion enhancement and suppression upon glycan-selective derivatization. *Anal Chem* **76**, 6989-6997 (2004).
116. Murray, B.W., Takayama, S., Schultz, J. & Wong, C.H. Mechanism and specificity of human alpha-1,3-fucosyltransferase V. *Biochemistry* **35**, 11183-11195 (1996).
117. De Vries, T., Palcic, M.P., Schoenmakers, P.S., Van Den Eijnden, D.H. & Joziassse, D.H. Acceptor specificity of GDP-Fuc:Gal beta 1->4GlcNAc-R alpha 3-fucosyltransferase VI (FucT VI) expressed in insect cells as soluble, secreted enzyme. *Glycobiology* **7**, 921-927 (1997).
118. Lee, L.V. et al. A potent and highly selective inhibitor of human alpha-1,3-fucosyltransferase via click chemistry. *J Am Chem Soc* **125**, 9588-9589 (2003).
119. Rillahan, C.D., Brown, S.J., Register, A.C., Rosen, H. & Paulson, J.C. High-throughput screening for inhibitors of sialyl- and fucosyltransferases. *Angew Chem Int Ed Engl* **50**, 12534-12537 (2011).
120. Hosoguchi, K. et al. An efficient approach to the discovery of potent inhibitors against glycosyltransferases. *J Med Chem* **53**, 5607-5619 (2010).
121. Lin, T.W., Chang, W.W., Chen, C.C. & Tsai, Y.C. Stachybotrydial, a potent inhibitor of fucosyltransferase and sialyltransferase. *Biochem Biophys Res Commun* **331**, 953-957 (2005).
122. Gonzalo, P., Sontag, B., Guillot, D. & Reboud, J.P. Fluorometric assay of GTPase activity: application to the couple elongation factor eEF-2-ribosome. *Anal Biochem* **225**, 178-180 (1995).
123. Sista, R. et al. Development of a digital microfluidic platform for point of care testing. *Lab Chip* **8**, 2091-2104 (2008).
124. Wulff-Burchfield, E. et al. Microfluidic platform versus conventional real-time polymerase chain reaction for the detection of *Mycoplasma pneumoniae* in respiratory specimens. *Diagn Microbiol Infect Dis* **67**, 22-29 (2010).

125. Agresti, J.J. et al. Ultrahigh-throughput screening in drop-based microfluidics for directed evolution. *Proc Natl Acad Sci U S A* **107**, 4004-4009 (2010).
126. Kintses, B. et al. Picoliter cell lysate assays in microfluidic droplet compartments for directed enzyme evolution. *Chem Biol* **19**, 1001-1009 (2012).
127. Khanafer, K., Vafai, K. & Lightstone, M. Buoyancy-driven heat transfer enhancement in a two-dimensional enclosure utilizing nanofluids. *Int J Heat Mass Transfer* **46**, 3639-3653 (2003).
128. Hamilton, R.L.C., O.K. Thermal conductivity of heterogeneous two-component systems. *I & EC Fundam.* **1**, 182-191 (1962).
129. Liu, Y. et al. Multilayer-assembled microchip for enzyme immobilization as reactor toward low-level protein identification. *Anal Chem* **78**, 801-808 (2006).
130. Zhao, X., Cheng, K. & Liu, D. Organosolv pretreatment of lignocellulosic biomass for enzymatic hydrolysis. *Appl Microbiol Biotechnol* **82**, 815-827 (2009).
131. Zou, Y., Xiang, C., Sun, L.X. & Xu, F. Glucose biosensor based on electrodeposition of platinum nanoparticles onto carbon nanotubes and immobilizing enzyme with chitosan-SiO(2) sol-gel. *Biosens Bioelectron* **23**, 1010-1016 (2008).
132. Zeng, J., Chen, X., Liang, Q., Xu, X. & Jing, X. Enzymatic degradation of poly(L-lactide) and poly(epsilon-caprolactone) electrospun fibers. *Macromol Biosci* **4**, 1118-1125 (2004).
133. Araci, I.E. & Quake, S.R. Microfluidic very large scale integration (mVLSI) with integrated micromechanical valves. *Lab Chip* **12**, 2803-2806 (2012).
134. Thorsen, T., Maerkl, S.J. & Quake, S.R. Microfluidic large-scale integration. *Science* **298**, 580-584 (2002).
135. Beebe, D.J., Mensing, G.A. & Walker, G.M. Physics and applications of microfluidics in biology. *Annu Rev Biomed Eng* **4**, 261-286 (2002).
136. Doshi, N. et al. Flow and adhesion of drug carriers in blood vessels depend on their shape: a study using model synthetic microvascular networks. *J Control Release* **146**, 196-200 (2010).
137. Song, H., Chen, D.L. & Ismagilov, R.F. Reactions in droplets in microfluidic channels. *Angew Chem Int Ed Engl* **45**, 7336-7356 (2006).
138. Song, H., Tice, J.D. & Ismagilov, R.F. A microfluidic system for controlling reaction networks in time. *Angew Chem Int Ed Engl* **42**, 768-772 (2003).
139. Ismagilov, R.F. Integrated microfluidic systems. *Angew Chem Int Ed Engl* **42**, 4130-4132 (2003).

140. Ge, L., Wang, S., Song, X., Ge, S. & Yu, J. 3D origami-based multifunction-integrated immunodevice: low-cost and multiplexed sandwich chemiluminescence immunoassay on microfluidic paper-based analytical device. *Lab Chip* **12**, 3150-3158 (2012).
141. Li, W. et al. Multiplex electrochemical origami immunodevice based on cuboid silver-paper electrode and metal ions tagged nanoporous silver-chitosan. *Biosens Bioelectron* **56**, 167-173 (2014).
142. Hu, J. et al. Advances in paper-based point-of-care diagnostics. *Biosens Bioelectron* **54**, 585-597 (2014).
143. Martinez, A.W., Phillips, S.T., Whitesides, G.M. & Carrilho, E. Diagnostics for the developing world: microfluidic paper-based analytical devices. *Anal Chem* **82**, 3-10 (2010).
144. Fobel, R., Fobel, C. & Wheeler, A.R. DropBot: An open-source digital microfluidic control system with precise control of electrostatic driving force and instantaneous drop velocity measurement. *Appl Phys Lett* **102** (2013).
145. Vo, P.Q.N., Husser, M.C., Ahmadi, F., Sinha, H. & Shih, S.C.C. Image-based feedback and analysis system for digital microfluidics. *Lab Chip* **17**, 3437-3446 (2017).
146. Paik, P.Y., Pamula, V.K. & Chakrabarty, K. Adaptive Cooling of Integrated Circuits Using Digital Microfluidics. *IEEE Transactions on VLSI Systems* **16**, 432-443 (2008).
147. Kalsi, S. et al. Rapid and sensitive detection of antibiotic resistance on a programmable digital microfluidic platform. *Lab Chip* **15**, 3065-3075 (2015).
148. Hadwen, B. et al. Programmable large area digital microfluidic array with integrated droplet sensing for bioassays. *Lab Chip* **12**, 3305-3313 (2012).
149. Zeng, X. et al. Chemiluminescence detector based on a single planar transparent digital microfluidic device. *Lab Chip* **13**, 2714-2720 (2013).
150. Lin, L., Evans, R.D., Jokerst, N.M. & Fair, R.B. Integrated optical sensor in a digital microfluidic platform. *IEEE Sens. J.* **8**, 628-635 (2008).
151. Shih, S.C.C., Barbulovic-Nad, I., Yang, X., Fobel, R. & Wheeler, A.R. Digital microfluidics with impedance sensing for integrated cell culture and analysis. *Biosens. Bioelectron.* **42**, 314-320 (2013).
152. Dryden, M.D.M., Fobel, R., Fobel, C. & Wheeler, A.R. Upon the Shoulders of Giants: Open-Source Hardware and Software in Analytical Chemistry. *Anal Chem* **89**, 4330-4338 (2017).
153. Graham, C. et al. Novel application of digital microfluidics for the detection of biotinidase deficiency in newborns. *Clin Biochem* **46**, 1889-1891 (2013).

154. Boles, D.J. et al. Droplet-based pyrosequencing using digital microfluidics. *Anal Chem* **83**, 8439-8447 (2011).
155. Miller, E.M. & Wheeler, A.R. A digital microfluidic approach to homogeneous enzyme assays. *Anal Chem* **80**, 1614-1619 (2008).
156. Luk, V.N., Fiddes, L.K., Luk, V.M., Kumacheva, E. & Wheeler, A.R. Digital microfluidic hydrogel microreactors for proteomics. *Proteomics* **12**, 1310-1318 (2012).
157. Millington, D. et al. Digital microfluidics comes of age: high-throughput screening to bedside diagnostic testing for genetic disorders in newborns. *Expert Rev Mol Diagn*, 1-12 (2018).
158. Dittrich, P.S. & Manz, A. Lab-on-a-chip: microfluidics in drug discovery. *Nat Rev Drug Discov* **5**, 210-218 (2006).
159. Martin, J.G. et al. Toward an artificial Golgi: redesigning the biological activities of heparan sulfate on a digital microfluidic chip. *J Am Chem Soc* **131**, 11041-11048 (2009).
160. Nguyen, E.P. et al. Hybrid Surface and Bulk Resonant Acoustics for Concurrent Actuation and Sensing on a Single Microfluidic Device. *Anal Chem* **90**, 5335-5342 (2018).
161. Cao, Q., Han, X. & Li, L. Configurations and control of magnetic fields for manipulating magnetic particles in microfluidic applications: magnet systems and manipulation mechanisms. *Lab Chip* **14**, 2762-2777 (2014).
162. Fan, X. & White, I.M. Optofluidic Microsystems for Chemical and Biological Analysis. *Nat Photonics* **5**, 591-597 (2011).
163. Abdelgawad, M., Freire, S.L., Yang, H. & Wheeler, A.R. All-terrain droplet actuation. *Lab Chip* **8**, 672-677 (2008).
164. Fan, S.K., Yang, H. & Hsu, W. Droplet-on-a-wristband: chip-to-chip digital microfluidic interfaces between replaceable and flexible electrowetting modules. *Lab Chip* **11**, 343-347 (2011).
165. Choi, K., Ng, A.H., Fobel, R. & Wheeler, A.R. Digital microfluidics. *Annu Rev Anal Chem (Palo Alto Calif)* **5**, 413-440 (2012).
166. Pollack, M.G., Fair, R.B. & Shenderov, A.D. Electrowetting-based actuation of liquid droplets for microfluidic applications. *Applied Physics Letters* **77**, 1725-1726 (2000).
167. Hsieh, T.F., S. in IEEE 21st International Conference on Micro Electro Mechanical Systems 641-644 (Tucson, Arizona; 2008).
168. Chatterjee, D., Hetayothin, B., Wheeler, A.R., King, D.J. & Garrell, R.L. Droplet-based microfluidics with nonaqueous solvents and solutions. *Lab Chip* **6**, 199-206 (2006).

169. Kang, K.Y. How Electrostatic Fields Change Contact Angle in Electrowetting. *Langmuir* **18**, 10318–10322 (2002).
170. Pohl, H.A. The Motion and Precipitation of Suspensoids in Divergent Electric Fields. *Journal of Applied Physics* **22**, 869-871 (1951).
171. Jones, T.B. *Electromechanics of Particles*. (Cambridge Univ. Press Cambridge, U.K.; 1995).
172. Zhao, Y., Yi, U.-C. & Cho, S.K. Microparticle Concentration and Separation by Traveling-Wave Dielectrophoresis (twDEP) for Digital Microfluidics. *Journal of Microelectromechanical Systems* **16**, 1472-1481 (2007).
173. Rice, C.L.W., R. Electrokinetic flow in a narrow cylindrical capillary. *J. Phys. Chem.* **69**, 4017-4024 (1965).
174. Wong, P.K., Wang, T.H., Deval, J.H. & Ho, C.M. Electrokinetics in Micro Devices for Biotechnology Applications. *IEEE/ASME Transactions on Mechatronics* **9**, 366-376 (2004).
175. Castellarnau, M., Errachid, A., Madrid, C., Juarez, A. & Samitier, J. Dielectrophoresis as a tool to characterize and differentiate isogenic mutants of Escherichia coli. *Biophys J* **91**, 3937-3945 (2006).
176. Chatterjee, D., Shepherd, H. & Garrell, R.L. Electromechanical model for actuating liquids in a two-plate droplet microfluidic device. *Lab Chip* **9**, 1219-1229 (2009).
177. Seyrat, E. & Hayes, R.A. Amorphous fluoropolymers as insulators for reversible low-voltage electrowetting. *Journal of Applied Physics* **90**, 1383-1386 (2001).
178. Lin, Y.Y. et al. Low Voltage Electrowetting-on-Dielectric Platform using Multi-Layer Insulators. *Sens Actuators B Chem* **150**, 465-470 (2010).
179. Luk, V.N., Mo, G. & Wheeler, A.R. Pluronic additives: a solution to sticky problems in digital microfluidics. *Langmuir* **24**, 6382-6389 (2008).
180. Au, S.H., Kumar, P. & Wheeler, A.R. A new angle on pluronic additives: advancing droplets and understanding in digital microfluidics. *Langmuir* **27**, 8586-8594 (2011).
181. Ren, H.S., Vijay;B. Fair, Richard in *Int. Conf. Solid-State Sens., Actuators Microsyst., 12th*, Vol. 1 619-622 (IEEE, 2003).
182. Ren, H. Automated on-chip droplet dispensing with volume control by electro-wetting actuation and capacitance metering. *Sensors and Actuators B: Chemical* **98**, 319-327 (2004).
183. Ren, H. (2004). Electro-wetting based sample preparation: An initial study for droplet transportation, creation and on-chip digital dilution., Duke University. PhD.

184. Singh, A.K. et al. Unravelling the multiple functions of the architecturally intricate *Streptococcus pneumoniae* beta-galactosidase, BgaA. *PLoS Pathog* **10**, e1004364 (2014).
185. Mark, B.L. et al. Structural and functional characterization of *Streptomyces plicatus* beta-N-acetylhexosaminidase by comparative molecular modeling and site-directed mutagenesis. *J Biol Chem* **273**, 19618-19624 (1998).
186. Brassard, D., Malic, L., Normandin, F., Tabrizian, M. & Veres, T. Water-oil core-shell droplets for electrowetting-based digital microfluidic devices. *Lab Chip* **8**, 1342-1349 (2008).
187. Vergauwe, N. et al. Controlling droplet size variability of a digital lab-on-a-chip for improved bio-assay performance. *Microfluidics and Nanofluidics* **11**, 25-34 (2011).
188. Kim, Y.W., Lee, S.S., Warren, R.A. & Withers, S.G. Directed evolution of a glycosynthase from *Agrobacterium* sp. increases its catalytic activity dramatically and expands its substrate repertoire. *J Biol Chem* **279**, 42787-42793 (2004).
189. Cold Spring Harbor Protocols (2006). "Preparation of 0.1 M Potassium Phosphate Buffer at 25°C." Retrieved 2016-11-07, from <http://cshprotocols.cshlp.org/content/2006/1/pdb.tab19>.
190. Kajihara, Y. et al. Synthesis of 2-[(2-pyridyl)amino]ethyl beta-D-lactosaminide and evaluation of its acceptor ability for sialyltransferase: a comparison with 4-methylumbelliferyl and dansyl beta-D-lactosaminide. *Carbohydr Res* **339**, 1545-1550 (2004).
191. Zeng, J. & Korsmeyer, T. Principles of droplet electrohydrodynamics for lab-on-a-chip. *Lab Chip* **4**, 265-277 (2004).
192. Liechti, C. "PySerial." 2018, from <http://pypi.python.org/pypi/pyserial>.
193. Zhang, J.H., Chung, T.D. & Oldenburg, K.R. A Simple Statistical Parameter for Use in Evaluation and Validation of High Throughput Screening Assays. *J Biomol Screen* **4**, 67-73 (1999).
194. de Vries, T., Knegt, R.M., Holmes, E.H. & Macher, B.A. Fucosyltransferases: structure/function studies. *Glycobiology* **11**, 119R-128R (2001).
195. Wong, C.H., Dumas, D. P., Ichikawa, Y., Koseki, K., Danishefsky, S. J., Weston, B. W., Lowe, J. B. Specificity, inhibition, and synthetic utility of a recombinant human. alpha.-1, 3-fucosyltransferase. *Journal of the American Chemical Society* **114**, 7321-7322 (1992).
196. Yoon, J.Y. & Garrell, R.L. Preventing Biomolecular Adsorption in Electrowetting-Based Biofluidic Chips. *Anal Chem* **75**, 5097-5102 (2003).

197. Rajabi, N. & Dolatabadi, A. A novel electrode shape for electrowetting-based microfluidics. *Colloids and Surfaces A: Physicochemical and Engineering Aspects* **365**, 230-236 (2010).
198. Chen, J., Yu, Y., Li, J., Lai, Y. & Zhou, J. Size-variable droplet actuation by interdigitated electrowetting electrode. *Applied Physics Letters* **101** (2012).
199. Pollack, M.G., Shenderov, A.D. & Fair, R.B. Electrowetting-based actuation of droplets for integrated microfluidics. *Lab Chip* **2**, 96-101 (2002).
200. Paik, P., Pamula, V.K., Pollack, M.G. & Fair, R.B. Electrowetting-based droplet mixers for microfluidic systems. *Lab Chip* **3**, 28-33 (2003).
201. Hamadi, F., Latrache, H., Zekraoui, M., Ellouali, M. & Bengourram, J. Effect of pH on surface energy of glass and Teflon and theoretical prediction of Staphylococcus aureus adhesion. *Materials Science and Engineering: C* **29**, 1302-1305 (2009).
202. Berthier, J. & Peponnet, C. A model for the determination of the dimensions of dents for jagged electrodes in electrowetting on dielectric microsystems. *Biomicrofluidics* **1**, 14104 (2007).
203. Lienemann, J., et al. (2003). Electrode shapes for electrowetting arrays. *Nanotech* 2003, researchgate.net.
204. Fair, R.B.S., V.; Ren, H.; Paik, P.; Pamula, V.K.; Pollack, M.G. in IEEE International Electron Devices Meeting 32.35.31-32.35.34 (2004).
205. Shih, S.C., Barbulovic-Nad, I., Yang, X., Fobel, R. & Wheeler, A.R. Digital microfluidics with impedance sensing for integrated cell culture and analysis. *Biosens Bioelectron* **42**, 314-320 (2013).
206. Calabrese, E.J. & Baldwin, L.A. The frequency of U-shaped dose responses in the toxicological literature. *Toxicol Sci* **62**, 330-338 (2001).
207. Owen, S.C. et al. Colloidal drug formulations can explain "bell-shaped" concentration-response curves. *ACS Chem Biol* **9**, 777-784 (2014).
208. Zegarra-Moran, O. et al. Correction of G551D-CFTR transport defect in epithelial monolayers by genistein but not by CPX or MPB-07. *Br J Pharmacol* **137**, 504-512 (2002).
209. Dienes, A., Shank, C. & Kohn, R. Characteristics of the 4-methylumbelliferone laser dye. *IEEE Journal of Quantum Electronics* **9**, 833-843 (1973).
210. Kongkamnerd, J. et al. The quenching effect of flavonoids on 4-methylumbelliferone, a potential pitfall in fluorimetric neuraminidase inhibition assays. *J Biomol Screen* **16**, 755-764 (2011).

211. Litten, B., Blackett, C., Wigglesworth, M., Goddard, N. & Fielden, P. Artefacts at the liquid interface and their impact in miniaturized biochemical assay. *Biomicrofluidics* **9**, 052607 (2015).
212. Eydelnant, I.A., Betty Li, B. & Wheeler, A.R. Microgels on-demand. *Nat Commun* **5**, 3355 (2014).
213. Toppila, S., Paavonen, T., Laitinen, A., Laitinen, L.A. & Renkonen, R. Endothelial sulfated sialyl Lewis x glycans, putative L-selectin ligands, are preferentially expressed in bronchial asthma but not in other chronic inflammatory lung diseases. *Am J Respir Cell Mol Biol* **23**, 492-498 (2000).

Appendix

Introduction to DMF Automation Systems

In a given DMF experiment, there are many types of operations to be performed on a device. The simplest form of DMF device operation comes from direct application of a potential to the desired electrodes by touching the positive wire of a circuit to a contact pad which is connected to the electrode, while touching the negative wire of a circuit to the ground. This would not only considerably slow the pace of an experiment and require manual dexterity, it would also render impossible certain operations which require fast sequential actuations of different electrodes and cut out the possibility for automation entirely. In order to facilitate the efficient operation of DMF chips, many labs develop automation systems and softwares independently of one-another. This does not take advantage of the potential of DMF as something that could be shared by any lab and downloaded by others in the manner of plug-and-play, both with regards to the design of devices and the experiments that are run by them. Cross-platform, open-source software that is user-friendly enough and compatible enough with other modules could help to reach that goal.

LLGUI

The initial automation system available was run through MATLAB (MathWorks) and coded in C++. Its advantage was its GUI (user interface) which allowed one to visually select electrodes to actuate and visually construct sequences from an array-based representation of the electrode layout. However, it was prone to glitching, and sequences needed to be loaded individually by inputting their file names. This would make any experiment involving the

responsive use of many sequences very arduous to run. Additionally, the MATLAB code was too difficult to decipher for non-coding labmates, making it impossible for them to debug, remix or expand upon what was already there to add additional functionalities. As such, a second automation system called ArduBridge was developed by Guy Soffer, which runs on the cross-platform coding language, Python 2.7. Comparatively more easy to teach and learn than MATLAB, labmates could now easily add to and expand upon it.

ArduBridge was run by inputting commands through the Python shell (IDLE). This would require entering a string of code into the python shell every time one wishes to actuate an electrode sequence during an experiment. To prevent slowing down device operation by repeatedly typing, and having to remember all of the sequence names, I created a GUI (LLGUI) to be used as an interface for ArduBridge, with help from Guy Soffer. To make LLGUI possible, ArduBridge's protocol file was also modified to include sequence categories and descriptions.

Typically, LLGUI read the user's ArduBridge protocol file and created a window with a button for each droplet operation sequence. (Figure 14) These sequence buttons were grouped under their similar droplet operation categories (dispensing, movement, mixing, and stashing or unstashing from reservoirs) to facilitate organization and visual interpretation. A text input box allowed the user to specify the number of repeats required for the sequence. Hovering over a button displayed the tooltip (sequence description) and clicking the button copied the command string to one's clipboard (this was achieved by using the python module, 'pyperclip'). This could then be pasted in the shell, from which one could begin sequence actuation. LLGUI also included a button which would copy the ArduBridge command for closing the Arduino.

Since that time, a new version of LLGUI came out with a few more additions by myself (better space allocation) and Guy Soffer (buttons for opening or reopening the connection to the Arduino through the USB port, and clicking the buttons now immediately actuates the sequence).

PaseMaker (Path Sequence Maker)

Writing dozens of actuation sequences with a hundred numbered electrodes on a DMF device can be costly with regards to time and human error. A program called Pasemaker.py was created to automate construction of electrode sequences universally (for any and all DMF designs), with thought to compatibility with other softwares and future functionality.

When PaseMaker is used alone, users provide a .csv file listing each electrode of a DMF device as its reference pin number on a separate row, and for each electrode, the electrodes adjacent to it are listed in any number of columns on that same row. From this information, Pasemaker constructs non-visual graphs which map out the DMF chips as networks in which every electrode is a node and every connection between electrodes is of a certain distance (the distance is automatically assigned as 1). Pasemaker's windowed interface allows users to load their .csv from a file browser/picker, after which it allows them to view, select and copy to the clipboard the raw numeric graph produced by Pasemaker. In a text input box on the interface, the user could choose to provide a customizable string in which they could specify where the sequence would be inserted once it had been created. In two other provided spaces, the user could enter the pin number of the start and end point electrodes, after which they could select what kind of sequence they wished to construct between those for Moving, Dispensing, Low-Volume Dispensing, Mixing in a line, Mixing in a circle, or Splitting of volumes between the two user-specified electrodes. (Table 4) Pasemaker would then use Dijkstra's Algorithm to solve for the shortest path and format it into the aforementioned customizable string, if it was provided. (Table 5)

Table 4) How PaseMaker constructs sequences



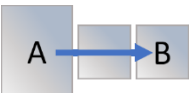
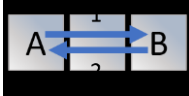

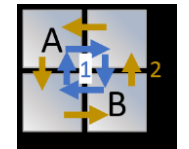
Sequence type and droplet activity	User-designated electrodes (Visual)	PaseMaker
Move (Moves from A to B)		Solves shortest path from A to B and constructs the electrode sequence from A to B
Dispense (Dispenses from A to B)		Solves shortest path from A to B and constructs the electrode sequence from A to B, then appends the simultaneous actuation of A and B
Disp-LV (Useful to dispense from A to B even when volume in A is low)		Solves shortest path from A to B and constructs the electrode sequence from A to B, then, while keeping electrode B actuated at every step, appends the actuation of electrodes in reverse order (from B to A), ending with the simultaneous actuation of A and B
Mix-I (Mixing in a straight line $A \rightleftharpoons B$)		Solves shortest path from A to B and constructs the electrode sequence from A to B, then appends the same sequence but with reversed order.
Split (Splits a central volume to A and B)		Solves shortest path from A to B. Checks the number of electrodes: if odd, there is a single central electrode. If even, there are two central electrodes. Constructs the electrode sequence to actuate the central electrode(s) then simultaneously actuate a path from the central electrode(s) to A and to B.
Mix-O (Mixing in a circle encompassing A and B)		Computes whether or not A and B are mutually connected to two other, separate electrodes. If so, then the path from A to B across one of these mutual adjacents is appended to the path from B to A across the other of the mutual adjacents. The sequence is constructed, then appended to itself but with reversed order.

Table 5) Examples of sequences made with PaseMaker

Example DMF Chip design	
Sequence desired	
Move 1 to 5	[[1], [1, 2], [2], [2, 3], [3], [3, 5], [5]]
Dispense 1 to 5	[[1], [1, 2], [2], [2, 3], [3], [3, 5], [5], [1, 5], [1, 5]]
Disp-LV 1 to 5	[[1], [1, 2], [2], [2, 3], [3], [3, 5], [5], [5, 2, 3], [1, 2, 5]]
Mix-I 4 to 6	[[4], [4, 5], [5], [5, 6], [6], [6], [5, 6], [5], [4, 5], [4]]
Split 4 to 6	[[5], [4, 5, 6], [4, 6]]
Split 4 to 7	[[5, 6], [4, 5, 6, 7], [4, 7]]
Mix-O 7 to 10	[[7], [7, 8], [8], [8, 10], [10], [10, 9], [9], [9, 7], [7], [9, 7], [9], [10, 9], [10], [8, 10], [8], [7, 8], [7]]

‘Bussing’ is the term given to a situation where multiple separate electrodes are controlled by the same switch, and as such, always actuate at the same time. Some DMF designs employ this to save space or to have more electrodes than the number of available control switches. To be fool-proof, Pasemaker automatically detects electrode bussing and assigns them different IDs in the graph so as to distinguish between spatially separate electrodes throughout its path-solving and sequence construction operations even if they shared the same pin number. If either or both of the electrodes specified for path solving were bussed, a window would pop up asking the user to select which of the displayed bussed electrodes to use for path solving and sequence making.